In compliance with the
Canadian Privacy Legislation
some supporting forms
may have been removed from
this dissertation.

While these forms may be included
in the document page count,
their removal does not represent
any loss of content from the dissertation.

University of Alberta

Electrostatic Double Layer Interactions in Confined and Many-Body Geometries

By

Prodip Kumar Das

A thesis submitted to the Faculty of Graduate Studies and Research in partial fulfillment of the requirements for the degree of **Master of Science**.

Department of Mechanical Engineering

Edmonton, Alberta
Fall 2003

National Library
of Canada

Acquisitions and
Bibliographic Services

395 Wellington Street
Ottawa ON K1A 0N4
Canada

Bibliothèque nationale
du Canada

Acquisisitons et
services bibliographiques

395, rue Wellington
Ottawa ON K1A 0N4
Canada

Your file Votre référence
ISBN: 0-612-87747-7
Our file Notre référence
ISBN: 0-612-87747-7

The author has granted a non-exclusive licence allowing the National Library of Canada to reproduce, loan, distribute or sell copies of this thesis in microform, paper or electronic formats.

The author retains ownership of the copyright in this thesis. Neither the thesis nor substantial extracts from it may be printed or otherwise reproduced without the author's permission.

L'auteur a accordé une licence non exclusive permettant à la Bibliothèque nationale du Canada de reproduire, prêter, distribuer ou vendre des copies de cette thèse sous la forme de microfiche/film, de reproduction sur papier ou sur format électronique.

L'auteur conserve la propriété du droit d'auteur qui protège cette thèse. Ni la thèse ni des extraits substantiels de celle-ci ne doivent être imprimés ou aturement reproduits sans son autorisation.

Canada

University of Alberta

Library Release Form

Name of Author: Prodip Kumar Das

Title of Thesis: Electrostatic Double Layer Interactions in Confined and Many-Body Geometries

Degree: Master of Science

Year this Degree Granted: 2003

Permission is hereby granted to the University of Alberta Library to reproduce single copies of this thesis and to lend or sell such copies for private, scholarly or scientific research purposes only.

The author reserves all other publication and other rights in association with the copyright in the thesis, and except as herein before provided, neither the thesis nor any substantial portion thereof may be printed or otherwise reproduced in any material form whatever without the author's prior written permission.

g.
ds Lab

Date: August 22, 2003

University of Alberta

Faculty of Graduate Studies and Research

The undersigned certify that they have read, and recommend to the Faculty of Graduate Studies and Research for acceptance, a thesis entitled **Electrostatic Double Layer Interactions in Confined and Many-Body Geometries** submitted by **Prodip Kumar Das** in partial fulfillment of the requirements for the degree of **Master of Science**.

Date: August 22, 2003

Abstract

In this dissertation, the evaluation of electrostatic double layer interactions between nanoparticles in many-body configurations has been addressed. Two model problems were selected for this work, namely, (i) two nanoparticles confined in "smooth" and "rough" cylindrical capillaries, and (ii) approach of a nanoparticle toward a planar surface containing already deposited particles. The electrostatic interaction force was obtained by solving the non-linear Poisson-Boltzmann equation using finite element analysis. The interaction force experienced by a particle inside a smooth capillary was drastically modified by charging the capillary wall to different surface potentials. Such modulation of forces can be a viable means of moving particles through micro-capillaries in microfluidic devices. Simulations of the electrostatic interactions in rough capillaries indicated that the roughness on the capillary wall can seriously alter the axial force experienced by a particle, which can oscillate between attraction and repulsion. Finally, the simulation for an approaching particle toward a particle array on a charged planar surface indicates that the electrostatic repulsion is significantly diminished in a many-body situation, and use of pairwise addition of binary interactions can grossly overestimate the colloidal forces.

To my parents.

Acknowledgements

First and foremost, my sincere thank and appreciation to my mom Mrs. Nisha R Das, my brothers, and my sisters for bearing with all my tantrums and insanity for the past two years. They have never lost faith in my abilities, and have provided abundance of encouragement and support along my lengthy and sometimes wandering path through graduate school.

I would like to thank my supervisor, Dr. Subir Bhattacharjee, for providing a wealth of opportunities, resources, and motivation, during my study of Colloid science. His timely advice, patience and valuable guidance throughout the period of research leading to this dissertation are also acknowledged. Had he not given me the opportunity to join Colloids and Complex Fluid Laboratory, I doubt I would have learned as much, and enjoyed doing research as much as I did. His talents as a mentor have already had a significant impact on my career direction, and I believe that I will carry much of what I have learned from him throughout my professional pursuits. Other faculties whose guidance, support, and suggestion have been appreciated include my former supervisor Dr. Abhijit Bhattacharyya (currently at University of Arkansas, Little Rock) for his guidance through the early stage of this degree and Dr. Walied Mousssa for his valuable suggestion during early stage of this research and allowing me to use his FEMLAB© software.

I would also like to thank Mrs. Stephanie Bozic, Mrs. Dione Chambers, and Mr. Mirwais Aktary for their incredible support during different phases of the experimental part and providing highly valuable tips during this research.

This research work has been partially supported by funding from University of Alberta Master's Scholarship, provided by the Faculty of Graduate Studies and Research, University of Alberta. Partial financial support from the Alberta Ingenuity Ph.D./M.Sc. Studentship Award provided by the Alberta Heritage Foundation of Science and Technology is also acknowledged. I would also like to thank Dept. of Mechanical Engineering for selecting me for RR Gilpin Memorial Scholarship.

Lastly I wish to thank my friend Mr. AKM Manjur Morshed and Mr. Abdur Rab for their friendly encouragement, suggestion, and support during the last two years, and my CCFLab members Mr. Shahnawaz H Molla and Mr. Jeffry Kemps for their cooperation during the writing phase of this dissertation.

Edmonton, Alberta
August 19, 2003

Prodip K Das

Table of Contents

1 Introduction 1

1.1 Background and Overview 1

1.2 Objectives and Scope 4

1.2.1 Objectives 4

1.2.2 Scope of the Present Study 5

1.3 Organization of the Thesis 7

2 Electrostatic Interaction between Colloidal Particles in Confined Domains: A Literature Review 8

2.1 Introduction 8

2.2 Electrostatic Interaction between Colloidal Particles 10

2.3 Particles in Cavity 13

2.4 Analysis of Particle-Particle Interaction in Cylindrical Domains 15

2.5 Influence of Confining Geometry: Roughness Effect 16

2.6 Summary 19

3 Electrostatic Interaction in Confined Domains 21

3.1 General 21

3.2 Mathematical Modelling of Electrostatic Interaction 22

3.2.1 Governing Equation 22

3.2.2 Computational Geometry and Boundary Conditions . . . 24

3.2.3 Normalization of Governing Equations 27

3.2.4 Calculation of Interaction Force 28

3.3 Numerical Solution Procedure 30

3.3.1 The Finite Element Model 31

3.3.2 Mesh Generation 32

3.3.3 Error Criteria and Adaptive Mesh Refinement 32

3.3.4 Solution Methodology 37
3.4 Validation of Numerical Results 38
3.4.1 Particle-Particle Interaction 38
3.4.2 Hermite Collocation based Numerical Solution 39
3.4.3 Comparison with Finite Element Results 40
3.5 Interaction Force for Particle in a Cylindrical Capillary 43
3.5.1 Potential Distribution and Fields 43
3.5.2 The Interaction Force: Like-Charge Interaction 51
3.5.3 Influence of Proximity of Charged Wall 57
3.5.4 Modulation of Repulsion between Two Particles 59
3.5.5 Interaction Force for Oppositely Charged Cylinder and Particles 64
3.5.6 Summary 72

4 Influence of Roughness on Particle-Particle Electrostatic Interaction 74
4.1 Introduction 74
4.2 Mathematical Modelling 74
4.2.1 Computational Domain, Governing Equation, and Boundary Conditions 75
4.2.2 Generation of a Rough Surface 77
4.2.3 Calculation of Electrostatic Interaction Force 78
4.3 Results and Discussions 79
4.3.1 Potential Distribution and Fields Inside the Rough Capillary 80
4.3.2 Similarly Charged Particles and Capillary 85
4.3.3 Charged Particles Inside an Uncharged Capillary 91
4.3.4 Charged Particles Inside an Oppositely Charged Capillary 96
4.4 Influence of Surface Roughness on the Interaction Force 101
4.5 AFM Measurement of Surface Roughness 104
4.5.1 Fabrication of Micro-channel 104
4.5.2 AFM Width Analysis 105
4.6 Summary 109

5 Many-Body Electrostatic Interactions 111
5.1 Introduction 111

5.2 Mathematical Modelling 112
5.2.1 Geometry and Boundary Conditions 112
5.2.2 Force Formulation 115
5.3 Results and Discussions 116
5.3.1 Particle-Plate Interaction 116
5.3.2 Particle over an Array of Deposited Particles 119
5.3.3 Difficulties of Numerical Solution 121
5.3.4 Comparison of 3-D FEM Simulations with Pairwise Summation Approaches 123
5.4 Concluding Remarks 125

6 Conclusions and Future Work **127**
6.1 Concluding Remarks 127
6.2 Future Work 130

Bibliography **132**

Appendix **141**

A Calculation of Force **141**

B Computer Codes (FEMLAB) **143**

List of Tables

1.1 Magnitudes of the characteristic forces: $T = 300$ K, $a = 1\mu$m, $\mu = 10^{-3}$ Pa-s, $U = 1 \times 10^{-6}$ m/s, $\rho = 10^3$ kg/m^3, $\Delta\rho/\rho = 10^{-2}$, $g = 10$ m/s^2, Hamaker constant, $A = 10^{-20}$ J, $\psi_s = 0.05$ V, $\varepsilon = 10^2$, $\varepsilon_0 = 8.85 \times 10^{-12}$ C/Vm, $k = 1.381 \times 10^{-23}$ J/K [Russel *et al.*, 1991]. 3

3.1 Values of Debye screening length (κ^{-1}) for several electrolyte concentrations and valences at 300K for $\varepsilon = 10^2$, $\varepsilon_0 = 8.85 \times 10^{-12}$ C/Vm, $e = 1.602 \times 10^{-19}$ C, $k = 1.381 \times 10^{-23}$ J/K. 28

3.2 Comparison between the interaction force obtained from adaptive mesh refinement and typical uniform mesh refinement techniques. 34

3.3 Steps of the adaptive process. 36

3.4 Typical values of different governing parameters for 1 mM 1:1 electrolyte for the parameter used in Table 3.1. 39

4.1 Width analysis statistics from atomic force microscope scans of rectangular micro-channels shown in Figure 4.19a. The threshold value represents the vertical height from the base of the channel. 108

4.2 Width analysis statistics from atomic force microscope scans of rectangular micro-channels shown in Figure 4.19b. The threshold value represents the vertical height from the base of the channel. 108

5.1 Steps of the 3-dimensional finite element scheme showing the convergence of the force between the particle and the plate with mesh refinements. 119

5.2 Steps of the 3-dimensional finite element scheme of many-body colloidal system showing the convergence of the force experienced by a particle with mesh refinements. 121

5.3 Comparison of force experienced by a particle approaching towards the previously deposited particles on a charged surface calculated using the HHF expression based pairwise summation method (linearized PB), pairwise summation of Hermite Collocation based numerical calculations (non-linear PB), and current 3-D finite element (FE) calculation for different scaled separation distances. 125

List of Figures

1.1 Typical sizes of the colloidal particles. 2

3.1 Schematic depiction of two spherical colloidal particles inside a cylindrical capillary (a). The particle centers are located on the cylinder axis. The region circumscribed by the broken lines depicts the computational domain, shown in detail in part (b). Utilizing the symmetry around the horizontal axis, the two-dimensional formulation of the governing equation was developed. The arcs BCD and EFG represent the particle surfaces, while the line IJ represents the wall of the cylindrical capillary. The origin of the cylindrical coordinate system is located at O. 25

3.2 Histogram showing the distribution of the mesh qualities for 24511 elements in the mesh. 33

3.3 Adaptive mesh for two particles inside a cylindrical capillary. . . 35

3.4 Variation of the electrostatic interaction force between two identical charged particles in an unbounded electrolyte with scaled separation distance, κh, corresponding to two values of scaled particle size, κa, for (a) constant potential (CP), and (b) constant charge (CC) conditions. Solid lines represent the results from an independent numerical result based on a Hermite collocation technique in a bispherical coordinate system (see text). Symbols represent the finite element results obtained in the present work. 41

3.5 Potential distribution of two spherical constant potential (CP) particles inside an infinitely long cylindrical capillary corresponding to two values cylinder surface potential as shown in the legend. 44

3.6 Variation of scaled potential inside the cylindrical capillary for constant potential (CP) particles at two different locations. Symbols represent the potential along the midplane between particles, and lines represent the variation along the distance of closest approach between the particle surface and the capillary wall at C (see Figure 3.1). 45

3.7 Distribution of the electrostatic field strength in the confined domain for two spherical constant potential (CP) particles corresponding to two values cylinder surface potential as shown in the legend. 46

3.8 Potential distribution of two spherical constant charge (CC) particles inside an infinitely long cylindrical capillary corresponding to two values cylinder surface potential as shown in the legend. . 48

3.9 Variation of scaled potential inside the cylindrical capillary for constant charge (CC) particles at two different locations. Symbols represent the potential along the midplane between particles, and lines represent the variation along the distance of closest approach between the particle surface and the capillary wall at C (see Figure 3.1). 49

3.10 Distribution of the electrostatic field strength in the confined domain for two spherical constant charge (CC) particles corresponding to two values cylinder surface potential as shown in the legend. 50

3.11 Electrostatic interaction force between two particles in a cylindrical capillary corresponding to different cylinder surface potentials. The variations of the scaled electrostatic force with scaled separation between the particles are depicted for a fixed size ratio (λ) of 0.83 and a fixed surface potential, $\Psi_p = -3.0$, on the particles (assuming constant potential particles) for scaled particle sizes $\kappa a = 0.5$ and 1.0. The open symbols in part (b) represent the interaction force between two CP particles in an unbounded electrolyte corresponding to $\kappa a = 1.0$. 52

3.12 Electrostatic interaction force between two particles in a cylindrical capillary corresponding to different cylinder surface potentials. The variations of the scaled electrostatic force with scaled separation between the particles are depicted for a fixed size ratio (λ) of 0.83 and a fixed surface potential, $\Psi_p = -3.0$, on the particles (assuming constant potential particles) for scaled particle sizes $\kappa a = 2.0$ and 5.0. The open symbols in part (b) represent the interaction force between two CP particles in an unbounded electrolyte corresponding to $\kappa a = 5.0$. 53

3.13 Variation of the scaled interaction force between two constant charge (CC) particles corresponding to two values of scaled particle size, $\kappa a = 0.5$ and 1.0, under same conditions as in Figure 3.11. The charge density on the particles was evaluated assuming a surface potential $\Psi_{p,\infty} = -3.0$ on each particle at isolation. The open symbols in part (b) represent the interaction force between two CC particles in an unbounded electrolyte corresponding to $\kappa a = 1.0$. 55

3.14 Variation of the scaled interaction force between two constant charge (CC) particles corresponding to two values of scaled particle size, $\kappa a = 2.0$ and 5.0, under same conditions as in Figure 3.12. The charge density on the particles was evaluated assuming a surface potential $\Psi_{p,\infty} = -3.0$ on each particle at isolation. The open symbols in part (b) represent the interaction force between two CC particles in an unbounded electrolyte corresponding to $\kappa a = 5.0$. 56

3.15 Dependence of the particle-particle interaction force on proximity of the charged capillary wall. The dependence of the scaled interaction force between two constant potential (CP) particles on the size ratio λ is shown for several values of the cylinder surface potential. 58

3.16 Dependence of the scaled particle-particle interaction force on λ for constant charge (CC) particles. Except for the CC boundary condition on the particles, all other parameters are same as in Figure 3.15. 59

3.17 Interaction force at different scaled separations between constant potential (CP) particles corresponding to scaled cylinder surface potential, $\Psi_c = -3.0$ for different size ratios (λ). The solid line depicts the interaction force between two particles in an unbounded electrolyte. 61
3.18 Interaction force at different scaled separations between constant potential (CP) particles corresponding to scaled cylinder surface potential, $\Psi_c = 0.0$ for different size ratios (λ). The solid line depicts the interaction force between two particles in an unbounded electrolyte. 61
3.19 Interaction force at different scaled separations between constant potential (CP) particles corresponding to scaled cylinder surface potential, $\Psi_c = +3.0$ for different size ratios (λ). The solid line depicts the interaction force between two particles in an unbounded electrolyte. 62
3.20 Interaction force at different scaled separations between constant charge (CC) particles corresponding to scaled cylinder surface potential, $\Psi_c = -3.0$. The solid line depicts the interaction force between two particles in an unbounded electrolyte. 62
3.21 Interaction force at different scaled separations between constant charge (CC) particles corresponding to scaled cylinder surface potential, $\Psi_c = 0.0$. The solid line depicts the interaction force between two particles in an unbounded electrolyte. 63
3.22 Interaction force at different scaled separations between constant charge (CC) particles corresponding to scaled cylinder surface potential, $\Psi_c = +3.0$. The solid line depicts the interaction force between two particles in an unbounded electrolyte. 63

3.23 Electrostatic interaction force between two constant potential (CP) particles inside an oppositely charged cylindrical capillary as indicated in the legend. The variations of the scaled electrostatic force with scaled separation between the particles are depicted for a fixed size ratio (λ) of 0.83 and a fixed surface potential, $\Psi_p = -3.0$, on the particles (assuming constant potential particles) for two values of scaled particle size, $\kappa a = 0.5$ and 1.0. The open symbols in part (b) represent the interaction force between two CP particles in an unbounded electrolyte corresponding to $\kappa a = 1.0$. 65

3.24 Electrostatic interaction force between two constant potential (CP) particles inside an oppositely charged cylindrical capillary as indicated in the legend. The variations of the scaled electrostatic force with scaled separation between the particles are depicted for a fixed size ratio (λ) of 0.83 and a fixed surface potential, $\Psi_p = -3.0$, on the particles (assuming constant potential particles) for two values of scaled particle size, $\kappa a = 2.0$ and 5.0. The open symbols in part (b) represent the interaction force between two CP particles in an unbounded electrolyte corresponding to $\kappa a = 5.0$. 66

3.25 Variation of the scaled interaction force between two constant charge (CC) particles corresponding to two values of scaled particle size, $\kappa a = 0.5$ and 1.0, under same conditions as in Figure 3.23. The charge density on the particles was evaluated assuming a surface potential $\Psi_{p,\infty} = -3.0$ on each particle at isolation. The open symbols in part (b) represent the interaction force between two CC particles in an unbounded electrolyte corresponding to $\kappa a = 1.0$. 69

3.26 Variation of the scaled interaction force between two constant charge (CC) particles corresponding to two values of scaled particle size, $\kappa a = 2.0$ and 5.0, under same conditions as in Figure 3.24. The charge density on the particles was evaluated assuming a surface potential $\Psi_{p,\infty} = -3.0$ on each particle at isolation. The open symbols in part (b) represent the interaction force between two CC particles in an unbounded electrolyte corresponding to $\kappa a = 5.0$. 70

3.27 Interaction force between two identically charged particles inside an oppositely charged capillary. The variation of the force with size ratio is shown for different cylinder surface potentials. Part (a) depicts the scaled interaction force for constant potential (CP) particles, while part (b) shows the scaled interaction force for constant charge (CC) particles. 71

4.1 Schematic representation of the computational domain for two spherical colloidal particles inside a "rough" capillary. (a) particles are moving uniformly from the crest of an undulation denoted by the point R (Case−I), (b) particles are moving uniformly from the trough of an undulation (Case−II). Utilizing the symmetry around the horizontal axis (AH), the two-dimensional formulation of the governing equation was developed. The arcs BCD and EFG represent the particle surfaces, while IJ represents the undulation of the capillary. The origin of the cylindrical coordinate system is located at O. 76

4.2 Potential distribution of two spherical particles inside an infinitely long "rough" capillary corresponding to three different capillary surface potentials as mentioned in the legend for the situation when particles are moving uniformly from the crest of an undulation (Case−I). 81

4.3 Electrostatic field distribution inside an infinitely long "rough" capillary corresponding to three different capillary surface potentials as mentioned in the legend for Case−I. 82

4.4 Potential distribution of two spherical particles inside an infinitely long "rough" capillary corresponding to three different capillary surface potentials as mentioned in the legend for the situation when particles are moving uniformly from the trough of an undulation (Case−II). 83
4.5 Electrostatic field distribution inside an infinitely long "rough" capillary corresponding to three different capillary surface potentials as mentioned in the legend for Case−II. 84
4.6 Variations of the scaled electrostatic interaction force between two spherical particles inside a "rough" capillary with scaled separation distance when the particles are moving uniformly from the crest of an undulation (Case−I). Both particles and capillary are similarly charged ($\Psi_p = \Psi_c = -3.0$) and different line types correspond to different values of scaled amplitude (η) of the roughness as indicated in the legend. Two figures represent the two values scaled wavelength of the undulation, (a) $\xi = 0.4$ and (b) $\xi = 1.0$. The open symbols depict the interaction force between two CP particles in a smooth ($\eta = 0.0$) cylindrical capillary. 86
4.7 Variations of the scaled electrostatic interaction force between two spherical particles inside a "rough" capillary with scaled separation distance when the particles are moving uniformly from the crest of an undulation (Case−I) under same conditions as in Figure 4.6. Two figures represent the two values scaled wavelength of the undulation, (a) $\xi = 2.0$ and (b) $\xi = 4.0$. 87
4.8 Scaled electrostatic interaction force between two spherical particles as a function of scaled separation distance when the particles are moving uniformly from the trough of an undulation (Case−II) under same conditions as in Figure 4.6 for two values scaled wavelength of the undulation, (a) $\xi = 0.4$ and (b) $\xi = 1.0$. 89
4.9 Scaled electrostatic interaction force between two spherical particles as a function of scaled separation distance when the particles are moving uniformly from the trough of an undulation (Case−II) under same conditions as in Figure 4.7 for two values scaled wavelength of the undulation, (a) $\xi = 2.0$ and (b) $\xi = 4.0$. 90

4.10 Variation of the scaled electrostatic interaction force between two similarly charged particles inside an uncharged "rough" capillary with scaled separation distance for Case−I corresponding to two values scaled wavelength of the undulation, (a) $\xi = 0.4$ and (b) $\xi = 1.0$. Simulations were performed under same boundary conditions as in Figure 4.6, except for zero surface potential on the capillary wall ($\Psi_c = 0.0$). The open symbols depict the interaction force between two CP particles in a smooth ($\eta = 0.0$) cylindrical capillary. 92

4.11 Variation of the scaled electrostatic interaction force between two similarly charged spherical particles inside an uncharged "rough" capillary with scaled separation distance for Case−I corresponding to two values scaled wavelength of the undulation, (a) $\xi = 2.0$ and (b) $\xi = 4.0$. Simulations were performed under same boundary conditions as in Figure 4.10. 93

4.12 Variation of the scaled electrostatic interaction force between two similarly charged particles inside an uncharged ($\Psi_c = 0.0$) "rough" capillary with scaled separation distance for Case−II under same conditions as in Figure 4.10 for two values scaled wavelength of the undulation, (a) $\xi = 0.4$ and (b) $\xi = 1.0$. . . . 94

4.13 Variation of the scaled electrostatic interaction force between two similarly charged particles inside an uncharged ($\Psi_c = 0.0$) "rough" capillary with scaled separation distance for Case−II under same conditions as in Figure 4.11 for two values scaled wavelength of the undulation, (a) $\xi = 2.0$ and (b) $\xi = 4.0$. . . . 95

4.14 Variation of the scaled particle-particle interaction force between two similarly charged spherical particles inside an oppositely charged capillary with scaled separation distance for Case−I. The scaled surface potential on the capillary wall is $\Psi_c = +3.0$, while the particle surface potential is given by $\Psi_p = -3.0$. All other conditions are as in Figure 4.6. Two figures represent the two values scaled wavelength of the undulation, (a) $\xi = 0.4$ and (b) $\xi = 1.0$. 97

4.15 Variation of the scaled particle-particle interaction force between two similarly charged spherical particles inside an oppositely charged capillary with scaled separation distance for Case−I corresponding to two values scaled wavelength of the undulation, (a) $\xi = 2.0$ and (b) $\xi = 4.0$ under same conditions as in Figure 4.14. 98
4.16 Variation of the scaled particle-particle interaction force between two similarly charged spherical particles inside an oppositely charged capillary with scaled separation distance for Case−II under same conditions as in Figure 4.14 for two values scaled wavelength of the undulation, (a) $\xi = 0.4$ and (b) $\xi = 1.0$. 99
4.17 Variation of the scaled particle-particle interaction force between two similarly charged spherical particles inside an oppositely charged capillary with scaled separation distance for Case−II under same conditions as in Figure 4.15 for two values scaled wavelength of the undulation, (a) $\xi = 2.0$ and (b) $\xi = 4.0$. 100
4.18 Microscope image of micro-fabricated mask in part (a) and corresponding microscope image of aluminium coated Si-wafer after etching in part (b) showing an array of rectangular micro-channels. 105
4.19 Atomic force microscope (AFM) image of micro-fabricated rectangular channels showing an array of, (a) 5 μm wide and (b) 6 μm wide rectangular micro-channels of *ca.* 0.45 μm deep etched on an aluminum film. 106
4.20 Atomic force microscope (AFM) image of micro-fabricated rectangular channels showing the procedure of measuring surface roughness by width analysis. Top view of patterned surface showing the section over which the width analysis is performed. The dashed rectangular box is placed on each channel and the width of the channel is measured by recording the lengths of all the horizontal scan lines (horizontal white lines) spanning the width of the channel. The measurements are performed at different channel heights. 107

5.1 Schematic depiction of a patterned planar surface showing an array of square grid with deposited particles. 113

5.2 Geometry showing the details of the finite element computational domain shown in the Figure 5.1. Part (a) depicts side view of the computational domain with geometrical parameters while part (b) shows top view along with the coordinates of the center of each particle. 114
5.3 Finite element mesh showing tetrahedron meshes for the geometry under consideration. 115
5.4 Comparison of the electrostatic interaction force between a charged particles and a charged planar surface obtained from finite element simulation with the corresponding estimates from Hogg *et al.* (1966). Solid line represents the result of the analytical HHF expression Eq. (5.2), while dashed line represents the result of 2-dimensional finite element method. Symbols represent the 3-dimensional finite element results obtained under identical geometry and boundary conditions as 2-D finite element model. 118
5.5 Potential distribution of many-body colloidal interaction when a particle approaching toward the previously deposited particles (top). A detail of the middle slice is depicted in bottom part. . . 120

List of Symbols

a	particle radius
a_1	radius of the deposited particle
a_2	radius of the probe particle
b	mean capillary radius
d	center-center separation distance between two particles
e	electronic charge (1.6×10^{-19} C)
$\mathbf{E}$	electrostatic field vector
E_x, E_y, E_z	components of electrostatic field vector $\mathbf{E}$
f	scaled force $\left(=\frac{F}{\varepsilon\varepsilon_0}\left(\frac{\nu e}{kT}\right)^2\right)$
f_z	scaled force acting along z direction
$\mathbf{F}$	force
F_z	component of force acting along the z direction
h	surface-surface separation distance between two particles
$\mathbf{I}$	identity tensor
k	Boltzmann constant (1.38×10^{-23} JK^{-1})
$\mathbf{k}$	unit normal in the positive z direction
L	surface-surface separation distance between deposited particles in $x-y$ plane
$\mathbf{n}$	unit normal vector
n_i	ionic number concentration of i^{th} species (m^{-3})
$n_{i\infty}$	number concentration of i^{th} ionic species in the bulk solution (m^{-3})

n_r, n_z	components of the unit normal along the r and z directions, respectively
n_x, n_y, n_z	components of the unit normal along the x, y, and z directions, respectively
q_p	surface charge density (Cm^{-2})
Q_p	total surface charge (C)
r	radial coordinate in the polar coordinate system
$\bar{r}$	scaled radial coordinate
T	absolute temperature (K)
T_{ij}	component of stress tensor
z	axial coordinate in the polar coordinate system
$\bar{z}$	scaled axial coordinate

Greek Symbols

α	amplitude of undulation on rough capillary wall
δ	pitch of undulation on rough capillary wall
ε_0	dielectric permittivity of vacuum (8.8542×10^{-12} C^2 N^{-1} m^{-2})
ε	dielectric permittivity of electrolyte solution
η	scaled amplitude of the undulation $\left(=\frac{\alpha}{a}\right)$
κ	inverse Debye screening length (m^{-1})
λ	size ratio $\left(=\frac{a}{b}\right)$
∇^2	Laplacian operator
$\partial\Omega$	boundary of the computational domain
ν	absolute value of the valency for a symmetric ($\nu : \nu$) electrolyte solution
ψ	electric potential (V)
ψ_c, ψ_p, ψ_s	surface potentials of cylinder, particle, and planar surface, respectively (V)

Ψ	scaled surface potential $\left(= \frac{\nu e \psi}{kT}\right)$
Ψ_c, Ψ_p	scaled surface potentials of cylinder and particle, respectively
$\Psi_{p,\infty}$	surface potential of an isolated spherical particle
Ψ_r, Ψ_z	electric field vector along the r and z directions, respectively
Π	osmotic pressure
σ_p	scaled surface charge density
ξ	scaled pitch of the undulation $\left(=\frac{\delta}{a}\right)$

Abbreviations

AFM	atomic force microscope
CC	constant charge
CP	constant potential
DA	Derjaguin approximation
DLVO	Derjaguin–Landau–Verwey–Overbeek
EDL	electrostatic double layer
FEM	Finite Element Method
LPB	linearized Poisson–Boltzmann
LSA	linear superposition approximation
LW	Lifshitz–van der Waals
NLPB	non–linear Poisson–Boltzmann
PB	Poisson–Boltzmann
PDE	partial differential equation

Chapter 1

Introduction

1.1 Background and Overview

The term *colloid* comes from Greek word '$\kappa\acute{o}\lambda\lambda\alpha$', meaning glue. Any particle that has some linear dimension ranging from 10^{-9} m (= 1 nm) to $\sim 10^{-5}$ m (= 10 μm) is considered as a colloid. For instance, pulverized coal, bacteria, viruses, silica particles, red blood cells etc. are considered to be colloids, whereas molecules and ions are small in size compared to colloids. However, there are some molecules (e.g. proteins, polysaccharides) that are individually larger than 1 nm in size and can often form a colloidal system. Typical particle sizes for some colloidal systems are given in Figure 1.1.

Generally, a colloidal dispersion is a suspension of finely divided solids or liquids (dispersed phase) in a continuous medium of liquids or gases known as the dispersing medium. Some examples of colloidal dispersions include aerosols (liquid droplets in gas), milk (liquid in liquid), smoke (solid particles in gas), and paint (solid particles in liquid). In a dispersing medium (like water), colloids usually acquire some charge. Surface charge can arise from either surface ionization, or dissociation, or adsorption. No matter what the charging mechanism is, the presence of a charged surface in a solution will set up an electrostatic field in the solution.

Due to this electrostatic field, colloidal particles exhibit an astonishingly

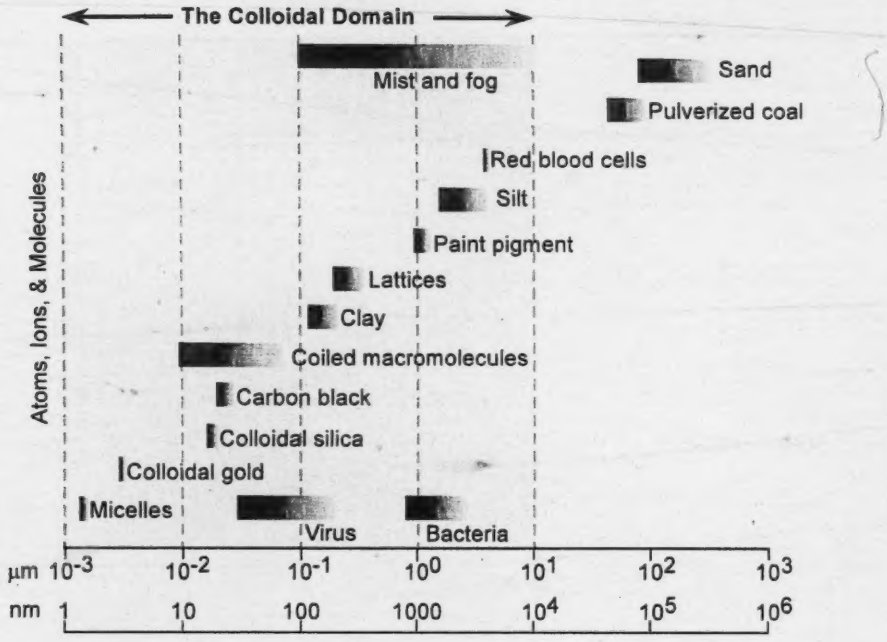

Figure 1.1: Typical sizes of the colloidal particles.

diverse range of physical and chemical behaviours in an aqueous medium. The overall nature of a colloidal system can be affected by the following factors [Masliyah, 1994]:

- Particle size and shape
- Surface properties, both chemical and physical
- Chemical and physical properties of the dispersed phase
- Particle-particle interaction
- Particle-dispersing medium interaction

Various interaction forces that can modify the nature of a colloidal system are: electrostatic interaction force, Lifshitz-van der Waals (LW) force, Brownian force, viscous force, inertial force, gravitational force, and surface tension [Israelachvili, 1991; Masliyah, 1994]. Some typical magnitudes of characteristic

$\frac{\text{electrostatic force}}{\text{Brownian force}}$	$\frac{\varepsilon\varepsilon_0{\psi_s}^2}{kT/a}$	$\approx 10^3$
$\frac{\text{LW force}}{\text{Brownian force}}$	$\frac{A/a}{kT/a}$	≈ 1
$\frac{\text{Brownian force}}{\text{viscous force}}$	$\frac{kT/a}{\mu U a}$	≈ 1
$\frac{\text{gravitational force}}{\text{viscous force}}$	$\frac{a^3 g \Delta\rho}{\mu U a}$	$\approx 10^{-1}$
$\frac{\text{inertial force}}{\text{viscous force}}$	$\frac{\rho a^2 U^2}{\mu U a}$	$\approx 10^{-6}$

Table 1.1: Magnitudes of the characteristic forces: $T = 300$ K, $a = 1\mu$m, $\mu = 10^{-3}$ Pa-s, $U = 1 \times 10^{-6}$ m/s, $\rho = 10^3$ kg/m^3, $\Delta\rho/\rho = 10^{-2}$, $g = 10$ m/s^2, Hamaker constant, $A = 10^{-20}$ J, $\psi_s = 0.05$ V, $\varepsilon = 10^2$, $\varepsilon_0 = 8.85 \times 10^{-12}$ C/Vm, $k = 1.381 \times 10^{-23}$ J/K [Russel *et al.*, 1991].

forces are listed in Table 1.1. For the particular values chosen, it is clear that the ratios of both electrostatic force to Brownian force and Lifshitz-van der Waals force to Brownian force are several orders of magnitude higher compared the ratio of inertial to viscous forces. Thus, both electrostatic and Lifshitz-van der Waals forces play the most significant role in dictating colloidal stability. The Lifshitz-van der Waals force between similar particles in a medium is always attractive. On the other hand, similarly charged particles always exhibit electrostatic repulsion, and due to this repulsive force, particles can avoid sticking together, thereby reducing the coagulation rate. This kind of colloidal stability was first explained by Derjaguin, Landau, Verwey, and Overbeek in their theory of colloidal stability [Derjaguin and Landau, 1941; Verwey and Overbeek, 1948].

The ability of a dispersion to resist coagulation may be either 'kinetic' or 'thermodynamic' and has traditionally been the primary focus of colloid science. Many of the major disciplines of science and engineering, including analytical chemistry, biochemistry and biochemical engineering, biological science, chemical manufacturing, environmental science, fluid engineering, materials science,

medical science, petroleum science, physical chemistry, and process engineering, have been greatly influenced by the concept of colloid stability [Heimenz and Rajagopalan, 1997]. Stability of colloids plays a dominant role in many separation processes. Colloidal interactions in aqueous solutions can also determine the rate of many dynamic phenomena occurring in dispersions, such as aggregation, coagulation, flocculation, and particle capture. In the past two decades, colloidal phenomena have also received more attention due to rapid developments in micro-electromechanical systems (MEMS) and nanotechnology. The renewed interest has primarily focused on the electrokinetic transport phenomena of colloidal systems for moving fluids in confinements (or channels) that have extremely small dimensions. Traditional fluid handling devices are incapable of handling the requirements of the microfluidic applications. Consequently, there has been an immense effort toward the exploration of alternative means of fluid transport in microscopic capillaries. Electrokinetic transport mechanisms constitute the most suitable fluid handling processes for microfluidic applications.

1.2 Objectives and Scope

1.2.1 Objectives

A current emphasis in microfluidics research is to move extremely small volumes of complex fluids through micro-capillaries for controlled delivery of substances in devices like micro-arrays and "labs-on-a-chip" for biological and chemical analyses. The main advantages of microfluidic devices over conventional macroscopic methods of such analyses are the potential for automation, small sample volumes, and a significant reduction in labour required to perform certain analyses. However, due to the miniaturized scale, the transport of fluids in microfluidic devices becomes a challenging problem. For instance, in the colloid regime, charged dispersions and sterically stabilized colloids show elastic behavior, whereas, when the particle-particle interactions are not important, they behave like ordinary liquids [Heimenz and Rajagopalan, 1997]. Therefore,

it becomes important to understand how the interaction forces between the colloidal particles affect the overall behaviour of complex dispersions. Furthermore, dealing with nanoparticles in confined geometries of comparable dimensions can lead to considerable alterations in the interaction forces that govern colloidal behaviour. In this thesis, the primary goal is to examine the electrostatic interaction between colloidal particles in microscopic channels, which will subsequently lead to the exploration of the microscopic behavior of colloids in electrokinetics. Here the fundamental issues like, what is the influence of the confinement on electrostatic interaction between colloidal nanoparticles and is there any influence of surface heterogeneity on the net interaction between nanoparticles have been addressed. The issue of many-body effects on the electrostatic interaction between nanoparticles has also been addressed. This study has the following major research objectives:

a) Develop a model to investigate the electrostatic double layer interactions in a microscopic channel and explore the behaviour of colloidal nanoparticles in a confined space.

b) Provide a computational scheme for calculating the electrostatic double layer interaction force between colloidal nanoparticles in confined geometries for different surface properties of the colloidal particles and the confining walls.

c) Investigate the influence of the roughness of the confining geometry on the electrostatic interaction forces.

d) Study the many-body effects on the electrostatic double layer force experienced by a nanoparticle.

1.2.2 Scope of the Present Study

The Derjaguin-Landau-Verwey-Overbeek (DLVO) interaction between colloidal particles is usually treated as the central pillar for understanding many natural

and industrial processes involving colloidal particles such as flow through porous media, deposition of particles, capillary electrophoresis, chromatographic separations, microfluidic actuation, and membrane separations [Masliyah, 1994; Elimelech *et al.*, 1995]. In the original DLVO theory, it was assumed that the interacting bodies are in an infinite medium. However, in real systems, most colloidal interactions occur in confined domains, like porous media or microscopic channels, where particles simultaneously interact with other particles and the wall of the confining geometry. In this investigation, a model problem of two colloidal particles in a micro-capillary is considered, for which a finite element model for electrostatic double layer interactions is developed. Since all surfaces are inherently rough at small length scales, subsequently the surface roughness of the capillary wall is also incorporated to get a more realistic picture of the colloidal interactions in a capillary that can apply to processes like porous media flow or flow through a membrane pore. Finally, the electrostatic interaction is studied for the case when a charged nanoparticle approaches a planar surface containing previously deposited particles, which is a typical scenario of many-body colloidal interactions observed during particle transport in porous media and particle deposition.

The findings of this work will have direct bearing on the flow of colloidal suspensions through micro-capillaries, porous media, and membranes. It also seems possible to utilize the oscillatory behaviour of electrostatic force due to the variations of the cylindrical capillary wall surface potential and morphology to move a particle through micro-capillaries for controlled delivery of fluids in devices like micro-arrays and "labs-on-a-chip". More specifically, electrostatic actuation techniques based on this study could be employed in the development of microfluidic devices (like micro-valves and micro-pumps) for controlled delivery of small volumes (μl to nl) of fluids.

1.3 Organization of the Thesis

In this chapter, a brief overview of the role of electrostatic interactions in colloidal systems has been presented, followed by a description of the objectives and scope of the present study. Chapter 2 presents a detailed and critical review of the existing studies related to the present investigation, including a discussion on their limitations and scopes of further work. In Chapter 3, a mathematical model of electrostatic double layer interaction between two nanoparticles inside a long smooth cylindrical capillary is presented along with numerical techniques, solution methodology, and numerical results. Chapter 4 deals with the particle-particle electrostatic interaction inside an infinitely long "rough" capillary. Chapter 5 describes a 3-dimensional (3D) model of many-body electrostatic interactions for a particle approaching a flat surface containing previously deposited particles. Finally, some significant conclusions drawn from the present investigation are given in Chapter 6. This chapter also contains suggestions for future work in this field.

Chapter 2

Electrostatic Interaction between Colloidal Particles in Confined Domains: A Literature Review

2.1 Introduction

The understating of colloidal phenomena is primarily based on the model of interparticle interaction potential originally proposed by Derjaguin, Landau, Verwey, and Overbeek [Derjaguin and Landau, 1941; Verwey and Overbeek, 1948]. This interaction potential, referred to as the DLVO potential, underlies theories of colloidal stability, colloid transport and deposition, electrokinetic phenomena, and nearly every mathematical treatment of colloidal systems. The DLVO interaction potential is comprised of two types of interaction between colloidal particles, namely, the Lifshitz-van der Waals (LW) interaction, which is predominantly attractive for similar particles (particles with same material composition), and the electrostatic double layer (EDL) interaction, which may be attractive or repulsive depending on how the particle surfaces are charged up in an electrolyte solution. The immense variation of the electrostatic double layer interaction, brought about by variations in electrolyte concentration of the dispersing medium, pH of the medium, and several other physical and

chemical conditions, leads to the diversity of colloidal behaviour. The primary limitation of the DLVO interaction potential is that it is a "pair potential". In other words, this potential represents the interaction between only two colloidal entities suspended in an infinitely large medium. Clearly, it is unrealistic for systems which have a high concentration of particles or for confined systems, where the walls of the confining domain interact with the particles. While most natural and engineered systems should be subject to many-body interactions arising from the presence of several particles or a confining wall, the theoretical treatment of these systems often neglects the many-body interactions and their role in modifying colloidal phenomena.

Calculation of the Lifshitz-van der Waals (LW) interaction using Hamaker's microscopic approach is based on the assumption that the interactions between a pair of atoms can be added together to obtain the total interaction between two particles (macro-bodies). Based on this assumption, the simplest procedure for calculating the LW force between colloidal particles is the pairwise summation of interatomic Lennard-Jones forces, which is known as Hamaker's pairwise summation approach [Hunter, 2001]. This pairwise addition of interatomic forces gives remarkably accurate predictions of LW interactions between small colloidal particles at small separations, although at large separations the "retardation effect" can slightly modify the net LW interaction between the particles. Therefore, the many-body LW interactions can be addressed fairly accurately using Hamaker's approach. This is, however, not possible for EDL interactions.

Literature related to the electrostatic double layer (EDL) interaction is mainly based on Debye-Hückel approximation, Derjaguin approximation, or Linear Superposition approximation. All of these methods have some sort of limitation. For instance, the Debye-Hückel approximation is a linearized model and is valid for low surface potentials, the Derjaguin approximation (DA) is valid only when the particle-particle separation and Debye length are small relative to the particle dimension, and the Linear Superposition approximation

(LSA) is valid only in the far-field limit, *i.e.*, for separations of several double layer thickness [Hunter, 2001; White, 1983; Bell *et al.*, 1970]. Due to these limitations, models based on the above mentioned methods can only deal with special cases of colloidal interaction. Furthermore, all these approaches provide the EDL interaction for only a pair of particles, and cannot be readily adopted for calculation of EDL interactions in the many-body case. The only possible way to correctly estimate the EDL interaction will be through a detailed numerical solution of the non-linear Poisson-Boltzmann (NLPB) equation. Based on this, the present investigation is limited to the EDL part of the colloidal interactions. In the following sections, previous work related to colloidal interaction in infinite domains and interaction inside confined domains have been discussed.

2.2 Electrostatic Interaction between Colloidal Particles

As stated earlier, among the two components of the DLVO interaction, the electrostatic double layer interaction is susceptible to immense variations with several operating and physico-chemical conditions like ionic strength of the suspending medium, the charging behavior of the interfaces, the dielectric property of the solvent, and geometry of the particles and the confining domain. Accordingly, the nature and magnitude of the electrostatic interactions are usually the primary governing parameters that dictate the overall macroscopic behaviour of colloidal systems near interfaces and in confined domains. Due to the predominance of electrostatic double layer interaction, numerous attempts have been made to derive and develop the model for electrostatic interaction between two charged entities in an infinite domain. Among them, Hogg *et al.* (1966) proposed a quantitative theory to describe the kinetics of coagulation of colloidal dispersions. A general expression was developed to describe the particle-particle interaction for two dissimilar spherical particles. However, their mathematical

formulation, which is based on the linearized Poisson-Boltzmann (LPB) equation, is valid only for low particle surface potential and symmetric electrolytes. Later, Ohshima *et al.* (1983) modified the Hogg-Healy-Fuerstenau formulas for the interaction of dissimilar double layers and incorporated the curvature correction for the interacting spheres. Bell *et al.* (1970) used Linear Superposition approximation (LSA) to calculate the double layer free energy of interaction for two charged colloidal particles. The main advantage of their method over the Hogg-Healy-Fuerstenau formulae is, this formulation can handle unequal particle radii at a large separation distance. However, this approximation gives better result only for large values of particle radius with constant surface potential. White (1977) obtained a series solution of the Poisson-Boltzmann equation for spherical particles. A more detailed solution of the Poisson-Boltzmann equation for electrostatic repulsion between charged spheres was provided by Glendinning and Russel (1983). They obtained a series solution of the linearized Poisson-Boltzmann based on multipole expansion. The interparticle interaction force was calculated for constant surface potential and constant charge density. They also showed that the Derjaguin approximation is inaccurate in the case of constant charge density.

The original DLVO theory is based on the assumption that the electric potential at a particle surface remains constant during the approach of another particle, which means that the surface charge density must change on approach. However, colloidal systems such as clays and latex particles maintain a constant surface charge density on approach. It should also be noted that, most charged interfaces in aqueous electrolyte media tend to obey some form of a charge regulatory behaviour. Several attempts have also been made to calculate the interaction between diffuse double layers both for constant charge case and charge regulatory behaviour [Gregory, 1973; Gregory, 1975; Carnie and Chan, 1993*b*]. Carnie and Chan (1993*a*) had considered the cases of constant surface potential, constant surface charge, and charge regulation to calculate interaction free energy between two spherical particles. McCormack *et al.* (1995) calculated the

electric double layer force and interaction free energy between two flat plates for both constant potential and constant charge boundary. In addition to the cases of similar surface potential or surface charge, McCormack *et al.* also considered the cases in which one surface is maintained at constant potential and the other maintains constant surface charge density. All these studies indicate that the LPB seriously overestimates the EDL interactions under constant charge (CC) conditions, and it is important to resort to solution of the non-linear Poisson-Boltzmann equation for CC boundary conditions.

Due to the non-linear characteristic of the Poisson-Boltzmann (PB) equation, only few attempts have been made to solve the PB equation for complicated geometries. However, in the recent years, a handful of mathematical formulations and numerical schemes have been proposed for solving non-linear Poisson-Boltzmann equation for different simple geometries and physical parameters. These include, for instance, interaction between two parallel plates [Ohshima *et al.*, 1987], interaction between two parallel cylinders [Ohshima, 1996; Harries, 1998], interaction between two charged spheroids [Hsu and Liu, 1997], sphere-plate interaction [Ohshima and Kondo, 1993; Carnie *et al.*, 1994*a*; Stankovich and Carnie, 1996; Warszynski and Adamczyk, 1997; Ohshima, 1998], a sphere and a cylinder [Mark *et al.*, 2000], a cylinder and a planar surface [Ohshima, 1999], interactions of bodies bearing thin double-layers [Adamczyk *et al.*, 1990*a*; Adamczyk *et al.*, 1990*b*; Adamczyk *et al.*, 1991*a*; Adamczyk *et al.*, 1991*b*], and interaction between a particle and a liquid interface [Chan *et al.*, 2001].

Hoskin (1956) and Hoskin and Levine (1956) made the first attempt to solve the Poisson-Boltzmann equation numerically for two identical spherical colloidal particles using finite difference scheme. McCartney and Levine (1969) used a similar finite difference method to calculate the interaction between two identical particles under constant surface potential. However, they reported the results for relatively small mesh sizes (30×40). In both cases, the force between two particles was calculated for constant potential boundary condition only.

Later, Ledbetter *et al.* (1981) studied the interaction between two charged particles under both constant surface potential and constant surface charge density boundary conditions on the particle surface using finite difference approach for larger mesh sizes (50×50). All of these studies used second order finite difference discretization scheme. More recently, a fourth order discretization scheme combined with Newton-Raphson iteration method was used by Carnie *et al.* (1994*a*) to calculate the double layer force between two spherical colloidal particles . In both of these cases, the actual problem was transformed into the bispherical coordinate system, which will be cumbersome for geometries other than that of two spherical particles. Later Warszynski and Adamczyk (1997) used similar coordinate transformation for sphere/plane geometry as well. Chan *et al.* (1983) provided a numerical solution of electric double layer interaction between spherical colloidal particles using finite element method. Based on the above, it is evident that numerical solutions of PB equation available in literature are primarily based on finite difference techniques using appropriate coordinate transformations. Application of finite element technique is very rare for the case of particle-particle interactions.

2.3 Particles in Cavity

Colloid transport through cylindrical pores is important in a variety of applications, specially for colloid transport through porous media and membrane separations [Masliyah, 1994; Elimelech *et al.*, 1995]. Due to the geometrical complexity, only few attempts have been made to calculate the EDL interaction between a particle and a cylindrical capillary. Smith and Deen (1980, 1983) first showed some theoretical results for electrostatic double layer interaction between a colloid particle and the wall of a charged cylindrical pore of infinite length. Analytical expressions for the potential energy of interaction for both constant surface potential and constant surface charge density were presented using linearized Poisson-Boltzmann model. Later, Pujar and Zydney (1997)

provided the results for charge regulation condition using the basic procedure developed by Smith and Deen. On the other hand, Papadopoulos and Kuo (1990) provided the numerical results for the Lifshitz-van der Waals interactions for a spherical particle inside a cylindrical pore. Hofman and Stein (1992) calculated both the LW and the EDL interactions on a particle approaching a conical constriction in a pore. An analytical expression was derived for the LW interaction whereas the EDL interaction was calculated by numerically solving the Poisson-Boltzmann equation. Bhattacharjee and Sharma (1995) also present the details of the analytical calculation of LW interaction for similar geometry. Compared to Papadopoulos and Kuo's approach, they showed that choosing the proper elements for pairwise summation, one can analytically evaluate five of the six nested integrations required to calculate the LW interaction. Later, they proposed a Surface Element Integration (SEI) technique to determine both the LW and the EDL interactions between spherical particles in cylindrical pores [Bhattacharjee and Sharma, 1997]. Bowen and Sharif (1997) used finite element technique for assessing the interaction on a charged spherical particle at various distances during approach and entry into a charged cylindrical pore. In their finite element scheme, they implemented the adaptive mesh refinement procedure, which is an effective technique to minimize errors in finite element solutions. They also presented analytical expressions for both the energy and the force between a charged spherical particle and a cylindrical pore [Bowen *et al.*, 1999]. It should be noted that all of these works are limited to the single particle inside a cylindrical pore or cavity; however, in colloid transport through capillaries, it is more probable to have two or more particles in close proximity inside a capillary.

2.4 Analysis of Particle-Particle Interaction in Cylindrical Domains

In the previous two sections, literature related to particle-particle interaction in an infinitely large medium, and interaction between a spherical particle and cylindrical pore have been discussed. However, in natural and industrial processes, colloidal interactions usually occur in a confined domain, and the net interaction evolves from many-body effects. Particle-particle interaction in confined domains has not been investigated to a great extent because of complexity of mathematical modelling. In the recent years, considerable attention has been devoted toward the calculation of electrostatic double layer interaction between colloidal particles in a confined domain [Ospeck and Fraden, 1998; Bowen and Sharif, 1998; Bowen and Sharif, 1999; Gray *et al.*, 1999; Sader and Chan, 1999*a*; Sader and Chan, 1999*b*; Sader and Chan, 2000; Bowen and Williams, 2002]. Most of these theoretical studies were spurred by the experiments that indicated the existence of a long-range attraction between two colloidal particles in a confined domain [Larsen and Grier, 1997]. Although it has become increasingly apparent that the long-range attraction observed in these experiments could not be replicated in the framework of the Poisson-Boltzmann (PB) theory [Sader and Chan, 1999*a*; Sader and Chan, 2000], there still remains a scope of exploring the short-range electrostatic interaction between colloidal particles in a confined space in the framework of the PB equation.

A variety of numerical solution schemes for the Poisson-Boltzmann equation has already been discussed in the previous two sections. Most of these numerical studies primarily deal with the solution of the PB equation to obtain the interaction between two spherical colloidal particles, or that between a particle and an infinite planar surface. These studies primarily rely on finite difference techniques, and generally employ coordinate transformations to map the physical space into a rectangular computational grid. This kind of mapping only works for simple geometries. Application of finite element techniques or its general-

izations are relatively less prevalent, and only recently several studies exploring the solution of the PB equation for different geometries using this technique have appeared in literature [Gray *et al.*, 1999; Bowen and Sharif, 1997*a*; Bowen and Sharif, 1997*b*]. Predominantly, the problem addressed using this technique involves the evaluation of the electrostatic interaction force between two colloidal particles located on the axis of a cylindrical cavity. The finite element approach for obtaining the interaction force for this geometry, however, seemed to have spurred a controversy following the numerical results shown by Bowen and Sharif (1998, 1999). In their study, it was reported that a long-range attraction would exist between the particles when these are confined in a cylindrical pore. This unusual result was almost immediately questioned by several authors, and it has been shown subsequently that the attractive force between two similarly charged colloidal particles in a cylindrical confinement is physically unrealistic in the framework of the PB equation [Gray *et al.*, 1999; Sader and Chan, 1999*b*; Sader and Chan, 2000; Bowen and Williams, 2002].

2.5 Influence of Confining Geometry: Roughness Effect

The DLVO model provides the pair interaction between two charged colloidal objects in an infinite electrolytic domain assuming that the interacting bodies are ideally shaped and perfectly smooth. Several applications, particularly those involving particles in a confined domain, likely violate the limitations imposed by such a pair-potential approach. In these cases, the pore walls will modify the net interaction force between the colloidal particles trapped inside the pore. Furthermore, in most natural processes, the confining pore geometry is extremely heterogeneous. Morphological heterogeneity, or roughness, is already considered a key factor in seriously altering the DLVO interaction energy and force between colloidal objects. It is believed that the effect of surface roughness is substantial on both the Lifshitz-van der Waals (LW) and the

electrostatic double layer (EDL) forces, the two components of the DLVO interaction force. For instance, surface roughness is typically considered as a possible cause for the large discrepancies observed between the theoretical predictions and experimental observations in particle deposition, hetero-coagulation, colloidal fouling of surfaces, and various other engineered and natural processes [Tamai *et al.*, 1983; Czarnecki, 1986; Czarnecki and Warszynski, 1987; Tobiason, 1989; Elimelech and Omelia, 1990; Shulepov and Frens, 1995; Shulepov and Frens, 1996; Walz, 1998].

During the last several decades, different approaches have been proposed for modelling surface roughness and subsequent evaluation of the colloidal interaction between rough surfaces. One of the most common approaches for modelling roughness involves random placement of geometrically regular asperities on a smooth surface. Herman and Papadopoulos (1990, 1991) developed equations to investigate the effect of roughness on both the van der Waals and the electrostatic double layer interaction of parallel flat plate systems with surface features. The van der Waals interaction was calculated using the Hamaker method, and Derjaguin's approximation (DA) was used for the electric double layer interaction. They considered spherical and conical asperities with protrusions and depressions on one of the surfaces to model the surface roughness. Significant variation of the van dar Waals force and the electrostatic double layer force was observed due the asperities. Sparnaay (1983) also derived the expression for the nonretarded van der Waals interaction between a flat plate and a cone. Elimelech and O'Melia (1990) investigated the effect of particle size on the interaction of polystyrene latex particles on spherical glass beads. They reported a higher rate of particle deposition than predictions made by the DLVO theory and attributed it to surface roughness. Shulepov *et al.* (1995, 1996) studied the effect of surface roughness and particle size on the rate of perikinetic coagulation. Their results showed that the influence of surface roughness is more pronounced compared to the particle size on the kinetics of slow Brownian coagulation. Suresh and Walz (1996, 1997) developed a set of analytical equations

to calculate the van der Waals and the electrostatic double layer energies between a rough spherical particle and a smooth plate in an infinite medium. Regular asperities were modelled using hemispheres of fixed radius on a smooth particle surface. They also verified their analytical result with experimental measurement done using the technique of total internal reflection microscopy (TIRM). They did not find any discrepancy of these experimental results with their analytical result though they used linear superposition technique for analytical calculation, which is valid only at higher separation between interacting particles. Lenhoff (1994) employed a slightly different approach to model a rough particle. He presented the potential distribution in and around a rippled sphere. Calculation of the LW component of the DLVO interaction using Hamaker's pairwise summation approach might be fairly accurate but the EDL component is arguably over estimated in these calculations since the interaction is usually evaluated using DA. Also these studies are based on regular geometric asperities. However, a geometrically regular shape is a poor model for roughness because it fails to capture the morphological randomness inherent in roughness.

Van Bree *et al.* (1974) studied the influence of irregular surface roughness on the van der Waals attraction between two parallel planes. One plane was considered flat while the other had small surface irregularities of zero average deviation. However, their calculation of the van der Waals attractions is valid only for the case when the radius of the sphere is much greater than the sphere-plate separation. Czarnecki and Dabros (1980) evaluated the retarded van der Waals interaction between a rough particle and a flat plate using Hamaker approach. They assumed that the rough particle has a solid core and rough shell that could be described with a radial distribution function. Later, Czarnecki (1986) calculated the van der Waals attraction energy between unequal rough spherical particles. Czarnecki and Itschenskij (1984) and Czarnecki and Warszynski (1987) also investigated the effects of surface in-homogeneities on the interactions governing colloid stability to explain the presence of tangential forces between a smooth particle and a rough planar surface. Roughness

was characterized as a number of small spheres with randomly selected radii dispersed on a planar surface. All of these models are mainly for the van der Waals attraction; the effect of roughness on the electrostatic interaction was not considered.

Recently, a model of surface roughness for DLVO interaction was proposed by Bhattacharjee *et al.* (1998) considering both protrusions and depressions by randomly selected asperity radii from a normal distribution. Both LW and EDL component of the DLVO interaction were evaluated by applying Surface Element Integration (SEI) technique [Bhattacharjee and Elimelech, 1997]. They concluded that presence of surface roughness causes a significant reduction in the repulsion energy compared to the DLVO prediction for smooth objects. SEI slightly improves the EDL calculations for rough surfaces. However, a complete and general solution of the electrostatic problem for rough surfaces is still elusive.

All of these roughness studies consider either particle-particle or particle-plate interaction in an infinite medium. None of the previous studies considered roughness effects in confined domains. The importance of considering roughness on confining walls of a capillary stems from our attempts to analyze the flow of particles inside microscopic microfluidic channels. Typical micro-fabrication practices, which involve etching the channels on a suitable substrate, rarely yield smooth walls. In many cases, the roughness of the walls is substantial, and adversely influences the manipulation of the particles by altering the electrical field distributions in the channel.

2.6 Summary

The review of literature shows that considerable information exists on the binary DLVO interaction between colloidal particles, although information regarding colloidal interactions in confined or many-body geometries is quite scarce. It might be pertinent to assume pairwise additivity of dispersion forces and calcu-

late the net LW interaction in such many-body systems by applying Hamaker's microscopic approach. Calculations of the net electrostatic double layer interaction in such confined geometries is considerably more difficult. In a confined system, the presence of charge on the confining walls alters the electrolyte distribution inside the domain, which in turn influences the net interaction between two colloidal particles in the confinement. Furthermore, if the walls of the confinement are rough, the electrolyte distribution is perturbed locally, which can cause further complications. The overall consequence is that the EDL interactions between colloidal particles in complex confined and many-body geometries cannot be determined by existing techniques.

Chapter 3

Electrostatic Interaction in Confined Domains

3.1 General

In the previous chapter, literature related to colloidal interactions has been reviewed. Most of the previous studies are mainly restricted to the particle-particles colloidal interaction in an infinite medium. Only few analytical attempts have been made to solve the non-linear Poisson-Boltzmann (NLPB) for confined geometries. Geometrical complexity and non-linear behaviour of the governing Poisson-Boltzmann (PB) equation are two main drawbacks to achieve the exact scenario of colloidal interaction in a confined domain using analytical techniques. Hence, numerical procedures for addressing these problems are gaining importance.

In this chapter, a mathematical model of particle-particle electrostatic double layer (EDL) interaction inside a cylindrical capillary based on the non-linear Poisson-Boltzmann equation is described along with details of the numerical scheme. The behaviour of the particle-particle interaction under different combinations of surface potential on the particles and capillary surface has been analyzed using the finite element technique.

3.2 Mathematical Modelling of Electrostatic Interaction

3.2.1 Governing Equation

Almost all substances acquire surface charge when brought in contact with an aqueous medium and the stability of such a system can be affected by the electric potential distribution near the charged surface. Ions of opposite charge (counter-ions) to that of the surface are attracted towards the surface, while similar charges (co-ions) are repelled by the charged surface. This type of ionic cloud near a charged surface is known as an electric double layer. The electric potential distribution within the diffuse double layer is given by the Poisson equation as

$$\varepsilon\varepsilon_0\nabla^2\psi = -\rho_f \tag{3.1}$$

Here ψ is the electric potential, ε is the dielectric constant of the suspending medium, ε_0 is the dielectric permittivity of vacuum, and ρ_f is the free charge density, which is given by

$$\rho_f = \sum_{i=1}^{N} n_i \nu_i e \tag{3.2}$$

where n_i represents the ionic number concentration of i^{th} species having valency ν_i, and e represents the magnitude of the electronic charge.

According to Boltzmann's probability law, the distribution of charged ions in the diffuse double layer is given by

$$n_i = n_{i\infty} \exp\left[-\frac{w_i}{kT}\right] \tag{3.3}$$

where w_i $(=\nu_i e\psi)$ represents the work done in bringing an ion i from the bulk solution to a point in the double layer where the potential is ψ, $n_{i\infty}$ is the bulk solution ionic number concentration at the neutral state where $\psi = 0$, k is the Boltzmnann constant, and T is the absolute temperature. In the above expression, energies involved in moving aside other ions or creating a passage in the solvent are ignored. Inserting Eqs. (3.2) and (3.3) into Eq. (3.1) leads

to well known Poisson-Boltzmann (PB) equation governing the distribution of the electric potential within the charged medium

$$\varepsilon\varepsilon_0\nabla^2\psi = -\sum_{i=1}^{N} n_{i\infty}\nu_i\, e \exp\left[-\frac{\nu_i e\psi}{kT}\right] \tag{3.4}$$

For a symmetric ($\nu_+ = -\nu_- = \nu$; $n_{i\infty} = n_\infty$) electrolyte, the non-linear Poisson-Boltzmann equation can be written as

$$\nabla^2\psi = \frac{2n_\infty\nu e}{\varepsilon\varepsilon_0}\sinh\left(\frac{\nu e\psi}{kT}\right) \tag{3.5}$$

It is should be noted that the above expression is valid within the electrolyte medium, *i.e.*, outside the charged bodies. However, inside the charged bodies that are perfect dielectrics, the right hand side of the Eq. (3.5) becomes zero.

In the present investigation, two solid charged particles are considered inside a cylindrical capillary. The capillary is infinitely long and is connected to two reservoirs of electrolyte. It is also assumed that the particles and the cylinder are perfect dielectrics ($\varepsilon = 1$) with no free charge in them, and hence, the PB equation is solved in the electrolyte medium only (the so-called outer problem). It is straightforward to solve the Poisson or Laplace equations inside the particles and the confining walls of the domain. Although such an approach will lead to a more rigorous analysis of the electrostatic problem, we resort to solving the "outer problem" to conform to earlier studies against which the results of the present model is compared for some limiting cases [Carnie *et al.*, 1994*b*; Stankovich and Carnie, 1996].

Depending on the charging behaviour of the surfaces immersed in the dielectric, the electrostatic interaction may be calculated assuming constant surface potential, constant surface charge, or surface charge regulation boundary conditions at the solid liquid interfaces [Carnie and Chan, 1993*a*; Carnie and Chan, 1993*b*; Carnie *et al.*, 1994*b*; Sader and Chan, 2000]. Usually, most charged interfaces in aqueous electrolyte media tend to obey some form of a charge regulatory behaviour. However, it is known that constant potential (CP) and

constant charge (CC) conditions represent the limiting charging behaviours of the interfaces, and provide a lower and an upper bound of the interaction, respectively. Accordingly, in the present investigation, both CP and CC cases are considered to obtain the lower and upper bounds of interaction between two charged particles. The constant potential boundary condition is represented as

$$\psi = \psi_s \text{ for } \partial\Omega \in \text{solid liquid interface} \tag{3.6}$$

where ψ_s is the surface potential of the solid-liquid interface, and $\partial\Omega$ represents the boundary of the computational domain. The constant charge boundary condition can be represented as

$$-\mathbf{n} \cdot \nabla\psi = \sigma_p \text{ for } \partial\Omega \in \text{ solid liquid interface} \tag{3.7}$$

where $\mathbf{n}$ is the unit normal to the solid liquid interface pointing to the electrolyte, and σ_p is the scaled surface charge density, related to the interfacial charge density q_p (C/m^2) as

$$\sigma_p = \frac{\nu e q_p}{\kappa\varepsilon\varepsilon_0 kT} \tag{3.8}$$

Thus, known values of the surface potential ψ_s or the surface charge density q_p provide the necessary boundary conditions at the solid liquid interfaces.

The above equations provide the generalized formulation of the electrostatic problem. Solution of the PB equation in a given geometrical framework requires recasting Eq. (3.5) in the proper coordinate system representing the geometry, and defining the boundary conditions at all the solid liquid interfaces. In the following, the governing equations leading toward the calculation of electrostatic double layer force on a particle in a system comprising two colloidal particles within a charged cylindrical capillary is described.

3.2.2 Computational Geometry and Boundary Conditions

Figure 3.1 shows the geometry under consideration in the present investigation along with the coordinate framework. Here, two spherical colloidal particles

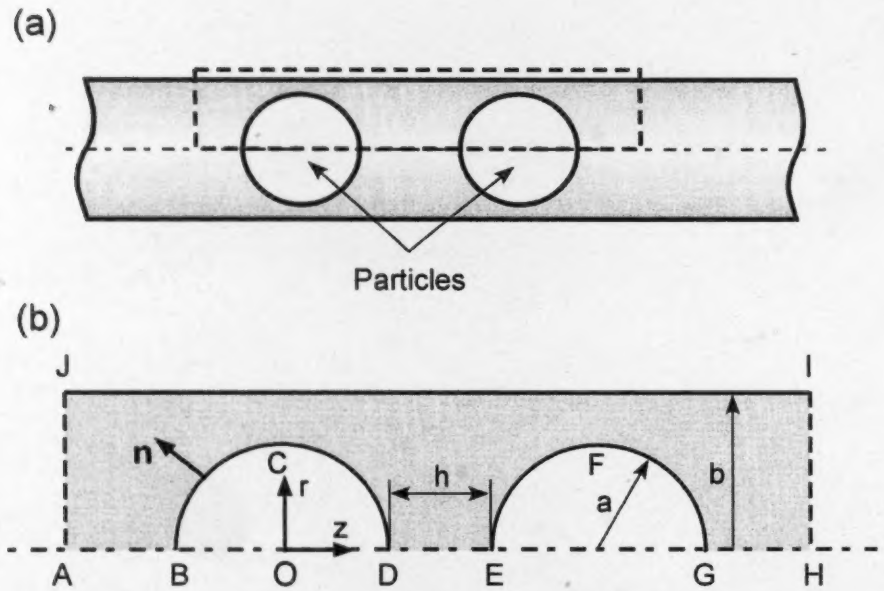

Figure 3.1: Schematic depiction of two spherical colloidal particles inside a cylindrical capillary (a). The particle centers are located on the cylinder axis. The region circumscribed by the broken lines depicts the computational domain, shown in detail in part (b). Utilizing the symmetry around the horizontal axis, the two-dimensional formulation of the governing equation was developed. The arcs BCD and EFG represent the particle surfaces, while the line IJ represents the wall of the cylindrical capillary. The origin of the cylindrical coordinate system is located at O.

of radius a are separated by a distance h (distance of closest approach) in an infinitely long straight cylindrical capillary of radius b. The particle surfaces are treated as either constant surface potential or constant surface charge density boundaries. The computational domain used in the finite element modelling is depicted by the rectangular region (in dashed lines) in Figure 3.1a. The particle centers lie on the axis of the cylindrical capillary, rendering the problem to be axisymmetric in a cylindrical coordinate system. Figure 3.1b shows the geometric details of the computational domain. The surfaces of the two particles (arcs BCD and EFG) are assigned constant surface potentials ψ_p or constant charge densities q_p in different simulations. The wall of the cylindrical capillary

(solid line IJ) is assigned a constant surface potential ψ_c and the remaining parts of the boundary have appropriate symmetry boundary conditions. The cylindrical coordinate system is chosen such that the center of the particle BCD is located at the origin O.

In the cylindrical coordinate system, the PB equation (Eq. (3.5)) is written as

$$\frac{\partial^2\psi}{\partial r^2} + \frac{1}{r}\frac{\partial\psi}{\partial r} + \frac{\partial^2\psi}{\partial z^2} = \frac{2n_\infty\nu e}{\varepsilon\varepsilon_0}\sinh\left(\frac{\nu e\psi}{kT}\right) \tag{3.9}$$

by noting that the potential is independent of the angular coordinate θ. As mentioned earlier, this equation is solved in the electrolyte solution only, shown by the shaded region in Figure 3.1b. The boundary conditions for constant surface potential on the particles and the cylinder are

$$\psi = \psi_p \text{ for } \partial\Omega \in \text{ BCD and EFG} \tag{3.10a}$$

$$\psi = \psi_c \text{ for } \partial\Omega \in \text{ IJ} \tag{3.10b}$$

$$\mathbf{n}\cdot\nabla\psi = 0 \text{ for } \partial\Omega \in \text{ AB, DE, GH, HI, and JA} \tag{3.10c}$$

The last statement, Eq. (3.10c), provides the symmetry conditions on the fluid boundaries, implying that the potential gradients normal to these line segments are zero. In this equation, $\mathbf{n}$ represents the unit normal to the surface. Clearly, this is an artificial boundary condition on the segments JA and HI, and appropriate measures must be taken in the numerical solution to ensure that this artificial boundary condition does not influence the accuracy of the solution.

For constant charge particles, the appropriate boundary condition is

$$-\mathbf{n}\cdot\nabla\psi = \sigma_p \text{ for } \partial\Omega \in \text{ BCD and EFG} \tag{3.11}$$

with the other boundary conditions, Eqs. (3.10b) and (3.10c), remaining same as the constant potential case.

The surface charge density of an isolated charged particle is related to the surface potential through [Russel *et al.*, 1991]

$$q_p = \frac{Q_p}{4\pi a^2} = \frac{\varepsilon\varepsilon_0 kT}{e\nu}\kappa\left[2\sinh\left(\frac{1}{2}\Psi_{p,\infty}\right) + \frac{4}{\kappa a}\tanh\left(\frac{1}{4}\Psi_{p,\infty}\right)\right] \tag{3.12}$$

where q_p is surface charge density (C/m^2), Q_p is the total surface charge, and $\Psi_{p,\infty}$ $\left(= \frac{\nu e \psi_{p,\infty}}{kT}\right)$ is the scaled surface potential of an isolated spherical particle. Introducing the scaled charge density, Eq. (3.8), we get

$$\sigma_p = 2\sinh\left(\frac{1}{2}\Psi_{p,\infty}\right) + \frac{4}{\kappa a}\tanh\left(\frac{1}{4}\Psi_{p,\infty}\right) \tag{3.13}$$

The above relationship is employed to define the charge density based on a given surface potential on the spherical particles in isolation. Equation (3.12), which is a semi-empirical relationship, is known to deviate from the correct charge densities obtained by numerically solving for the electric field distribution around an isolated sphere by $< 5\%$ for κa greater than or equal to 0.5 [Russel *et al.*, 1991].

3.2.3 Normalization of Governing Equations

For numerical calculation, the governing non-linear Poisson-Boltzmann (NLPB) equation (Eq. (3.9)) is rendered non-dimensional by scaling the electric potential with respect to thermal energy, yielding the following form

$$\nabla^2\Psi = \kappa^2\sinh(\Psi) \tag{3.14}$$

Here Ψ $\left(= \frac{\nu e \psi}{kT}\right)$ is the scaled potential, and the parameter κ is the inverse Debye screening length (some representative values are listed in Table 3.1), defined as

$$\kappa = \sqrt{\frac{2n_\infty \nu^2 e^2}{\varepsilon\varepsilon_0 kT}} \tag{3.15}$$

To render the problem independent of the actual physical dimensions of the particles and the cylinder, Eq. (3.14) is further modified by introducing the scaled parameters $\bar{r} = \kappa r$ and $\bar{z} = \kappa z$, and finally, rewriting in axisymmetric cylindrical coordinates as

$$\frac{\partial^2\Psi}{\partial\bar{r}^2} + \frac{\partial^2\Psi}{\partial\bar{z}^2} = \sinh(\Psi) - \frac{1}{\bar{r}}\frac{\partial\Psi}{\partial\bar{r}} \tag{3.16}$$

Molarity	$\nu_+ : \nu_-$	κ^{-1} (m)
10^{-3}	1:1	1.089×10^{-8}
	2:2	5.447×10^{-9}
	3:3	3.631×10^{-9}
10^{-2}	1:1	3.445×10^{-9}
	2:2	1.722×10^{-9}
	3:3	1.148×10^{-9}
10^{-1}	1:1	1.089×10^{-9}
	2:2	5.445×10^{-10}
	3:3	3.631×10^{-10}

Table 3.1: Values of Debye screening length (κ^{-1}) for several electrolyte concentrations and valences at 300K for $\varepsilon = 10^2$, $\varepsilon_0 = 8.85 \times 10^{-12}$ C/Vm, $e = 1.602 \times 10^{-19}$ C, $k = 1.381 \times 10^{-23}$ J/K.

which represents a general partial differential equation (PDE) formulation of the type

$$\nabla \cdot \Gamma = \mathbf{R} \tag{3.17}$$

where $\Gamma = \Psi_{\bar{r}} + \Psi_{\bar{z}}$, with the subscripts representing the partial derivatives with respect to $\bar{r}$ and $\bar{z}$, and

$$\mathbf{R} = \sinh(\Psi) - \frac{1}{\bar{r}} \frac{\partial \Psi}{\partial \bar{r}} \tag{3.18}$$

3.2.4 Calculation of Interaction Force

Once the potential distribution is obtained by solving the PB equation, the electrostatic force on any one of the spherical particles can be calculated by integrating the total stress tensor, defined as

$$\mathbf{T}_{ij} = \left(\Pi - \frac{1}{2} \varepsilon \varepsilon_0 \mathbf{E} \cdot \mathbf{E} \right) \mathbf{I} + \varepsilon \varepsilon_0 \mathbf{E}\mathbf{E} \tag{3.19}$$

over the surface of a particle, yielding

$$\mathbf{F} = \iint_p \mathbf{T}_{ij} \cdot \mathbf{n}\, dS = \iint_p \left[\left(\Pi - \frac{1}{2}\varepsilon\varepsilon_0 \mathbf{E} \cdot \mathbf{E} \right) \mathbf{I} + \varepsilon\varepsilon_0 \mathbf{E}\mathbf{E} \right] \cdot \mathbf{n}\, dS \qquad (3.20)$$

where the subscript p represents integration over the closed particle surface. Here, $\mathbf{F}$ is the force acting on the sphere, $\mathbf{E}$ $(=-\nabla\psi)$ is the electrostatic field vector, Π is the osmotic stress, $\mathbf{n}$ is the unit surface normal (Figure 3.1b), and $\mathbf{I}$ is the identity tensor. It should be noted that the above expression of force is independent of the choice of the surface over which the integration is performed. It can be performed on the closed surface of any of the particles, or at the mid-plane of these particles. In the present investigation, the net stress tensor is integrated over the surface of a particle to calculate the net force on the particle.

The net force acting on a sphere along the axial (z) direction can determined from the total force $\mathbf{F}$ and can be written explicitly (see Appendix A) as

$$\begin{aligned} F_z &= \mathbf{F} \cdot \mathbf{k} \\ &= 2\pi\kappa^2\varepsilon\varepsilon_0 \left(\frac{kT}{\nu e} \right)^2 \int_{\mathrm{BCD}} \left[n_r \Psi_r \Psi_z + n_z \left\{ (\cosh \Psi - 1) + \frac{1}{2} \left(\Psi_z^2 - \Psi_r^2 \right) \right\} \right] r dr \end{aligned} \qquad (3.21)$$

where $\mathbf{k}$ is the unit normal in the positive z direction, n_r and n_z are the components of the unit normal along the r and z directions, respectively, and BCD represents the semi-circular boundary of the spherical particle over which the integration is performed. Ψ_r and Ψ_z are the components of the electric field vector $\mathbf{E}$ along the r and z directions, respectively. The term $(\cosh \Psi - 1)$ in Eq. (3.21) represents the osmotic pressure contribution to the net force, while the two remaining terms in the square braces represent the electrostatic (Maxwell) stress. Since the integral of the osmotic pressure term vanishes over a closed domain having a constant potential, the force for CP situations is calculated by excluding the osmotic pressure term from Eq. (3.21). For CC cases, both the osmotic and electrostatic stresses are included in the force expression. Finally,

the axial force is represented in its non-dimensional form, given by

$$f_z = \frac{F_z}{\varepsilon\varepsilon_0}\left(\frac{\nu e}{kT}\right)^2 \tag{3.22}$$

3.3 Numerical Solution Procedure

The numerical solution of the PB equation was performed using finite element analysis. An inherent advantage of using the finite element technique for obtaining the interaction force between two particles in a cylindrical cavity is its ability to consider arbitrary geometrical domains. Furthermore, one can avoid coordinate transformations, and directly apply the technique in a coordinate system that facilitates representation of the physical domain. The only problem with adoption of finite element techniques is perhaps the computational load it involves, specifically when stringent accuracy of the numerical results is warranted. However, several commercial finite element solvers of a general nature have become available recently, and have substantially simplified the implementation of this technique to solve a variety of problems quite accurately. In this context, it is felt that if the accuracy and relevance of this technique can be demonstrated in solving the widely discussed problem of obtaining the interaction force between two particles in a charged cylindrical capillary, there might be greater interest in exploring finite element based solutions of the PB equation for several geometries of practical concern. One of the main goal of the present investigation was to employ a generalized technique that is widely available and can be implemented relatively easily on most commercial finite element software. Details regarding implementation of finite element approximation to solve partial differential equations are available in standard textbooks [Zienkiewicz and Taylor, 1989]. Consequently, in this section, only details of the procedure followed to formulate the problem, the types of elements used, and the methodology of adaptive mesh refinement and error control are discussed. The formulation of the problem, specifically the statement of the problem in a generalized PDE form and subsequent recasting in the weak form were crucial for

successful and fast solution. Furthermore, the adaptive mesh refinement steps and refinement criteria stated here provided a fast and accurate convergence of the numerical solution.

3.3.1 The Finite Element Model

The finite element method approximates the exact solution Ψ as a combination of piece-wise polynomial shape functions. For convenience, a quadratic shape function φ_i with U_i degrees of freedom is used, where $\varphi_i = 1$ at node i, and $= 0$ at all other nodes. In terms of the basis functions and degrees of freedoms, the solution can be written for an element as

$$\Psi = \sum_i U_i \varphi_i \tag{3.23}$$

where the summation is over all the nodes in the element.

Clearly, the strong form of the governing PDE, as written in Eq. (3.17), needs to be converted to its weak form to implement a finite element solution, which is obtained by writing Eq. (3.17) as an equality of the integrals

$$\int_\Omega v \nabla \cdot \Gamma \, \mathrm{d}A = \int_\Omega v \mathbf{R} \, \mathrm{d}A \tag{3.24}$$

where v is a test function. Applying Green's theorem, the area integral in the left hand side of the above equation can be written as a line integral over the domain boundary. Furthermore, applying a Neumann boundary condition,

$$-\mathbf{n} \cdot \Gamma = \mathbf{G} \text{ on } \partial\Omega \tag{3.25}$$

the weak formulation of the governing PDE is given as

$$\int_\Omega v \nabla \cdot \Gamma + v\mathbf{R} \, \mathrm{d}A + \int_{\partial\Omega} v\mathbf{G} \, \mathrm{d}s = 0 \tag{3.26}$$

Here the function $\mathbf{G}$ defines the generalized Neumann boundary coefficient. The term $\mathrm{d}s$ in the final integral represents a small length element on the domain

boundary $\partial\Omega$. The weak problem can be further constrained through a Dirichlet boundary condition, stated as

$$\mathbf{Q} = 0 \text{ on } \partial\Omega \tag{3.27}$$

where $\mathbf{Q}$ represents a vector of Dirichlet boundary conditions.

Equations (3.26) and (3.27) constitute the weak form of the governing PDE that can be solved using the finite element technique.

3.3.2 Mesh Generation

The computational domain was initially discretized into a triangular mesh and Lagrangian elements of second order (quadratic elements) were used. It should also be noted that the numerical convergence becomes faster when quadratic elements are used in lieu of linear elements. However, elements of order greater than two may increase the computational load or cause instabilities in the solution. The use of quadratic elements implies that a triangular element has six nodes on its boundary (three at the vertices, and three at the midpoints of each side). Each of these nodes has a shape function φ_i with U_i degrees of freedom. The weak form of the governing PDE was first discretized by assuming the test function v to be the shape function φ_i in each element. A non-uniform initial mesh was generated in each simulation using triangulation of the domain. The mesh was created to ensure that the domain error was small at the curved surfaces of the sphere, yielding smaller elements near the circular boundaries in Figure 3.1b.

3.3.3 Error Criteria and Adaptive Mesh Refinement

Initial solution of the assembled matrix equation was achieved by Gauss elimination. After solution, the local error in each element was calculated by computing an L^2 norm of the error. This error was then used to refine the mesh using adaptive mesh refinement scheme. This technique typically employs the difference

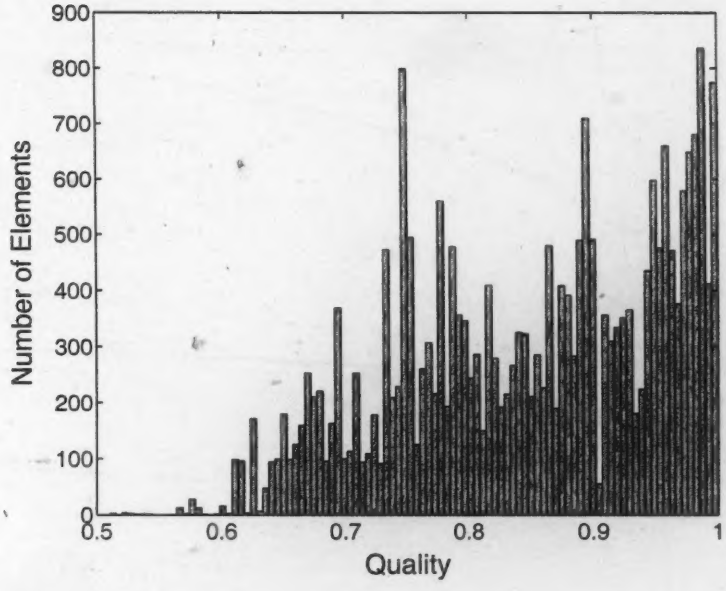

Figure 3.2: Histogram showing the distribution of the mesh qualities for 24511 elements in the mesh.

between the numerical solution and true solution, and determines the regions of the computational domain where the error is above a certain tolerance. The mesh is then refined in the region of highest error. The refinement method can be of two types. Regular refinement results in a uniform mesh, where all of the specified triangles are divided into four triangles of the same shape. The second type of refinement method reduces the longest edge on each triangle. Some triangles outside of the specified set may also be refined, in order to preserve the triangulation and mesh quality. Here regular refinement is used to maintain the mesh quality high. Quality of the mesh used in this investigation is shown in Figure 3.2. It is a number between 0 and 1 calculated from the following expression

$$Quality = \frac{4\sqrt{3A}}{\sqrt{{l_1}^2 + {l_2}^2 + {l_3}^2}} \tag{3.28}$$

where A is the area of the triangle and l_1, l_2, and l_3 are the side lengths of the triangle. Generally, $Quality > 0.6$ of a triangle in the finite element mesh is

	Uniform mesh		Adaptive mesh	
Step number	No. of elements	Force	No. of elements	Force
1	212	23.085	212	23.085
2	848	25.662	505	25.178
3	3392	26.581	1153	26.286
4	13568	26.864	2506	26.682
5	54272	26.963	5496	26.903
6	–	–	11421	26.910
7	–	–	24511	26.941

Table 3.2: Comparison between the interaction force obtained from adaptive mesh refinement and typical uniform mesh refinement techniques.

acceptable and $Quality = 1$ when $l_1 = l_2 = l_3$. In this study, the quality of the mesh is maintained over 0.5 in all simulations.

In this investigation, the adaptive mesh refinement was performed on all the elements where the error estimate was larger than the preset tolerance (10^{-6}). For equal number of elements, adaptive mesh gives more accurate results compared to a uniform mesh. In Table 3.2, a comparison between adaptive mesh and uniform mesh results is shown for two spherical particles inside a cylindrical capillary at a fixed separation distance $\kappa h = 0.4$ for $\kappa a = 1.0$ and $\Psi_p = -3.0$, assuming CP boundary conditions on the particles. Clearly, adaptive mesh converges faster than uniform mesh. The main steps involved in the adaptive mesh refinement technique are as follows:

- Generate a starting mesh and solve problem on the initial mesh.
- Based on the initial solution, estimate the error using L^2-norm.
- If the estimated error is less than the predefined tolerance then solution is assumed to have converged.
- If the estimated error is greater, then the mesh elements are refined and the problem is solved again using the refined mesh.

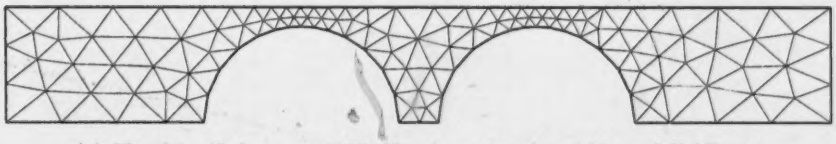

(a) Number of elements: 195, Number of nodes: 135, and DOF 464.

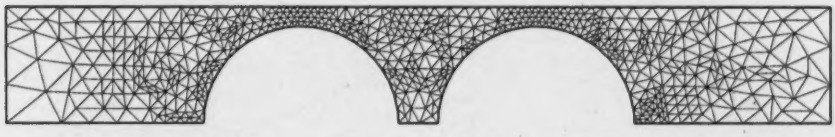

(b) Number of elements: 1130, Number of nodes: 645, and DOF 2419.

(c) Number of elements: 2516, Number of nodes: 1377, and DOF 5269.

(d) Number of elements: 5339, Number of nodes: 2843, and DOF 11024.

Figure 3.3: Adaptive mesh for two particles inside a cylindrical capillary.

In this study, adaptive mesh refinement was achieved by dividing each original element into four elements. When an element is refined, new nodes appear at the middle of each side , and if the neighboring triangle is not refined in a similar way, it is said to have hanging nodes. The refinement technique ensured that all hanging nodes were removed from the mesh by splitting neighboring triangles. It was also ensured that none of the refined elements had vertices smaller than half the vertices of the original elements. To illustrate the mesh refinement process, typical adaptive meshes are shown in Figure 3.3 for a case of two spherical particles inside a cylindrical capillary with $\kappa a = 2.0$. The first part in Figure 3.3 represents the initial mesh, and the three subsequent figures represent the mesh used in the 3rd, 4th, and 5th steps of the adaptive refinement, respectively. The results of different steps of the adaptive mesh refinement technique are listed in Table 3.3 for the case of two spherical particles inside an uncharged cylindrical capillary ($\Psi_c = 0.0$) and a charged cylindrical capillary ($\Psi_c = -3.0$).

	$\Psi_c = 0.0$		$\Psi_c = -3.0$	
Step number	Global error	Force	Global error	Force
1	0.6393750	23.085	0.9004110	3.7686
2	0.1695960	25.178	0.1545200	4.3403
3	0.0575730	26.286	0.0415070	4.3958
4	0.0170407	26.682	0.0125884	4.5582
5	0.0058698	26.903	0.0039266	4.5946
6	0.0018951	26.910	0.0012712	4.5983
7	0.0006302	26.941	0.0003968	4.6088

Table 3.3: Steps of the adaptive process.

3.3.4 Solution Methodology

The entire solution methodology was developed using a commercially available software FEMLAB (COMSOL, Inc., USA), which can be run either as a programmable toolbox for development of finite element solutions on MATLAB (The MathWorks, Inc., USA), or as a simple graphical user interface (GUI) based integrated environment for solution of partial differential equations using the finite element technique. It was observed that considerable programming flexibility could be achieved by using a sequence of function or procedural calls to various subroutines from the FEMLAB toolbox for implementing the various steps of the finite element procedure, while relegating all the peripheral calculations to MATLAB (see Appendix B for computer code). All the calculations were performed on a Pentium III (1000 MHz) personal computer.

The process of obtaining a solution, determination of the local error in each element, and mesh refinement was repeated until a global convergence criterion was attained. Limits on the maximum number of iterations in mesh refinement (10) and the maximum number of elements (30,000) are also imposed. The program was terminated when any of the above mentioned criteria was attained. After termination, the postprocessing of the data involved calculation of the interaction force on the boundaries of the spherical particles. A four point Gaussian quadrature was used to compute the force. The forces were computed on both the particle surfaces and their values were compared against each other. In all the reported results, the forces obtained on the two particle surfaces match to within two significant digits. As mentioned in Section 3.2.2, the boundary conditions on segments JA and HI (Figure 3.1b) are artificial symmetry conditions, which may be valid only when these boundaries are located sufficiently far away from the particles. To ascertain the minimum distance between the particle surface and the domain boundary (length of the segments AB and GH) that would lead to negligible error in the computed forces, the simulations were performed by setting this distance (AB or GH) to different values ranging from κa to $10\kappa a$. The resulting force computations indicated that the influence of

this artificial boundary becomes negligible when the lengths of the segments AB and GH are set to values $\geq 2\kappa a$.

3.4 Validation of Numerical Results

3.4.1 Particle-Particle Interaction

In this section, we first focus on the accuracy of the finite element calculations. This can be achieved by comparing the presently obtained force estimates with those available in other reported works. However, available studies in the literature mainly deal with the problem of particle-particle interaction in infinite media. To compare the finite element results, one of the limiting cases of the model, namely, interaction between two identical spherical particles in an infinite electrolyte medium is considered. The simulation results presented here are obtained for both the constant potential (CP) and the constant charge (CC) conditions on the particle surfaces. These numerical solutions were obtained by assuming the capillary radius b to be considerably larger than the particle radius a. A value of 0.2 for the parameter $\lambda = a/b$ (size ratio) was used to ensure that the influence of the cylindrical domain on the particle-particle interaction would be minimal. Furthermore, a Neumann boundary condition was applied on the capillary wall (IJ in Figure 3.1b)

$$\mathbf{n} \cdot \nabla \Psi = 0 \text{ on IJ} \tag{3.29}$$

Using these conditions, the interaction force between the two particles was computed without modifying the problem geometry or the coordinate system. The objective of employing this approach was to observe the influence of the cylindrical coordinate system on the error in force calculations. The cylindrical coordinate system has rarely been used for studying the interaction force between two spherical colloids. Typically, numerical solution of this problem is achieved by using a bispherical coordinate system, which maps the spherical physical domain to a rectangular computational domain [Carnie *et*

al., 1994*b*; Warszynski and Adamczyk, 1997]. Furthermore, the use of bispherical coordinate maps the infinite domain problem onto a finite grid, allowing one to use the more accurate boundary condition $\Psi = 0$ at ∞. It has generally been speculated that solution of the PB equation in other types of coordinate frameworks might lead to erroneous estimates of the interaction force for the two-sphere problem discussed here.

3.4.2 Hermite Collocation based Numerical Solution

An independent mathematical model is used to calculate the force between two identical charged particles in an infinite electrolyte medium [Carnie *et al.*, 1994*b*; Stankovich and Carnie, 1996]. Here, the cylindrical computation domain is first transformed into bispherical coordinates to map the region outside the particles into a rectangular domain. The solution in the bispherical coordinate system is then obtained using a cubic Hermite collocation based discretization scheme, followed by iterative solution of the resulting non-linear system of equations by a Newton-Raphson technique. The interaction between the particles is estimated

	scale	typical value
length	$\sqrt{\frac{\varepsilon\varepsilon_0 kT}{2n_\infty \nu^2 e^2}}$	10.894×10^{-9} m
potential	$\frac{kT}{\nu e}$	2.586×10^{-2} V
surface charge density	$\varepsilon\varepsilon_0\kappa^{-1}\left(\frac{kT}{\nu e}\right)$	2.101×10^{-3} C/m^2
force	$\varepsilon\varepsilon_0\left(\frac{kT}{\nu e}\right)^2$	5.918×10^{-13} N

Table 3.4: Typical values of different governing parameters for 1 mM 1:1 electrolyte for the parameter used in Table 3.1.

over a relatively wide range of scaled surface-to-surface separation distances $0 < \kappa h < 4.0$ for both CP and CC conditions on the particle surfaces. The charge density used in the CC calculations is obtained by numerically solving the PB equation around an isolated particle based on a scaled surface potential $\Psi_{p,\infty} = -3.0$. Finally, the dimensionless force between the two particles is evaluated by integrating the stress tensor over a surface separating the two particles. Typical values of different governing parameters are listed in Table 3.4 with the scales used to produce dimensionless quantities.

3.4.3 Comparison with Finite Element Results

In this subsection, results are shown for one of the limiting cases of the model, namely, interaction between two identical spherical particles in an infinite domain. The simulation results presented here are obtained for both the constant potential (CP) and constant charge (CC) conditions on the particle surfaces. Figure 3.4 depicts a comparison of the interaction forces obtained in the present study with the corresponding numerical estimates obtained using the Hermite collocation technique [Carnie *et al.*, 1994*b*; Stankovich and Carnie, 1996]. The interaction forces obtained under CP conditions using the two techniques are virtually identical over a relatively wide range of scaled separation distances (surface to surface) $0.0 < \kappa h < 4.0$ (Figure 3.4a). The finite element solution becomes unreliable at larger separations. Even over the range of separation distances shown in Figure 3.4, we observe that the interaction force obtained using the finite element calculations deviates slightly from the solid lines for $\kappa h > 3.0$. This is due to the relatively weak tolerances set for the convergence criteria of the numerical solution. Although higher accuracy can be achieved at greater separations by further mesh refinement, this was deemed as an enormous computational effort to obtain a relatively insignificant electrostatic force. The numerical results (scaled forces) at small separations ($\kappa h < 2.0$) from the two techniques were in conformity within 3% for both values of κa.

The results obtained in our study for the CC case are also in good agreement

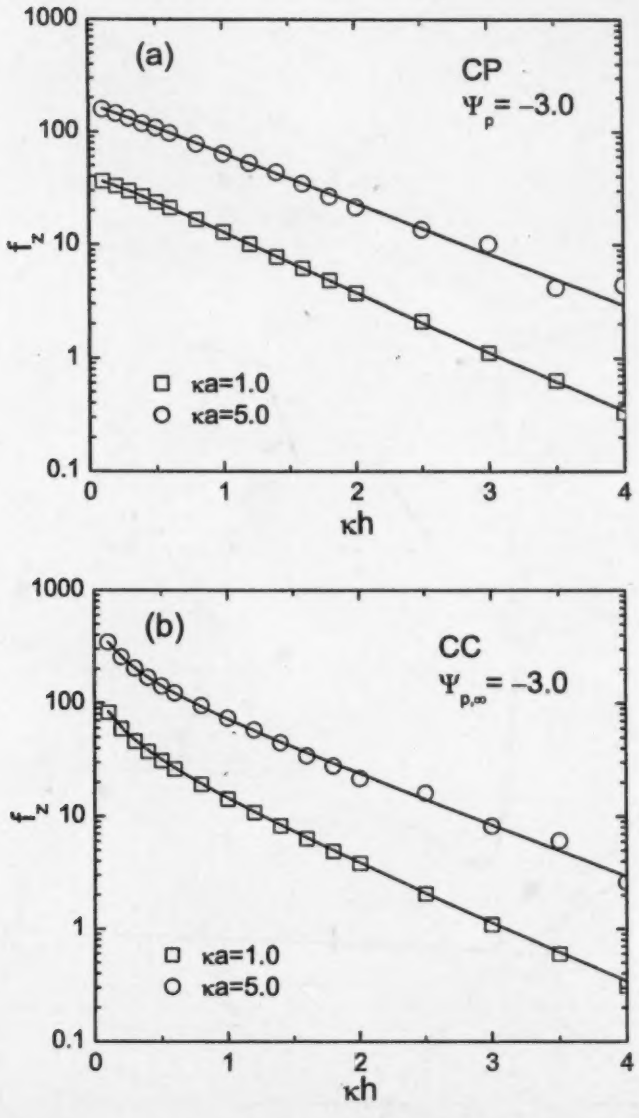

Figure 3.4: Variation of the electrostatic interaction force between two identical charged particles in an unbounded electrolyte with scaled separation distance, κh, corresponding to two values of scaled particle size, κa, for (a) constant potential (CP), and (b) constant charge (CC) conditions. Solid lines represent the results from an independent numerical result based on a Hermite collocation technique in a bispherical coordinate system (see text). Symbols represent the finite element results obtained in the present work.

with the results of the collocation solution (Figure 3.4b). In this case, the errors in the results based on finite element analysis tend to increase more rapidly with increasing separation distance between the particles. However, even for the CC case, the finite element results are within 5% of the corresponding collocation results (solid lines) for $\kappa h < 2.0$. In general, for a given number of elements and accuracy settings, the forces estimated under CP condition tend to be more accurate than the CC results.

The comparison of the presently obtained finite element estimates of the force with an independent numerical result based on a completely different technique highlights several points worth noting about the nature of finite element solutions of the non-linear PB equation. Three key differences in the two solution techniques can be readily identified, namely: (i) The present results were obtained in a cylindrical coordinate system whereas the collocation technique used a bispherical coordinate system. (ii) The boundary condition representing the cylindrical wall was chosen to be of Neumann type, which may be construed as an artificial boundary condition to the PB equation, while the boundary condition used in the bispherical coordinate system is the true condition at infinite separation. (iii) The integral for force calculation was evaluated on the particle surface in the finite element calculation, while the integral was performed over the mid-plane between the spherical particles in the collocation method noting that the integration over the particle surface results in relatively larger errors. Despite these differences, the two techniques provide almost identical results at small interparticle separations.

Although the comparison of the two results indicate the ability of finite element approximations to provide a reasonable estimate of the interaction forces, particularly at small values of particle-particle separations, it comes at the expense of fairly involved computation. It should be noted that the results in Figure 3.4 could not be attained without (a) using adaptive meshing, (b) using a large number of elements (usually of the order of 30,000), and (c) carefully choosing the convergence criterion. Furthermore, the governing equation had

to be stated in a very specific manner to achieve the given accuracy. These might be an artifact of our usage of a general-purpose commercial software for the computation, which may not be specialized for solution of the PB equation. Almost all of the standard features are used enabling high accuracy solutions, like adaptive solvers, multiple criteria for error minimization, and mesh adaptation. Yet, with none of the available combinations a convergence of the force to within a given tolerance could be obtained by using fewer elements. It should, however, be noted that in terms of accuracy, the finite element solutions for this limiting case are the worst compared to any of our subsequent calculations. This is due to the following reasons: (a) the computational domain used in these calculations was the largest to ensure that the artificial boundary effects were negligible on the solution; (b) most of the boundary conditions used (except for the ones on the particle surfaces) were artificial; and, (c) in the CC results, there may be an error ($\leq 5\%$) in the estimates of the surface charge density calculated using Eq. (3.12) compared to the values obtained using the numerical solution of the non-linear PB equation around a single particle.

Clearly, the solution of the PB equation for two spherical particles could have been more facile if the coordinate system of the problem was bispherical, rendering the computational grid to be rectangular. However, this option was ruled out because the primary objective of this study was to obtain the interaction force between the two spherical particles in a confined cylindrical domain, for which the present coordinate system seems natural, and allows us to reduce the dimensionality of the problem by utilizing axisymmetry.

3.5 Interaction Force for Particle in a Cylindrical Capillary

3.5.1 Potential Distribution and Fields

Some representative potential distributions in the confined electrolyte corresponding to capillary surface potentials $\Psi_c = 0.0$ and -3.0 are depicted in

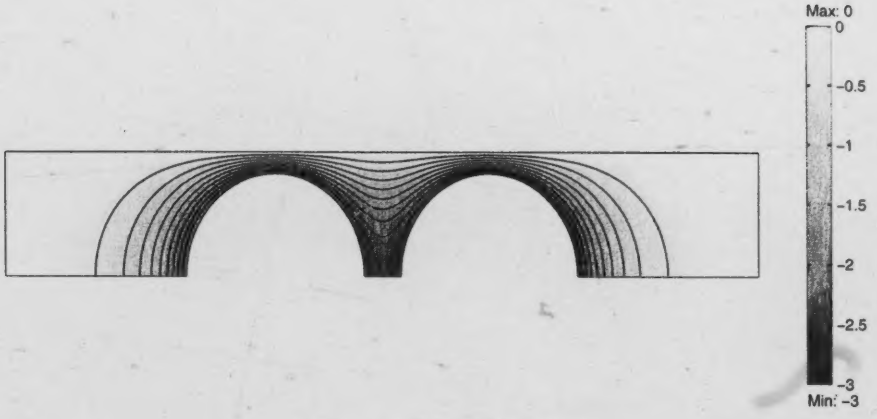

(a) $\Psi_p = -3.0$ and $\Psi_c = 0.0$.

(b) $\Psi_p = -3.0$ and $\Psi_c = -3.0$.

Figure 3.5: Potential distribution of two spherical constant potential (CP) particles inside an infinitely long cylindrical capillary corresponding to two values cylinder surface potential as shown in the legend.

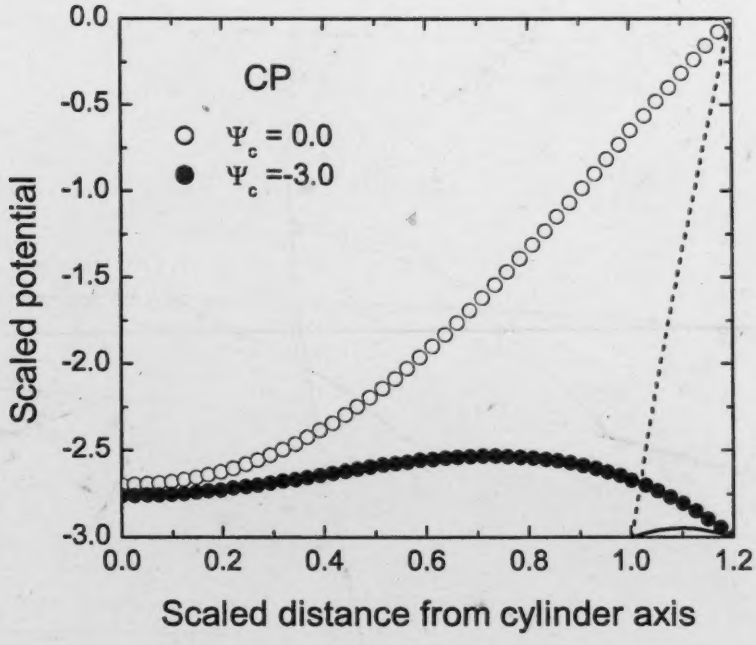

Figure 3.6: Variation of scaled potential inside the cylindrical capillary for constant potential (CP) particles at two different locations. Symbols represent the potential along the midplane between particles, and lines represent the variation along the distance of closest approach between the particle surface and the capillary wall at C (see Figure 3.1).

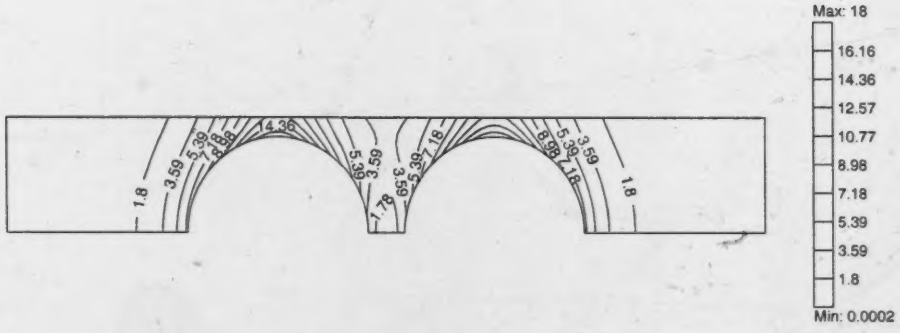

(a) $\Psi_p = -3.0$ and $\Psi_c = 0.0$.

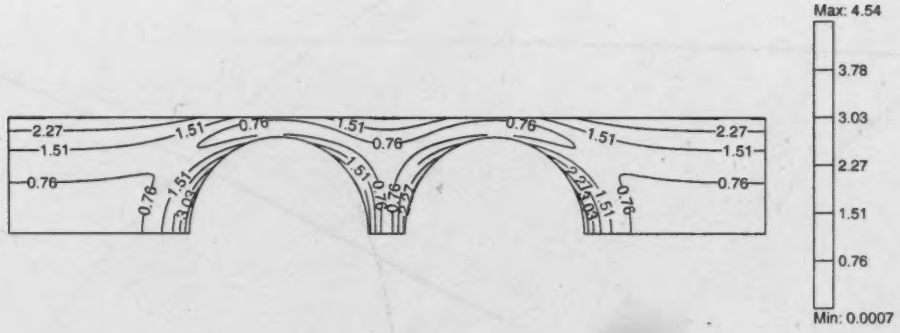

(b) $\Psi_p = -3.0$ and $\Psi_c = -3.0$.

Figure 3.7: Distribution of the electrostatic field strength in the confined domain for two spherical constant potential (CP) particles corresponding to two values cylinder surface potential as shown in the legend.

Figure 3.5 for CP conditions. In both cases, the surface potentials on the particles are fixed at $\Psi_p = -3.0$. The potential distribution in the domain (Figure 3.5) varies markedly corresponding to states of two different surface potentials on the capillary surface. This modification of potential distribution is shown quantitatively in Figure 3.6. Open symbols and dashed line represent the potential variation for $\Psi_c = 0.0$ and filled symbols and solid line represent the potential variation for $\Psi_c = -3.0$ at two different locations. For a zero surface potential on the capillary wall (Figure 3.5a), the potential decreases rapidly from the particle surfaces (dashed line in Figure 3.6), while the electrostatic potential distribution varies more modestly when the capillary surface potential is -3.0 (Figure 3.5b and solid line in Figure 3.6). This alteration in the potential distribution changes the electrostatic field quite remarkably, as shown in two plots in Figure 3.7 corresponding to cylinder surface potentials $\Psi_c = 0.0$ and -3.0, respectively. Noting that the electrostatic field is obtained from the spatial gradient of the potential ($\mathbf{E} = -\nabla\Psi$), it can be immediately recognized that the electrostatic field distribution in the $\Psi_c = -3.0$ configuration is quite modest, and the Maxwell stresses will be significantly lower on the particles in the $\Psi_c = -3.0$ configuration. The magnitudes of the electrostatic fields shown in the contour labels clearly suggest an order of magnitude suppression in the field strength around the individual particles when the capillary wall acquires the same surface potential as the particles.

Distribution of the electrostatic potential corresponding to CC conditions on the particle surfaces are shown in Figure 3.8 for two different cylinder potentials $\Psi_c = 0.0$ and -3.0. These results were obtained under identical parameter settings as the CP simulations. The cylinder wall was assumed to behave as a CP surface in these calculations. In both parts of Figure 3.8, the potential on the surfaces of the particles attain higher values than in Figure 3.5. Furthermore, the potential on the particle surfaces are not constant. At the mid point between the two particles, the potential is higher than the corresponding position of CP case (symbols in Figure 3.9). The distribution of potential for the CC case does

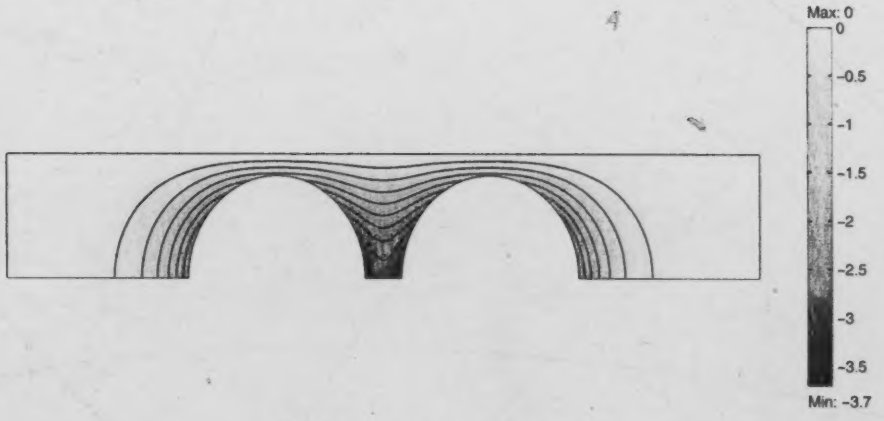

(a) $\Psi_{p,\infty} = -3.0$ and $\Psi_c = 0.0$.

(b) $\Psi_{p,\infty} = -3.0$ and $\Psi_c = -3.0$.

Figure 3.8: Potential distribution of two spherical constant charge (CC) particles inside an infinitely long cylindrical capillary corresponding to two values cylinder surface potential as shown in the legend.

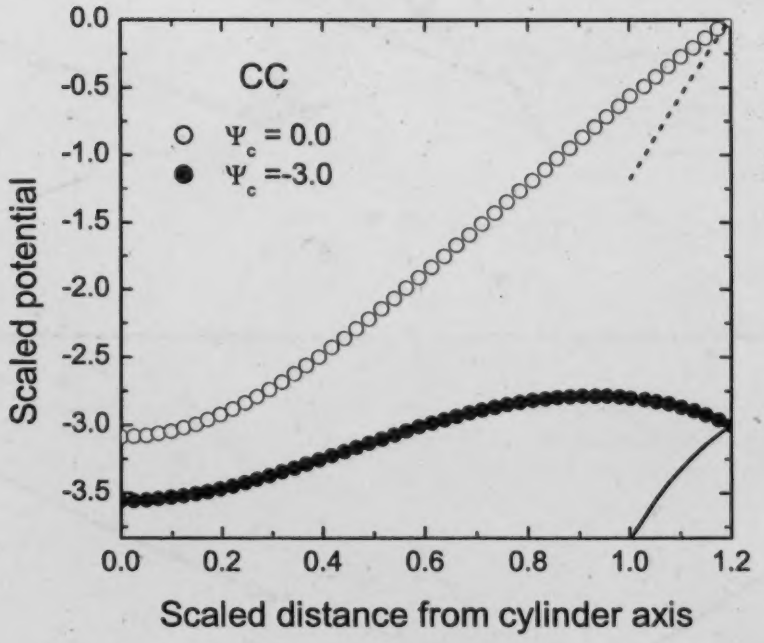

Figure 3.9: Variation of scaled potential inside the cylindrical capillary for constant charge (CC) particles at two different locations. Symbols represent the potential along the midplane between particles, and lines represent the variation along the distance of closest approach between the particle surface and the capillary wall at C (see Figure 3.1).

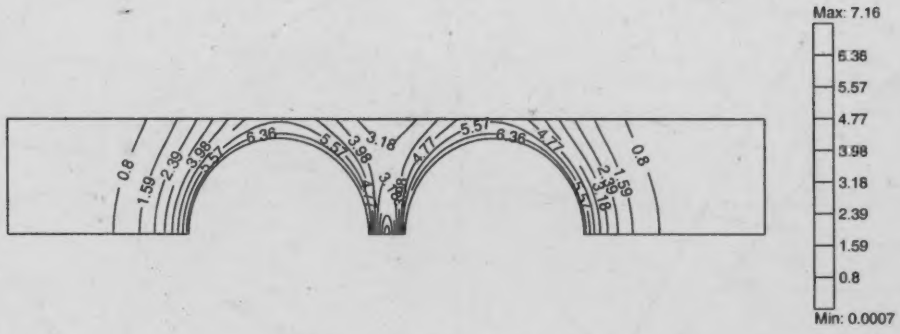

(a) $\Psi_{p,\infty} = -3.0$ and $\Psi_c = 0.0$.

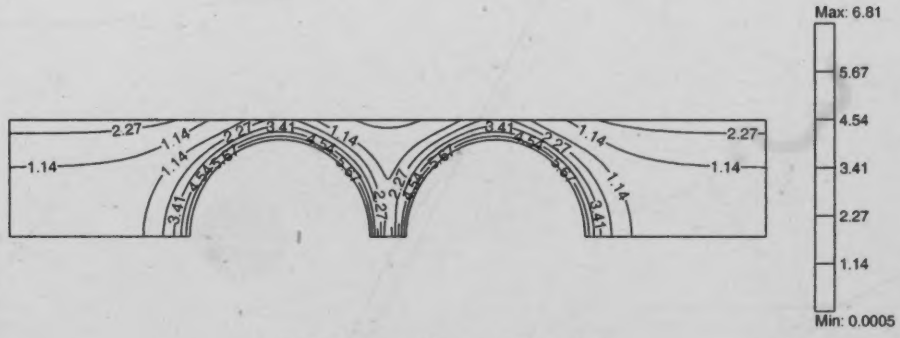

(b) $\Psi_{p,\infty} = -3.0$ and $\Psi_c = -3.0$.

Figure 3.10: Distribution of the electrostatic field strength in the confined domain for two spherical constant charge (CC) particles corresponding to two values cylinder surface potential as shown in the legend.

not change as uniformly as the corresponding potential for the CP case when the cylinder surface potential is $\Psi_c = 0.0$. At the closest surface on the particle from the capillary wall, different potential profiles (lines in Figure 3.9) are obtained for $\Psi_c = 0.0$ and $\Psi_c = -3.0$. We also note that the surface potential on the particle changes in these cases. The field distributions corresponding to CC cases for $\Psi_c = 0.0$ and -3.0, respectively, are shown in two parts of Figure 3.10. The distribution of electrostatic field is quite modest for CC cases compared to corresponding CP cases. No significant variation in the field distribution in terms of magnitude was observed.

3.5.2 The Interaction Force: Like-Charge Interaction

In this section, the interaction force between two particles in a cylindrical capillary is obtained for various combinations of the governing parameters to highlight the dependence of this force on the proximity of the charged capillary wall. The interaction forces between two spherical particles located on the axis of a charged cylindrical capillary were obtained for constant potential (CP) and constant charge (CC) boundary conditions on the particles. The force was determined for wide ranges of the scaled particle size κa, size ratio λ $(= a/b)$, and different combinations of the surface potentials on the particles and the cylinder wall. In the following, some of the key simulation results highlighting the influence of the capillary wall on the particle-particle interaction force are depicted.

Figures 3.11 and 3.12 show the variation of the scaled interaction force with scaled separation distance between the particles (κh) under CP conditions on both the particles and the cylinder wall. The results in Figures 3.11 and 3.12 correspond to four values of the scaled particle size (κa), namely, 0.5, 1.0, 2.0, and 5.0, respectively. In all these figures, the force is calculated for a fixed value of the size ratio $\lambda = a/b = 0.83$, and a fixed dimensionless surface potential $\Psi_p = -3.0$ on the particles. For comparison, the interaction force between two particles in an infinite electrolyte is depicted as open symbols in Figures 3.11b

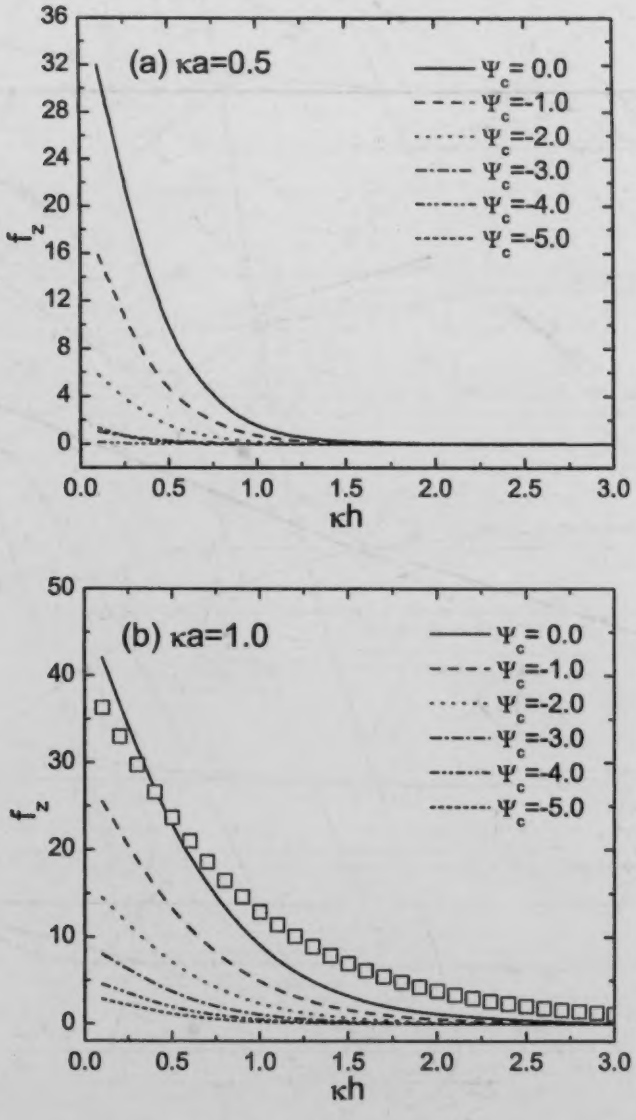

Figure 3.11: Electrostatic interaction force between two particles in a cylindrical capillary corresponding to different cylinder surface potentials. The variations of the scaled electrostatic force with scaled separation between the particles are depicted for a fixed size ratio (λ) of 0.83 and a fixed surface potential, $\Psi_p = -3.0$, on the particles (assuming constant potential particles) for scaled particle sizes $\kappa a = 0.5$ and 1.0. The open symbols in part (b) represent the interaction force between two CP particles in an unbounded electrolyte corresponding to $\kappa a = 1.0$.

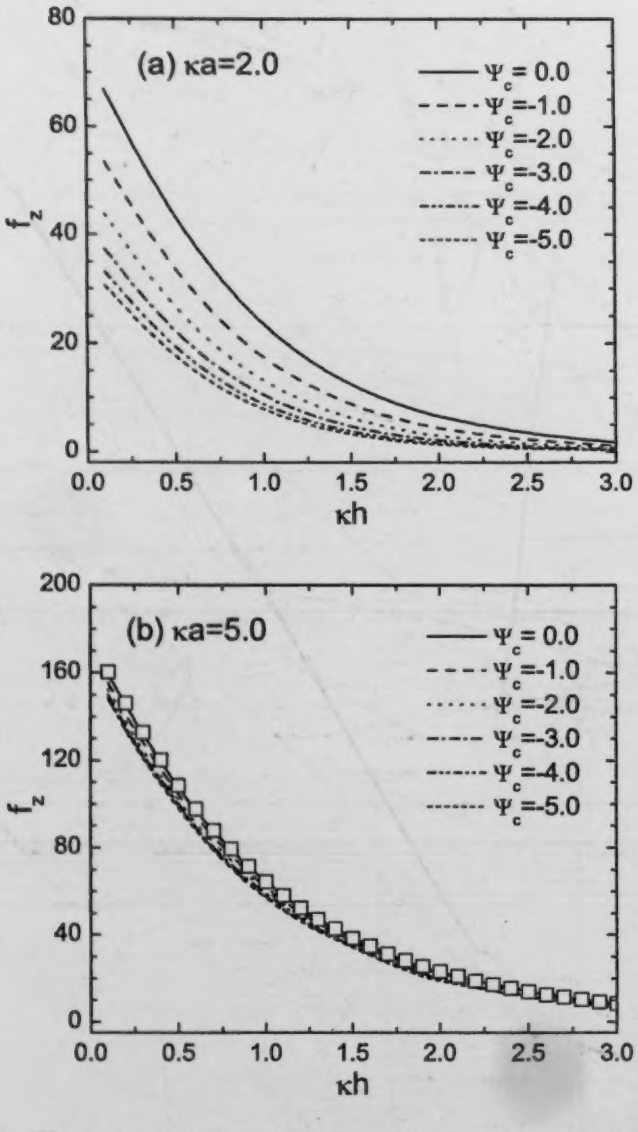

Figure 3.12: Electrostatic interaction force between two particles in a cylindrical capillary corresponding to different cylinder surface potentials. The variations of the scaled electrostatic force with scaled separation between the particles are depicted for a fixed size ratio (λ) of 0.83 and a fixed surface potential, $\Psi_p = -3.0$, on the particles (assuming constant potential particles) for scaled particle sizes $\kappa a = 2.0$ and 5.0. The open symbols in part (b) represent the interaction force between two CP particles in an unbounded electrolyte corresponding to $\kappa a = 5.0$.

and 3.12b corresponding to $\kappa a = 1.0$ and $\kappa a = 5.0$, respectively. These figures indicate that varying the dimensionless cylinder surface potential (Ψ_c) from 0.0 to -5.0 induces a dramatic lowering of the magnitudes of the electrostatic force, particularly for small values of $\kappa a \leq 2.0$. For larger values of κa (Figure 3.12b), the interaction force between the particles is not seriously affected by the charge on the cylinder wall. For small κa (for instance, $\kappa a = 1.0$), the interaction force between the confined particles deviates from the corresponding force between these particles in an infinite medium even when the cylinder wall bears no charge (Figure 3.11b, solid line and symbols).

An important observation from these results is that all of the force profiles remain in the positive quadrant, indicating that the force never changes sign over the scaled separation distances shown ($0.0 < \kappa h < 3.0$). These results corroborate the fact that it is theoretically impossible to obtain electrostatic attraction between two constant potential spherical particles (with same surface potentials) even in charged confined domains [Sader and Chan, 2000]. These results were obtained for a considerably large value of the size ratio compared to the calculations of Bowen and Sharif (1998). Present results also show the same qualitative trends observed by Gray *et al.* (1999), when the particle to cylinder size ratio λ is small.

The forces corresponding to CC conditions on the particle surfaces are shown in Figures 3.13 and 3.14, which indicates a different behaviour compared to the CP cases. These results were obtained under identical parameter settings for the CP simulations. The cylinder wall was assumed to behave as a CP surface in these calculations. It can be seen that the interaction forces for the CC case do not change as dramatically as the corresponding forces for the CP case when the cylinder surface potential is altered. The particle-particle interaction force decays more rapidly for larger cylinder surface potentials. The influence of the cylinder potential on the interaction force is not perceptible for $\kappa a = 5.0$ (Figure 3.14b). Once again, for all combinations of the governing parameters, the force between the particles remains repulsive over the entire range of particle-

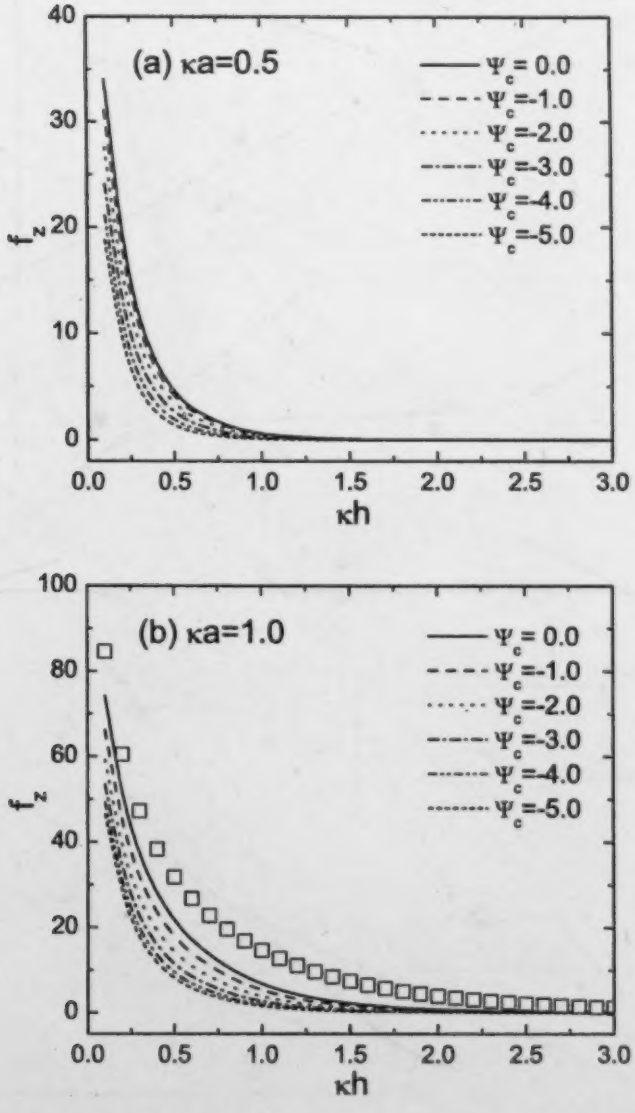

Figure 3.13: Variation of the scaled interaction force between two constant charge (CC) particles corresponding to two values of scaled particle size, $\kappa a = 0.5$ and 1.0, under same conditions as in Figure 3.11. The charge density on the particles was evaluated assuming a surface potential $\Psi_{p,\infty} = -3.0$ on each particle at isolation. The open symbols in part (b) represent the interaction force between two CC particles in an unbounded electrolyte corresponding to $\kappa a = 1.0$.

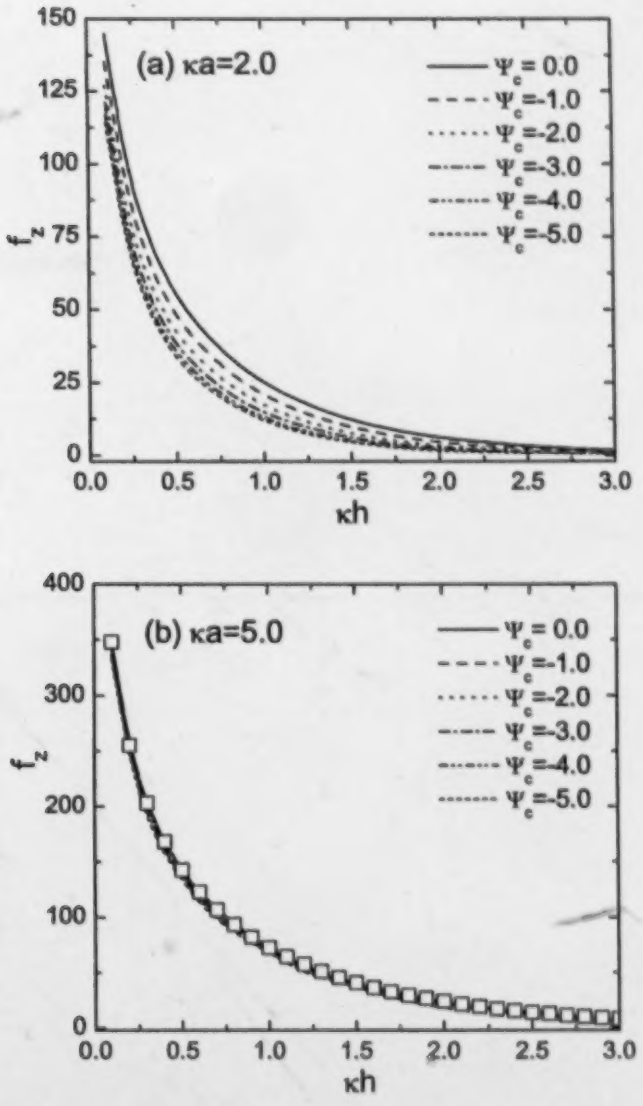

Figure 3.14: Variation of the scaled interaction force between two constant charge (CC) particles corresponding to two values of scaled particle size, κa = 2.0 and 5.0, under same conditions as in Figure 3.12. The charge density on the particles was evaluated assuming a surface potential $\Psi_{p,\infty} = -3.0$ on each particle at isolation. The open symbols in part (b) represent the interaction force between two CC particles in an unbounded electrolyte corresponding to $\kappa a = 5.0$.

particle separations studied. Furthermore, for $\kappa a = 1.0$, the mere presence of an uncharged confining wall alters the magnitude of the electrostatic repulsion between the particles, as seen previously in the CP case (Figure 3.13b, solid line and symbols).

3.5.3 Influence of Proximity of Charged Wall

As observed in Figures 3.11, 3.12, 3.13, and 3.14, which depict the results for $\lambda = 0.83$, the interaction force between the two particles is influenced by the proximity of the charged wall of the confining domain. Figure 3.15 depicts the extent to which the scaled force between two particles at a fixed separation distance $\kappa h = 0.4$ is affected by changes in the size ratio λ for different surface potentials on the cylinder wall. All the results were obtained for $\kappa a = 1.0$ and $\Psi_p = -3.0$, assuming CP boundary conditions on the particles. For fixed surface potentials on the cylinder, the interaction force decreases considerably with increasing values of λ. It is discernable that for small values of λ (when the particles are much smaller than the cylinder radius), the influence of the cylinder surface on the interaction between the particles will be minimal. Accordingly, the interaction force approaches the limiting value of the corresponding force between two particles in an infinite domain as $\lambda \to 0$, irrespective of the magnitude of the cylinder surface potential. The case where the surface potential on the cylinder is zero (uppermost curve in Figure 3.15) indicates that the proximity of the cylinder wall has very little influence on the interaction force between the two particles when it is uncharged.

A similar trend is observed for constant charge (CC) particles, as depicted in Figure 3.16. Here, the change in interaction force induced by variations in λ is more modest compared to the CP results. All the calculations were performed by keeping the simulation parameters same as in Figure 3.15, except for the constant charge boundary condition on the particle surfaces. The interaction force approaches the value of the force between two constant charge particles in an infinite medium as $\lambda \to 0$. The influence of the uncharged cylinder wall

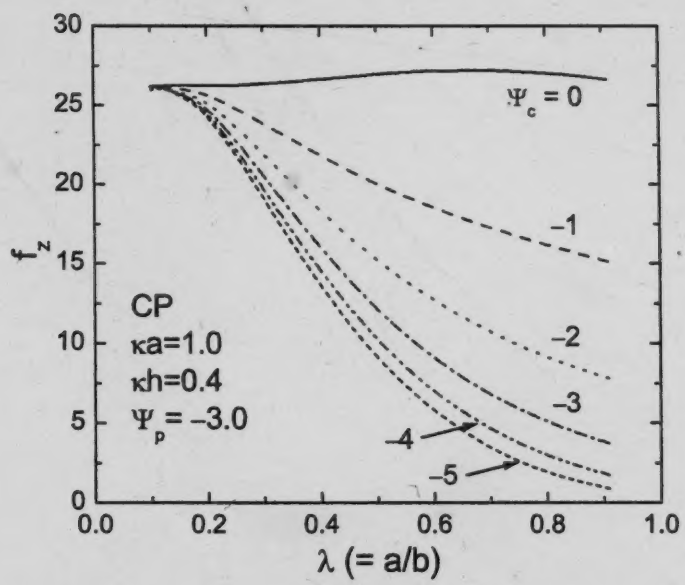

Figure 3.15: Dependence of the particle-particle interaction force on proximity of the charged capillary wall. The dependence of the scaled interaction force between two constant potential (CP) particles on the size ratio λ is shown for several values of the cylinder surface potential.

($\Psi_c = 0.0$) on the particle-particle interaction force is manifested differently compared to the CP case, indicating a much larger influence of the cylinder wall on the interaction force between CC particles as it approaches closer to the interacting particles ($\lambda \geq 0.6$).

An interesting feature in the results corresponding to $\Psi_c = 0.0$ for the constant potential particles (Figure 3.15, uppermost curve) is the presence of a slight maximum near $\lambda = 0.7$. Although the variation of the interaction force between the particles with λ is quite small when the cylinder potential is zero, this behaviour evolves from the variations in the electric field distribution around a given sphere due to the combined influence of the second particle and the proximity of the cylinder wall. When the cylinder wall is far from the particle surface, the electric field around a given particle is primarily influenced by the second particle. As the cylinder radius becomes comparable to the particle radius, it

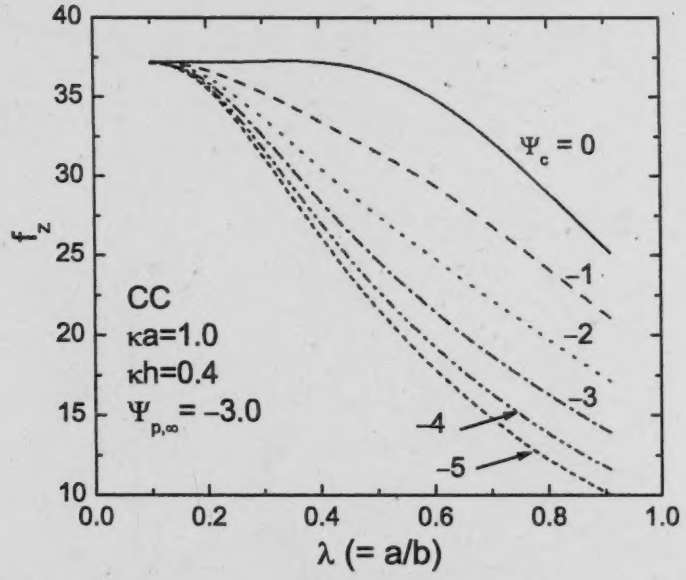

Figure 3.16: Dependence of the scaled particle-particle interaction force on λ for constant charge (CC) particles. Except for the CC boundary condition on the particles, all other parameters are same as in Figure 3.15.

starts to influence the potential distribution around the particle. The maximum interaction force was observed when the particle-particle and the particle cylinder separation distances were equal, *i.e.*, $\kappa h = \kappa(b - a)$. As the cylinder wall approached closer to the particle compared to the other particle, the force was primarily governed by the influence of the capillary wall. The maximum was not observed for the CC boundary conditions (Figure 3.16).

3.5.4 Modulation of Repulsion between Two Particles

Figures 3.17, 3.18, and 3.19 show the variation of the interaction force with scaled separation between the CP particles for four values of the size ratio. Three sets of results are shown, those corresponding to $\Psi_c = -3.0$ in Figure 3.17, those corresponding to $\Psi_c = 0.0$ in Figure 3.18, and those corresponding to $\Psi_c = 3.0$ in Figure 3.19. The other conditions were $\Psi_p = -3.0$, $\kappa a = 1.0$, and CP boundaries on the particles and the capillary wall. For reference, the

interaction force between two particles in an infinite medium is shown as solid lines in Figures 3.17, 3.18, and 3.19. The interaction forces for small values of λ (upright and inverted triangles in Figure 3.17) nearly coincide with the solid lines, indicating very little influence of the charged capillary wall on the particle-particle interaction. As the extent of confinement increases (λ becomes larger), the force between the particles decreases considerably. The corresponding results for the case when the capillary surface potential is zero (Figure 3.18) depicts minor variations in the decay behaviour of the interaction force for the four values of λ, the deviation from the limiting case of two particles in an infinite medium increasing for larger λ. In fact, at small separations, $\kappa h < 0.4$, the interaction force between two particles is greater than the corresponding force between the particles in an infinite medium, although the variation is not quite significant. Hence, when the cylinder potential is zero, it may be assumed that the interaction force between the particles does not undergo a serious alteration with changes in the size ratio. However, the results corresponding to the case when the capillary wall is oppositely charged ($\Psi_c = 3.0$), shows the opposite behaviour compared to the similarly charged cylinder as observed in Figure 3.19. The interaction force between two particles is higher at small separations than the corresponding force between the particles in an infinite electrolyte medium.

The modulation of forces corresponding to constant charge (CC) conditions on the particle surfaces are shown in Figures 3.20, 3.21, and 3.22. These results were obtained under identical parameter settings for the CP simulations. For comparison, the interaction force between two constant charged particles in an infinite medium is shown as solid lines in these figures. It can be seen that the influence of the charged capillary wall on the interaction force is less compared to the CP case (see Figures 3.17 and 3.19). The force between the particles is modified noticeably for $\lambda = 0.83$ when the cylinder bears the same potential as the particles. However, the variation of force is less significant for $\Psi_c = 0.0$ and 3.0. In both cases, the interaction force between the particles does not undergo a serious alteration with changes in the size ratio.

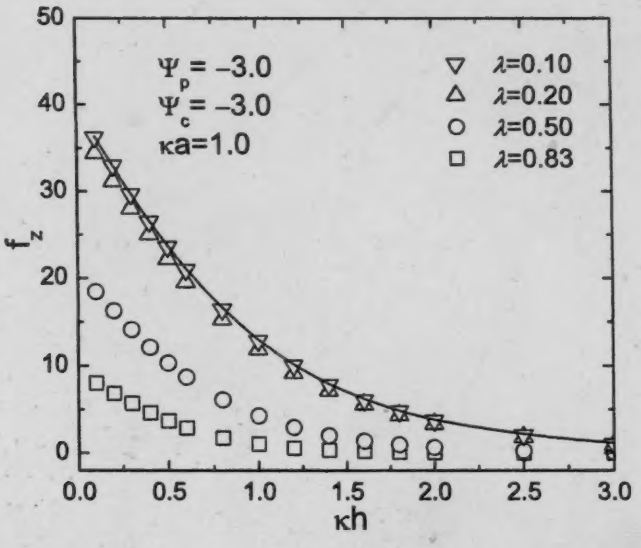

Figure 3.17: Interaction force at different scaled separations between constant potential (CP) particles corresponding to scaled cylinder surface potential, $\Psi_c = -3.0$ for different size ratios (λ). The solid line depicts the interaction force between two particles in an unbounded electrolyte.

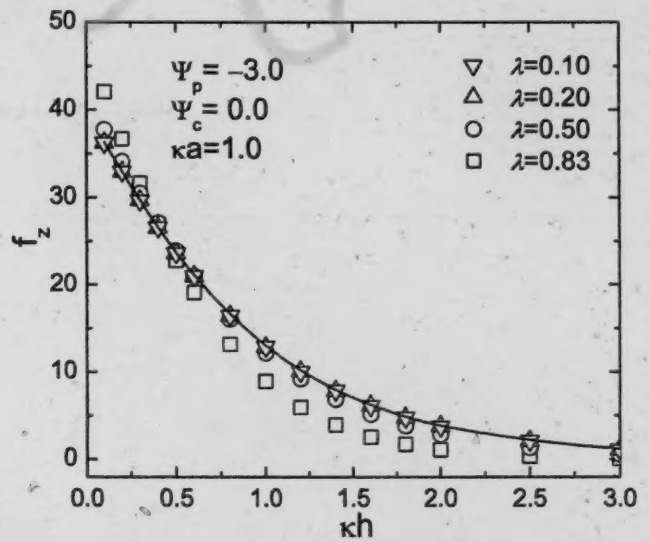

Figure 3.18: Interaction force at different scaled separations between constant potential (CP) particles corresponding to scaled cylinder surface potential, $\Psi_c = 0.0$ for different size ratios (λ). The solid line depicts the interaction force between two particles in an unbounded electrolyte.

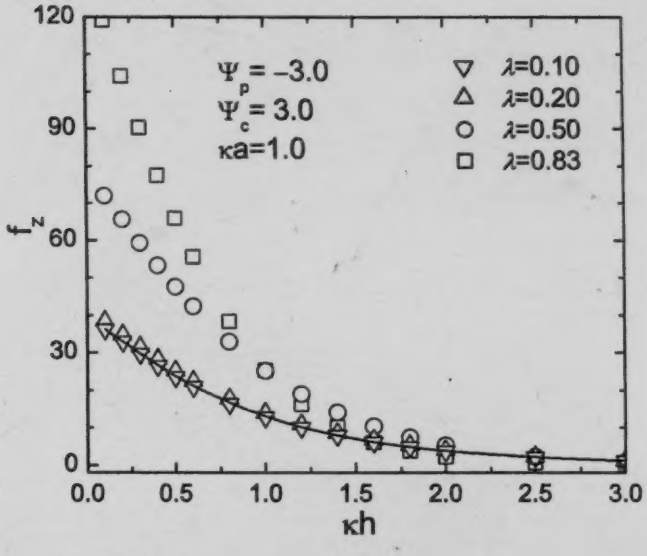

Figure 3.19: Interaction force at different scaled separations between constant potential (CP) particles corresponding to scaled cylinder surface potential, $\Psi_c = +3.0$ for different size ratios (λ). The solid line depicts the interaction force between two particles in an unbounded electrolyte.

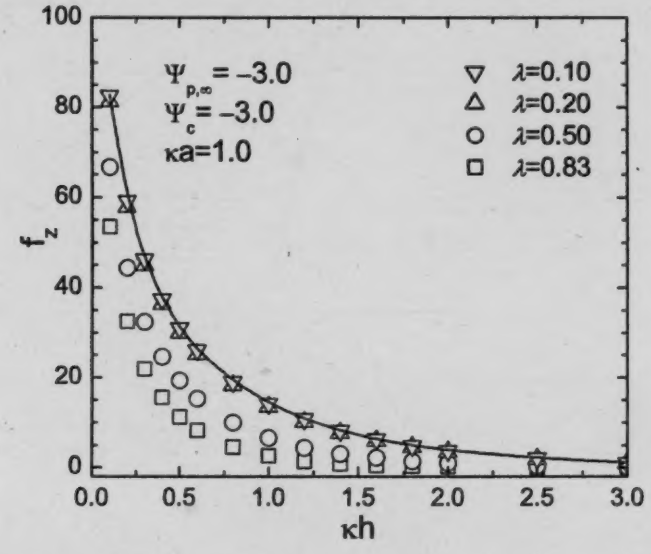

Figure 3.20: Interaction force at different scaled separations between constant charge (CC) particles corresponding to scaled cylinder surface potential, $\Psi_c = -3.0$. The solid line depicts the interaction force between two particles in an unbounded electrolyte.

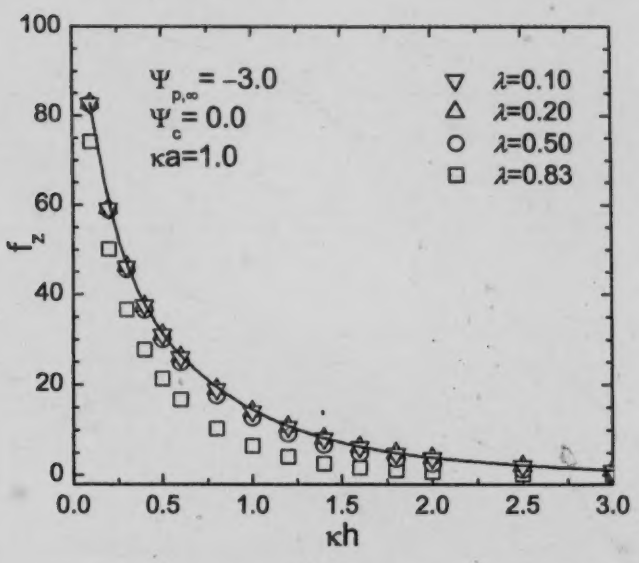

Figure 3.21: Interaction force at different scaled separations between constant charge (CC) particles corresponding to scaled cylinder surface potential, Ψ_c = 0.0. The solid line depicts the interaction force between two particles in an unbounded electrolyte.

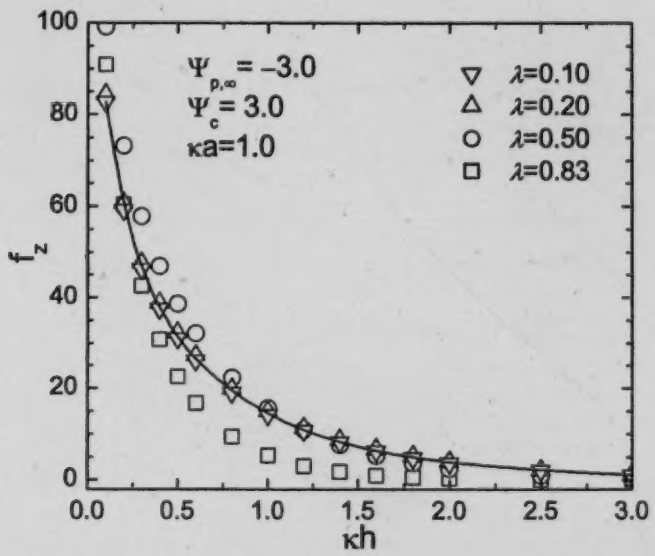

Figure 3.22: Interaction force at different scaled separations between constant charge (CC) particles corresponding to scaled cylinder surface potential, Ψ_c = +3.0. The solid line depicts the interaction force between two particles in an unbounded electrolyte.

The large difference in the interaction forces between the constant potential particles corresponding to the cases when the cylinder surface potential has a finite value (On) depicted in Figures 3.17 and 3.19, and is zero depicted in Figure 3.18, may be utilized as a control mechanism for the short-range ($\kappa h < 1.0$) colloidal forces between the particles. For instance, switching the scaled surface potential of the cylinder between zero and -3.0 while keeping the particle separation fixed at $\kappa h = 0.4$ can induce an almost one order of magnitude change in the electrostatic interaction force for $\lambda = 0.83$ (Figures 3.17 and 3.18). Although the van der Waals interactions were not calculated in this study, it may be speculated that combined with the attractive van der Waals interaction, the modified electrostatic force might lead to a net attractive DLVO force between the particles when the cylinder potential is turned on. In other words, the presence of the charged confining wall might lead to a reduction in the repulsive energy barrier between the colloidal particles. In this manner, there might exist a possibility of a short range DLVO attraction (or at least a substantial reduction in the repulsive interaction) that can induce particle aggregation. It is however emphasized that this attraction will not be solely due to electrostatic forces, which always remains repulsive. Furthermore, this overall DLVO attraction is manifested only at short inter-particle separations and for large values of the parameter λ.

3.5.5 Interaction Force for Oppositely Charged Cylinder and Particles

Figures 3.23 and 3.24 show the variation of the scaled interaction force between two constant potential particles inside an oppositely charged cylindrical capillary (as indicated in the legend) with scaled separation distance between the particles (κh). The results in Figures 3.23 and 3.24 correspond to a fixed value of the size ratio $\lambda = 0.83$, and a fixed dimensionless surface potential $\Psi_p = -3.0$ on the particles while the capillary surface potential is considered as opposite in sign. For comparison, the interaction force between two particles in an infi-

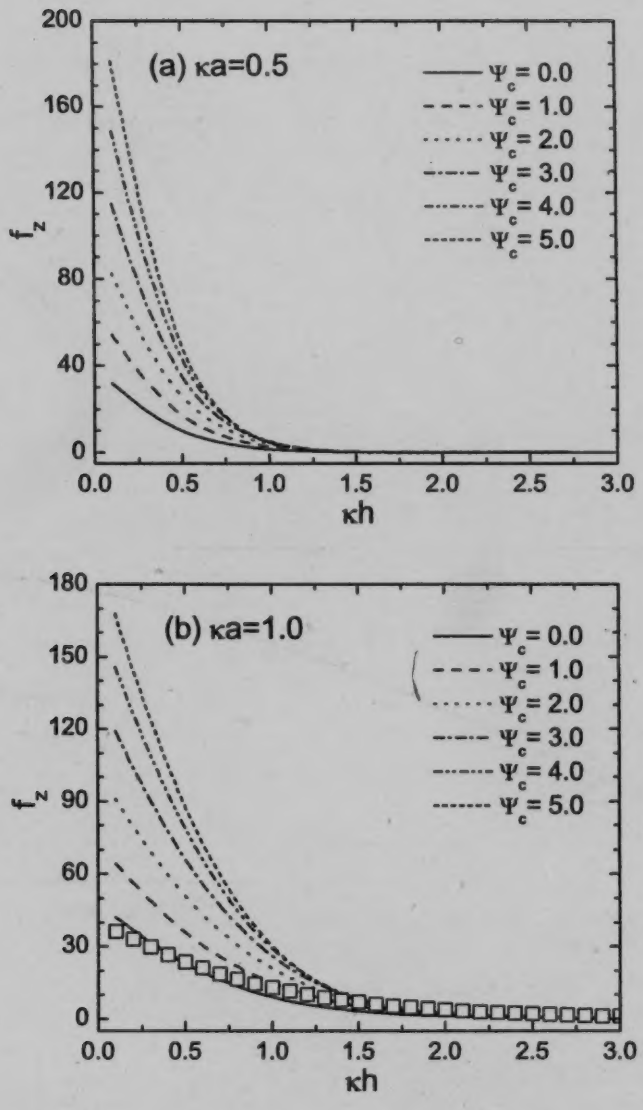

Figure 3.23: Electrostatic interaction force between two constant potential (CP) particles inside an oppositely charged cylindrical capillary as indicated in the legend. The variations of the scaled electrostatic force with scaled separation between the particles are depicted for a fixed size ratio (λ) of 0.83 and a fixed surface potential, $\Psi_p = -3.0$, on the particles (assuming constant potential particles) for two values of scaled particle size, $\kappa a = 0.5$ and 1.0. The open symbols in part (b) represent the interaction force between two CP particles in an unbounded electrolyte corresponding to $\kappa a = 1.0$.

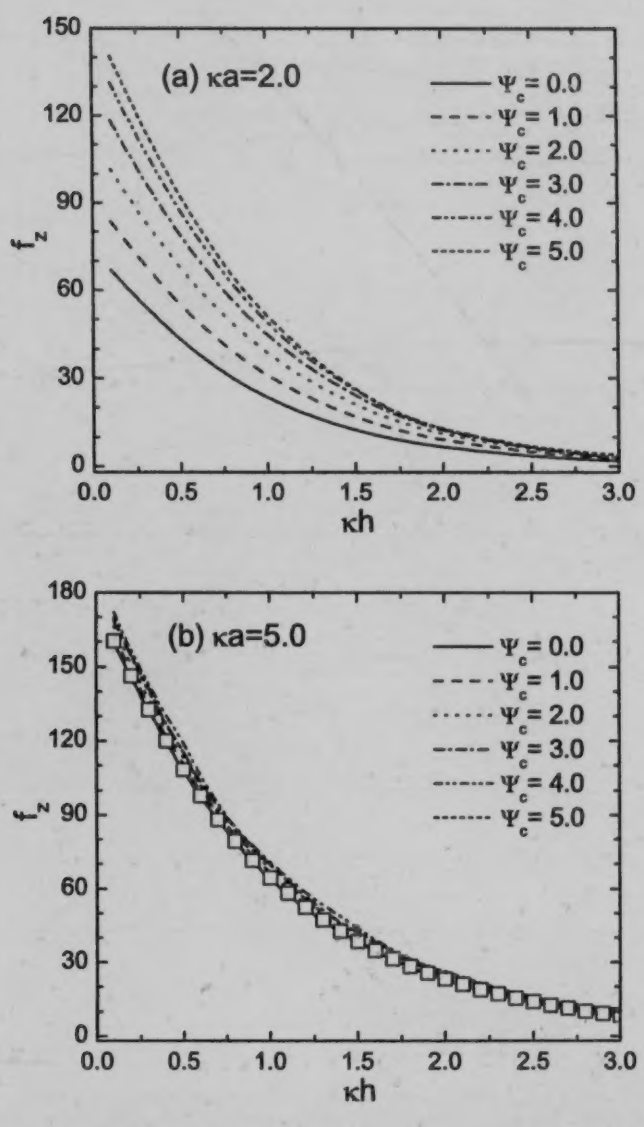

Figure 3.24: Electrostatic interaction force between two constant potential (CP) particles inside an oppositely charged cylindrical capillary as indicated in the legend. The variations of the scaled electrostatic force with scaled separation between the particles are depicted for a fixed size ratio (λ) of 0.83 and a fixed surface potential, $\Psi_p = -3.0$, on the particles (assuming constant potential particles) for two values of scaled particle size, $\kappa a = 2.0$ and 5.0. The open symbols in part (b) represent the interaction force between two CP particles in an unbounded electrolyte corresponding to $\kappa a = 5.0$.

nite electrolyte domain is depicted as open symbols in Figures 3.23b and 3.24b corresponding to $\kappa a = 1.0$ and $\kappa a = 5.0$, respectively. These figures indicate that changing the dimensionless cylinder surface potential (Ψ_c) from 0.0 to +5.0 increases the magnitudes of the electrostatic force on a particle, particularly for small values of $\kappa a \leq 2.0$. Here, the variation of interaction forces are large compared to the case of similarly charged capillary. For instance, at $\kappa a = 2.0$ and $\kappa h = 0.1$, the force when the capillary wall potential is +5.0 is over two times larger than the force when the cylinder bears no charge. For larger values of κa, the charged cylinder has less effect on the interaction force between the particles (see Figure 3.24b). Figure 3.23b shows that the interaction forces between the particles inside a cylindrical capillary with zero surface potential differ from the corresponding forces between these particles in an infinite medium. As in Figure 3.11b, such a deviation represents the influence of confinement.

A different trend is observed for constant charge (CC) particles, as depicted in Figures 3.25 and 3.26 for four different particle sizes (κa) as mentioned in the legend. As observed in Figures 3.11 and 3.12 for CP cases, for similarly charged particles and capillary, varying the dimensionless cylinder surface potential (Ψ_c) from 0.0 to -5.0 shows a reduction of force, and for oppositely charged case shows a magnification of force (Figures 3.23 and 3.24). This cannot be said for constant charge particles. For smaller particles (for instance $\kappa a = 0.5$), varying the dimensionless cylinder surface potential (Ψ_c) from 0.0 to +5.0 always reduces the force between the two oppositely charged particles as observed in the case of similarly charged particles and cylinder. Larger particles ($\kappa a \geq 2.0$) show a slight magnification of force when the cylinder potential is varied form 0.0 to +5.0. A slightly complicated behaviour is observed for $\kappa = 1.0$. When the magnitude of the cylinder potential is less than the particle potential, varying the cylinder potential induces little magnification of force. For $|\Psi_c| \geq |\Psi_p|$, the force between two CC particles also depends on their separation. For $\Psi_c = +5.0$, the force is magnified compared to the force between the particles inside an uncharged cylindrical capillary for small separations, particularly when $\kappa h \leq$

$\kappa(b-a)$. On the other hand, the force is reduced due to the presence of charged cylinder at large separation distances.

Figure 3.27 depicts the interaction force for cases where the cylinder surface is oppositely charged with respect to the particles. The figure depicts the interaction force on a particle for $\kappa a = 1.0$, $\kappa h = 0.4$ and for a fixed value of the particle surface potential, $\Psi_p = -3.0$. Figure 3.27a depicts the variation of the interaction force with size ratio (λ) for CP particles corresponding to different values of the cylinder surface potential. With increasing values of λ and the cylinder surface potential, the magnitude of the repulsive force increases. Comparing Figure 3.27a with Figure 3.15 indicates that while the net interaction force on the particle increases for oppositely charged cylinder surfaces (Figure 3.27a), it decreases for like-charged cylinder and particles (Figure 3.15). The results further indicate that the short-range repulsion between the particles can be dramatically amplified by trapping these in an oppositely charged cylindrical cavity.

The simulations of Figure 3.27b were performed under identical conditions as in Figure 3.27a, except for CC conditions on the particles. A similar increase of the interaction force between the spherical particles is observed when these are assigned CC boundary conditions for $0.1 < \lambda < 0.4$ (Figure 3.27b). At larger values of λ, however, the interaction force starts decreasing. For $\lambda > 0.8$, the interaction force corresponding to different cylinder surface potentials are quite close ($20 < f_z < 30$), implying that for constant charge particles in a tightly fitting capillary, there will be very little influence of the capillary wall surface potential on the net interaction force on a particle.

These different behaviours of the interaction force for CP and CC particles in an oppositely charged capillary (specifically at large values of λ) might be helpful in distinguishing between different charging behaviours of the particles. For instance, from an inspection of the interaction forces between the particles as the cylinder wall is charged up, one might be able to conclude whether the particles are CP or CC, depending on whether the interaction force increases

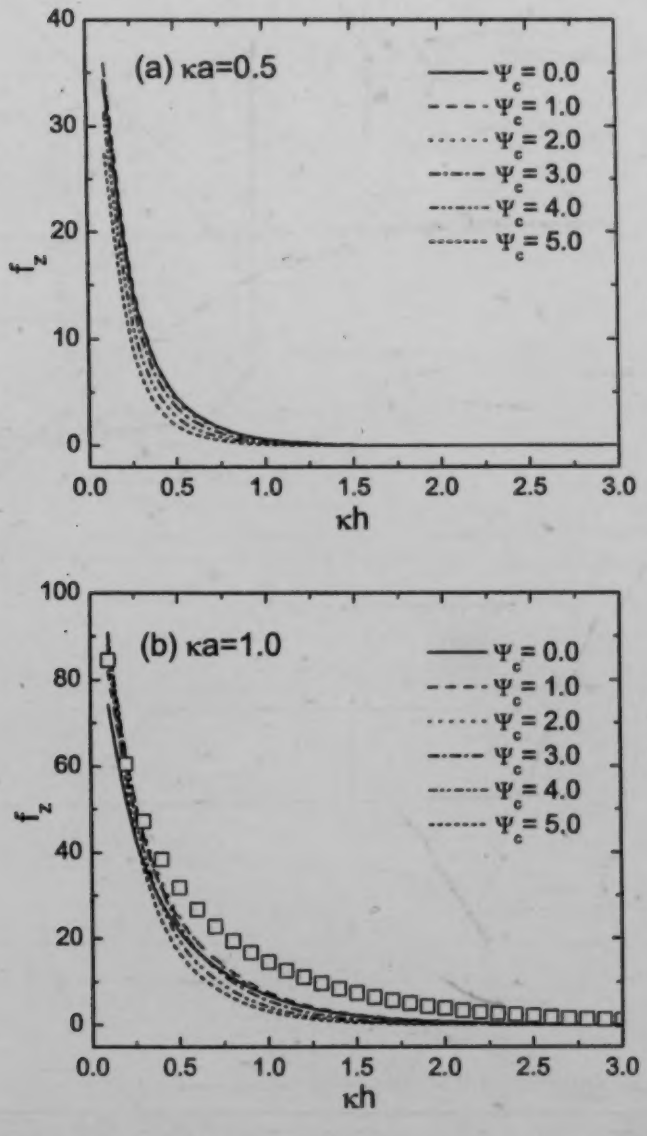

Figure 3.25: Variation of the scaled interaction force between two constant charge (CC) particles corresponding to two values of scaled particle size, $\kappa a =$ 0.5 and 1.0, under same conditions as in Figure 3.23. The charge density on the particles was evaluated assuming a surface potential $\Psi_{p,\infty} = -3.0$ on each particle at isolation. The open symbols in part (b) represent the interaction force between two CC particles in an unbounded electrolyte corresponding to $\kappa a = 1.0$.

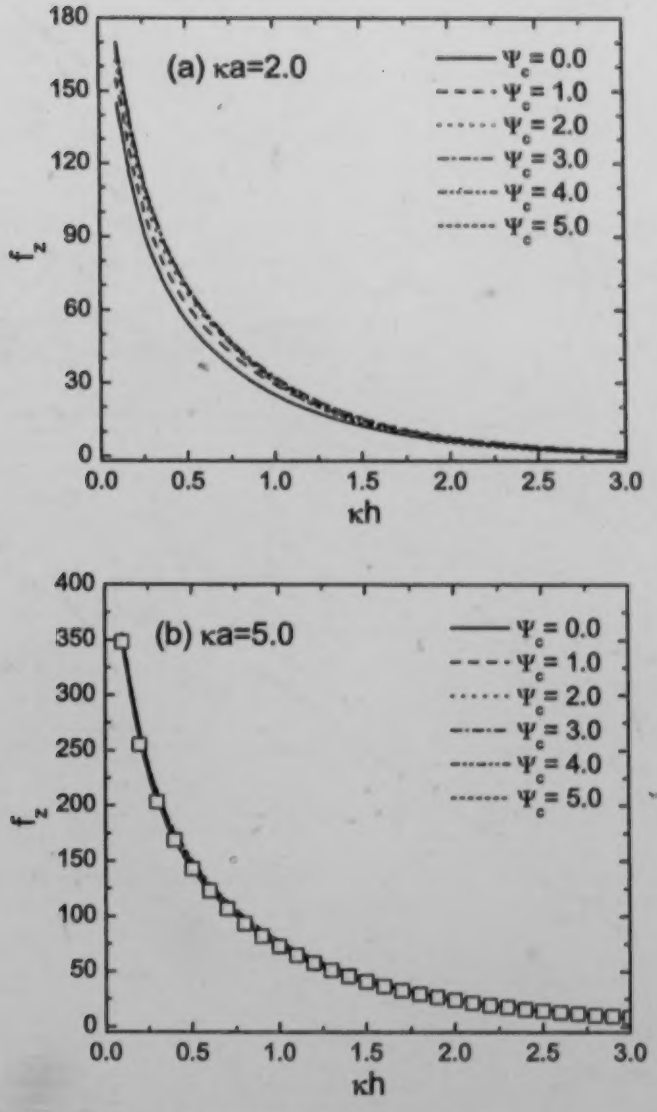

Figure 3.26: Variation of the scaled interaction force between two constant charge (CC) particles corresponding to two values of scaled particle size, κa = 2.0 and 5.0, under same conditions as in Figure 3.24. The charge density on the particles was evaluated assuming a surface potential $\Psi_{p,\infty} = -3.0$ on each particle at isolation. The open symbols in part (b) represent the interaction force between two CC particles in an unbounded electrolyte corresponding to $\kappa a = 5.0$.

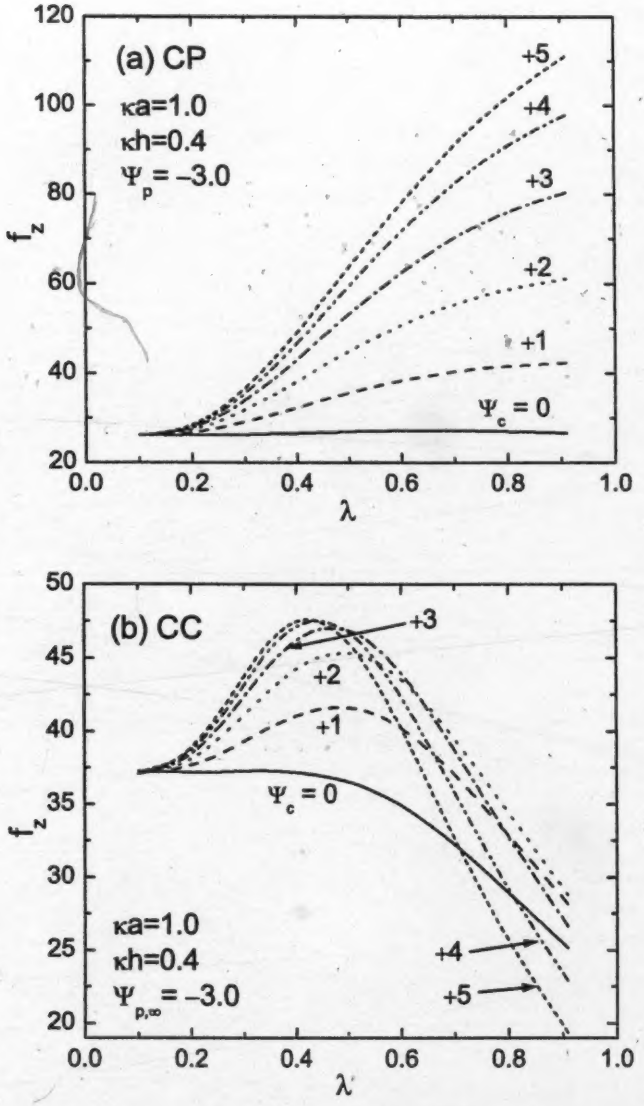

Figure 3.27: Interaction force between two identically charged particles inside an oppositely charged capillary. The variation of the force with size ratio is shown for different cylinder surface potentials. Part (a) depicts the scaled interaction force for constant potential (CP) particles, while part (b) shows the scaled interaction force for constant charge (CC) particles.

considerably or remains relatively unperturbed, respectively.

The short-range electrostatic interaction force between the particles was always repulsive as long as the particles were similarly charged (same surface potential or surface charge density), even when the cylindrical wall was oppositely charged. In fact, for CP particles, an increase in the repulsive force was observed when the sign of the cylinder surface potential was opposite to the particle surface potential.

The increase in the interaction force between two similarly charged particles inside an oppositely charged cylindrical capillary can be explained by considering how the electric fields around the particles are altered by the proximity of an oppositely charged surface. When an oppositely charged cylindrical wall approaches a spherical particle, the potential gradients around the particle become larger (the surface charge density of the sphere increases). Hence, the two particles will "see" each other as if they are becoming more charged as the cylinder wall approaches them. The increase is more prominent for constant potential particles (Figure 3.27a). The variation of the interaction force for constant charge particles originates from the distortion of the electric potential distribution around the particles in presence of the oppositely charged cylinder wall. Although the charge densities of the particles remain fixed, the potential distribution around each particle is altered by the presence of the cylinder, which in turn modifies the osmotic stress around the particles. The variations of the osmotic stress cause the variation of the interaction force as the cylinder wall approaches the particles (Figure 3.27b).

3.5.6 Summary

To summarize, the solution of non-linear Poisson-Boltzmann equation to obtain the electrostatic interaction force between two particles confined in a straight cylindrical capillary shows a large influence of the proximity of the charged cylinder wall on the net particle-particle electrostatic interaction force. The

influence of the charged cylinder wall is most prominent when the cylinder radius is comparable to the particle radii. An interesting phenomenon observed in these simulations is that while like-charged cylinder surfaces tend to reduce the magnitude of the repulsion, oppositely charged walls considerably amplify the repulsion. Furthermore, the influence of the charged cylinder is more pronounced when the particles have constant potential surfaces.

In developing the finite element based solution procedure, it has also been demonstrated that the short-range electrostatic interaction force between two spherical particles in an infinite domain can be evaluated accurately in a cylindrical coordinate system. Furthermore, these results show that integration of the stress tensor over the surface of the particles yields a correct estimate of the interaction force.

Chapter 4

Influence of Roughness on Particle-Particle Electrostatic Interaction

4.1 Introduction

The purpose of this chapter is to investigate the influence of capillary wall surface roughness on the electrostatic interaction forces between two nanoparticles inside an infinitely long capillary. As discussed in Chapter 2, literature related to roughness analysis were mainly restricted to studies on the Lifshitz-van der Waals (LW) interaction between colloidal particles in an infinite medium. None of the previous studies investigate the effect of roughness on the electrostatic double layer (EDL) component of the DLVO interaction in confined domains. Here, the finite element predictions of EDL interaction forces between two similarly charged spherical nanoparticles trapped inside an infinitely long "rough" capillary are reported.

4.2 Mathematical Modelling

The behaviour of charged particles suspended in an electrolyte medium inside a charged domain can be analyzed by solving the non-linear Poisson-Boltzmann (NLPB) equation with appropriate boundary conditions imposed on the charged

particles and capillary surfaces. Here, a brief description of the mathematical formulation, particularly focusing on the procedures for generating the rough capillary wall is described along with some key steps of the numerical solution procedure.

4.2.1 Computational Domain, Governing Equation, and Boundary Conditions

In this subsection, the mathematical formulation of the problem considered in terms of the non-linear Poisson-Boltzmann equation is presented with the pertinent boundary conditions. Here, two spherical colloidal particles of radius a are separated by a distance h (distance of closest approach) in an infinitely long "rough" capillary of mean radius b. The pitch (or wavelength) of the roughness is denoted by δ, and amplitude of the roughness is denoted by α as shown in Figure 4.1. Two different cases are considered depending upon the relative particle position inside the capillary. Case−I (Figure 4.1a) considers the crest of the wave as a reference point (R), while Case−II (Figure 4.1b) considers the trough of the undulating capillary as the reference point (R). The interaction forces between the particles are determined for each of these cases at various separation distances relative to the reference point R. The ratio of the particle radius to the mean radius of the cylindrical capillary is denoted as the size ratio λ $(= a/b)$.

Utilizing the axisymmetry when the particles are axially located in the capillary, the governing Poisson-Boltzmann (PB) equation can be written in the cylindrical coordinate system as (*cf.* Eq. 4.1)

$$\frac{\partial^2 \Psi}{\partial \bar{r}^2} + \frac{\partial^2 \Psi}{\partial \bar{z}^2} = \sinh(\Psi) - \frac{1}{\bar{r}} \frac{\partial \Psi}{\partial \bar{r}} \tag{4.1}$$

where Ψ $(= \frac{\nu e \psi}{kT})$ is the scaled potential and the scaled coordinates are $\bar{r} = \kappa r$ and $\bar{z} = \kappa z$. The scaling parameter here is the inverse Debye screening length, κ, for a symmetric $(\nu : \nu)$ electrolyte (see Eq. (3.15)).

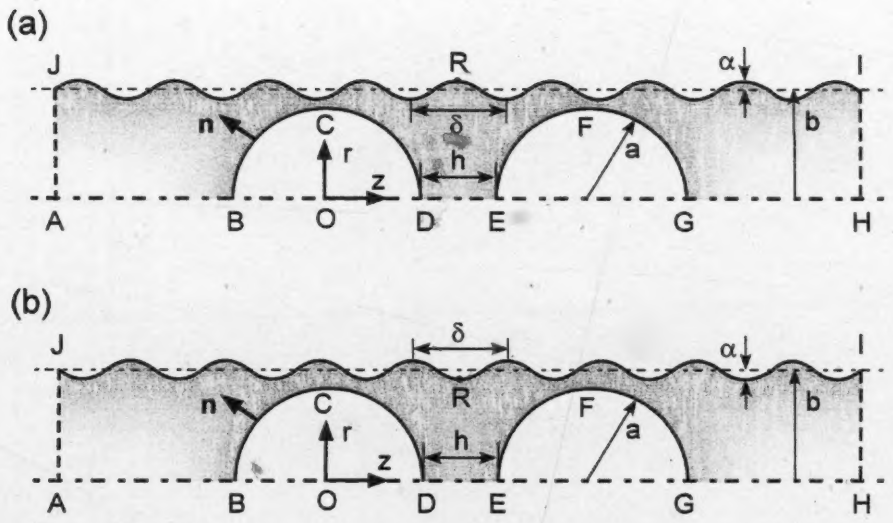

Figure 4.1: Schematic representation of the computational domain for two spherical colloidal particles inside a "rough" capillary. (a) particles are moving uniformly from the crest of an undulation denoted by the point R (Case−I), (b) particles are moving uniformly from the trough of an undulation (Case−II). Utilizing the symmetry around the horizontal axis (AH), the two-dimensional formulation of the governing equation was developed. The arcs BCD and EFG represent the particle surfaces, while IJ represents the undulation of the capillary. The origin of the cylindrical coordinate system is located at O.

The particle surfaces may be treated as either constant surface potential (CP) or constant surface charge density (CC) boundaries. In the previous chapter, both CP and CC cases were considered to evaluate the interaction forces between two spherical colloidal particles inside a charged straight cylindrical capillary. It was observed that the interaction force between the particles was affected significantly by the proximity of the charged capillary wall only for constant surface potential particles. Accordingly, in this chapter only constant surface potential boundary condition is considered for both the particles and the capillary wall. The boundary conditions for the problem (as depicted graphically in Figure 4.1) are summarized as

$$\Psi = \Psi_p \text{ for } \partial\Omega \in \text{ BCD and EFG} \tag{4.2a}$$

$$\Psi = \Psi_c \text{ for } \partial\Omega \in \text{ IJ} \tag{4.2b}$$

$$\mathbf{n} \cdot \nabla\Psi = 0 \text{ for } \partial\Omega \in \text{ AB, DE, GH, HI, and JA} \tag{4.2c}$$

Eq. (4.2c) provides the symmetry conditions on the fluid boundaries, implying that the potential gradients normal to these line segments are zero. In this equation, $\mathbf{n}$ represents the unit outward normal to the surface.

4.2.2 Generation of a Rough Surface

Numerous approaches have been proposed for generating surface roughness and subsequent evaluation of the interaction between rough surfaces as mentioned earlier in Chapter 2. In this study, a simple technique based on Bézier curves is utilized to generate the wavy pattern on the capillary wall to simulate roughness. Bézier curves are most frequently used in computer graphics and geometric modelling. For a set of $(n+1)$ control points P_0, P_1, P_2, ..., P_n the corresponding Bézier curve is given by [Shikin and Plis, 1995]

$$b(t) = \sum_{i=0}^{n} P_i B_{i,n}(t) \tag{4.3}$$

where $B_{i,n}(t)$ is a Bernstein polynomial defined as

$$B_{i,n}(t) = \binom{n}{i} t^i (1-t)^{n-i} \tag{4.4}$$

For numerical calculation a "rational" Bézier curve is defined by

$$b(t) = \frac{\sum_{i=0}^{n} w_i P_i B_{i,n}(t)}{\sum_{i=0}^{n} w_i B_{i,n}(t)}, \quad t \in [0,1] \tag{4.5}$$

where n is the order, $B_{i,n}$ are the Bernstein polynomials, P_i are control vertices of the n-dimensional space, and w_i are the weights which should always be positive real numbers to get a properly defined rational Bézier curve. The Bézier curve always passes through the first and last control points and lies within the convex hull of the control points. One of the most useful property of the rational Bézier

curves is that the direction of the tangent vector at $t = 0$ and $t = 1$ is determined by the vectors $P_1 - P_0$ and $P_n - P_{n-1}$, respectively. In other words, the curve will always be tangent to the line connecting control vertices P_0 and P_1, and also to the line connecting P_{n-1} and P_n. Here quadratic Bézier curve is used to avoid numerical instability associated with higher order Bézier curves. Three control points are needed to define a quadratic Bézier curve. Considering three control points P_0, P_1 and P_2, a quadratic Bézier curve is defined as

$$P(t) = (1-t)^2 P_0 + 2t(1-t)P_1 + t^2 P_2 \tag{4.6}$$

Here t is a parameter between 0 and 1, where $P(0) = P_0$ and $P(1) = P_2$, so the curve passes through the control points P_0 and P_2. The functions $(1-t)^2$, $2t(1-t)$, and t^2 that are used to "blend" the control points P_0, P_1 and P_2 together, are the second degree Bernstein polynomials. Equation (4.6) is a linear combination of quadratic polynomials, and therefore it is a parabolic segment. Thus, the quadratic Bézier curve is simply a continuous parabolic curve and has continuous derivatives of all orders. Substituting Eq. (4.4) and Eq. (4.6) into Eq. (4.5), the final form of the quadratic Bézier curve is written as

$$b(t) = \frac{w_0(1-t)^2 P_0 + 2w_1 t(1-t)P_1 + w_2 t^2 P_2}{w_0(1-t)^2 + 2w_1 t(1-t) + w_2 t^2} \tag{4.7}$$

Throughout this study, w_0 and w_2 are kept constant to maintain symmetry over the point P_1, w_1 is varied to control the amplitude of the roughness, while the two end or anchor points are used to vary the pitch. If P_1 and w_1 are known, the amplitude of the asperities can be calculated from the following relationship

$$\alpha = \frac{P_1}{1 + w_1} \tag{4.8}$$

4.2.3 Calculation of Electrostatic Interaction Force

The net electrostatic force between the two particles is calculated by integrating the stress tensor, Eq. (3.19), over the surface of the particles. Since the integration of the osmotic pressure term over a closed surface of constant potential

is always zero, the net electrostatic force acting on a particle along the axial (z) direction can be written explicitly as

$$F_z = \mathbf{F} \cdot \mathbf{k} = 2\pi\kappa^2\varepsilon\varepsilon_0 \left(\frac{kT}{\nu e}\right)^2 \int_{BCD} \left[n_r \Psi_r \Psi_z + \frac{1}{2} n_z \left(\Psi_z^2 - \Psi_r^2\right)\right] r dr \qquad (4.9)$$

where $\mathbf{k}$ is the unit normal in the positive z direction, n_r and n_z are the components of the unit normal along the r and z direction, respectively, and BCD represents the semi-circular boundary of the spherical particle over which the integration is performed (see Figure 4.1). Ψ_r and Ψ_z are the components of the electric field vector $\mathbf{E}$ along the r and z directions, respectively.

4.3 Results and Discussions

The numerical solution of the non-linear Poisson-Boltzmann equation was performed using finite element method as described in Chapter 3. Here a generalized technique is employed that is available in FEMLAB software. Detailed procedure of the numerical technique is available in the previous chapter. Here, we only present the simulation results for the interaction force experienced by the spherical particle inside an infinitely long "rough" capillary for various combinations of the roughness parameters to explore the key effects of surface roughness on the interparticle interaction. Effect of surface roughness of the capillary wall, as determined by amplitude and pitch of the undulations, on the interaction force between two particles is obtained for dimensionless surface roughness η (defined as the ratio of roughness amplitude, α to particle radius, a) ranging from $0.0 - 0.15$, scaled wavelengths ξ (defined as the ratio of pitch of the undulations, δ to particle radius, a) ranging from $0.4 - 4.0$, and different combinations of the surface potentials on the particles and the capillary wall.

4.3.1 Potential Distribution and Fields Inside the Rough Capillary

The potential variation and the electrostatic field variation inside the "rough" capillary are both presented in terms of iso-potential lines and iso-gradient lines in Figures 4.2 and 4.3, respectively, for the case when the particles are placed at a equal distance from the crest of an undulation (Case−I). Results shown in these figures are corresponding to scaled amplitude of the roughness $\eta = 0.1$, and scaled pitch $\xi = 1.0$. Three parts (a−c) in Figures 4.2 and 4.3 represent three values of the capillary surface potential (Ψ_c), namely, $-3.0, 0.0$, and $+3.0$, respectively. The other conditions were $\Psi_p = -3.0$, $\kappa a = 1.0$, and $\kappa h = 0.5$. The potential distribution inside the capillary decays slowly for $\Psi_c = -3.0$ as shown in Figure 4.2a., whereas this decaying behaviour was more rapid for $\Psi_c = 0.0$ and -3.0. This was mainly due to the magnitude of the cylinder potential. Since the potential distribution changes with change of the surface potential of the capillary, this alteration in the potential distribution changes the electrostatic field quite remarkably, as shown in Figure 4.3. Most notable in these figures are the peak values of the electrostatic field. For similarly charged particles and capillary (Figure 4.3a), the variation of the electrostatic field is quite modest whereas significant variation is observed for two other cases (Figures 4.3b and 4.3c). This kind of dramatic variation implies that the electrical stress in both the radial and the axial direction will vary markedly. However, due to the axial symmetry, the net force in the radial direction will not be affected. Both Figures 4.3b and 4.3c also reveal the direction of the axial force. As observed in these two figures, the highest gradient point is mainly induced by the particle-capillary interaction. The localized fields at the points of closest approach between a particle and the rough capillary will modify the net electrostatic stress on the particles. If this stress is directed away from the mid-plane between the particles, there will be a net enhancement in the repulsion between the particles. Thus, the roughness of the wall will induce an oscillatory behaviour of the force as the particles move away from the point R

(a) $\Psi_c = -3.0$.

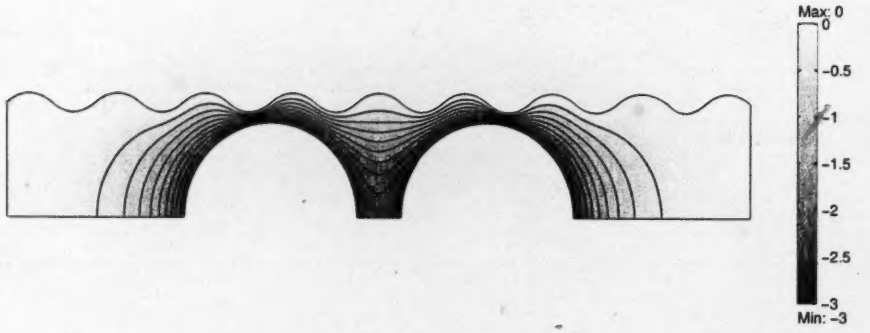

(b) $\Psi_c = 0.0$.

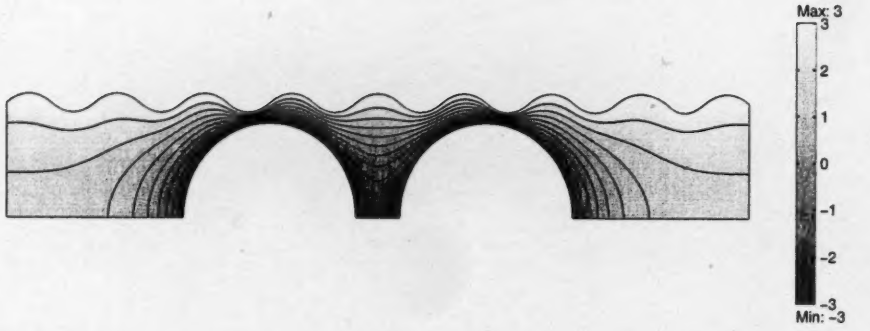

(c) $\Psi_c = +3.0$.

Figure 4.2: Potential distribution of two spherical particles inside an infinitely long "rough" capillary corresponding to three different capillary surface potentials as mentioned in the legend for the situation when particles are moving uniformly from the crest of an undulation (Case−I).

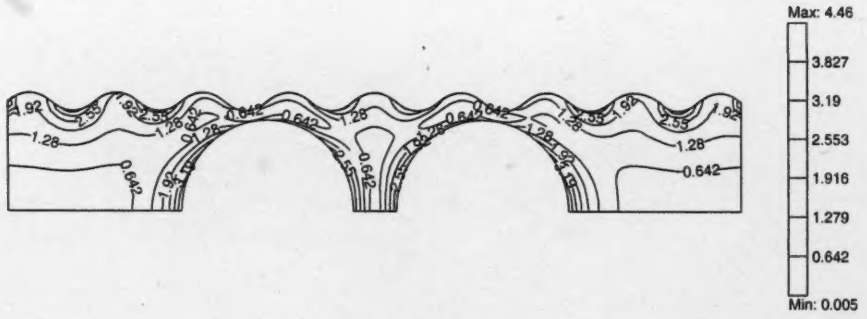

(a) $\Psi_c = -3.0$.

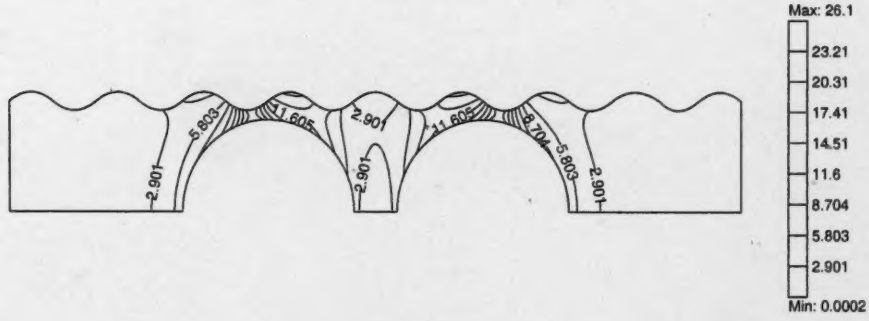

(b) $\Psi_c = 0.0$.

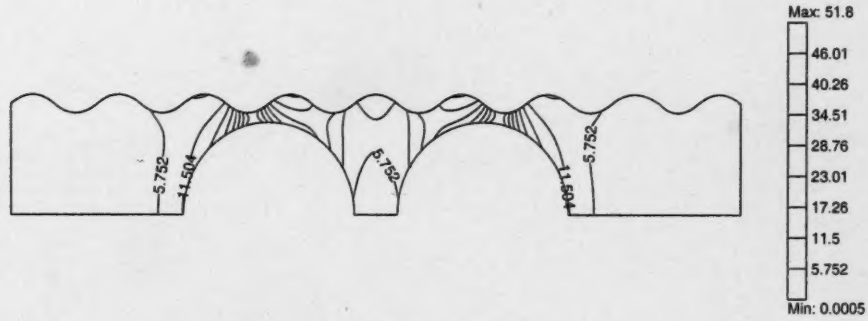

(c) $\Psi_c = +3.0$.

Figure 4.3: Electrostatic field distribution inside an infinitely long "rough" capillary corresponding to three different capillary surface potentials as mentioned in the legend for Case−I.

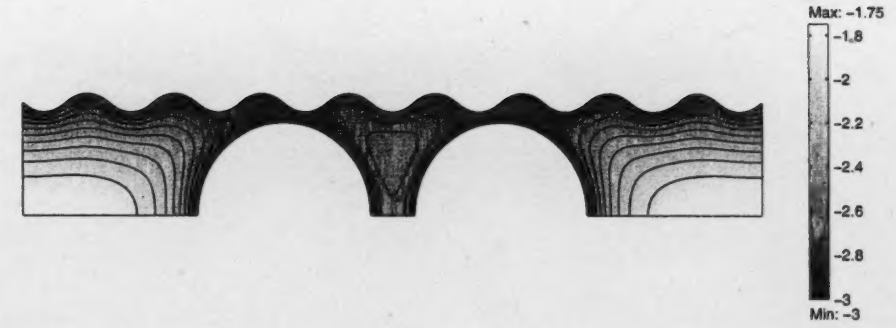

(a) $\Psi_c = -3.0$.

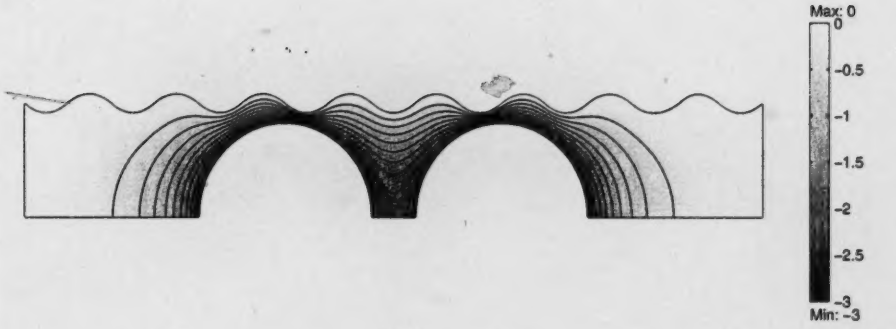

(b) $\Psi_c = 0.0$.

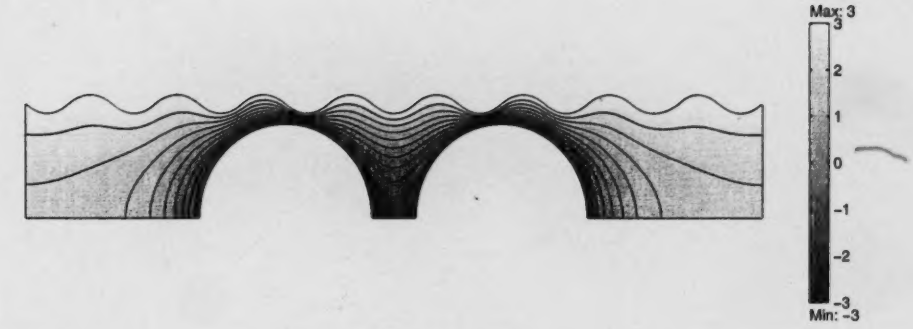

(c) $\Psi_c = +3.0$.

Figure 4.4: Potential distribution of two spherical particles inside an infinitely long "rough" capillary corresponding to three different capillary surface potentials as mentioned in the legend for the situation when particles are moving uniformly from the trough of an undulation (Case−II).

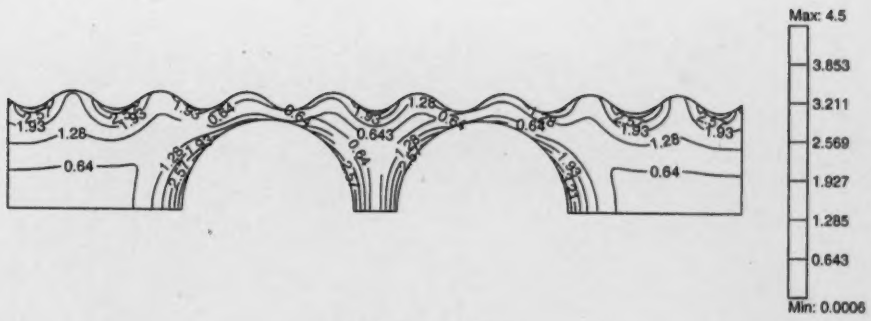

(a) $\Psi_c = -3.0$.

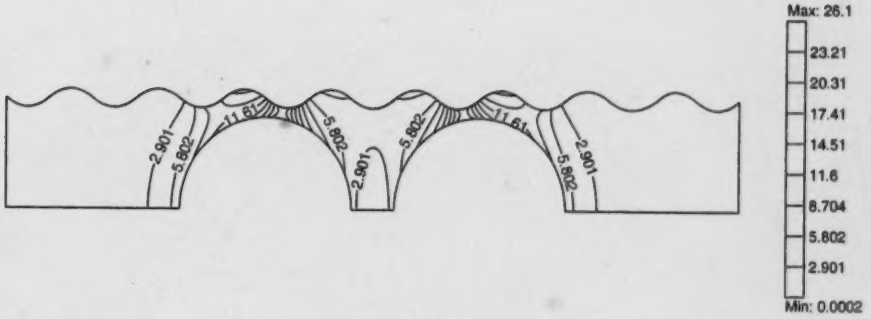

(b) $\Psi_c = 0.0$.

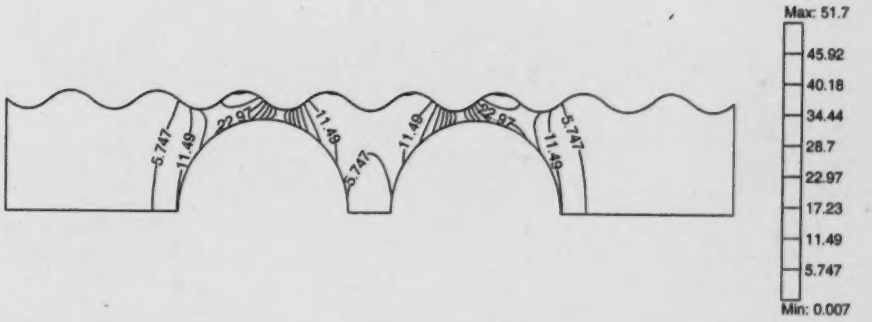

(c) $\Psi_c = +3.0$.

Figure 4.5: Electrostatic field distribution inside an infinitely long "rough" capillary corresponding to three different capillary surface potentials as mentioned in the legend for Case−II.

in Figure 4.1.

Distribution of the electrostatic potential and field corresponding to Case−II are depicted in Figures 4.4 and 4.5, respectively. These results are obtained under identical parameter settings as Figures 4.2 and 4.3. Similar trend is observed in the potential and field distribution as observed in Figures 4.2 and 4.3. The variations in term of magnitude are same for both cases. However, in the field distribution (Figure 4.3), the most significant observation is the location of the highest gradient points. In this case, the maximum stress is directed toward the mid-plane between the particles, resulting in a net enhancement in the attraction between the particles. In the following subsections, a detailed analysis of the variation of net electrostatic force acting along the axial direction on the spherical particle is presented for different combinations of scaled amplitude and pitch of the roughness for both Case−I and Case−II.

4.3.2 Similarly Charged Particles and Capillary

The interaction forces between two charged spherical particles inside a charged capillary were calculated for constant potential (CP) boundary conditions when both the particles and the capillary were similarly charged (bearing same sign of the surface potential). The force was determined for the scaled particle-particle separation distance κh ranging from 0.0 to 3.0. As mentioned earlier in Section 4.2.1, the simulations were performed for two cases: Case−I corresponding to a reference point (R in Figure 4.1a) being at the crest of the rough cylindrical capillary wall, and considering the two particles moving away from point R, while Case−II corresponding to the reference point at the trough (R in Figure 4.1b).

Figures 4.6 and 4.7 depict the variation of scaled interaction force with scaled separation distance between the spherical particles (κh) for Case−I and Figures 4.8 and 4.9 depict the force profiles for Case−II. The results in these figures correspond to four values of the scaled pitch (wavelength) of the undulation (ξ),

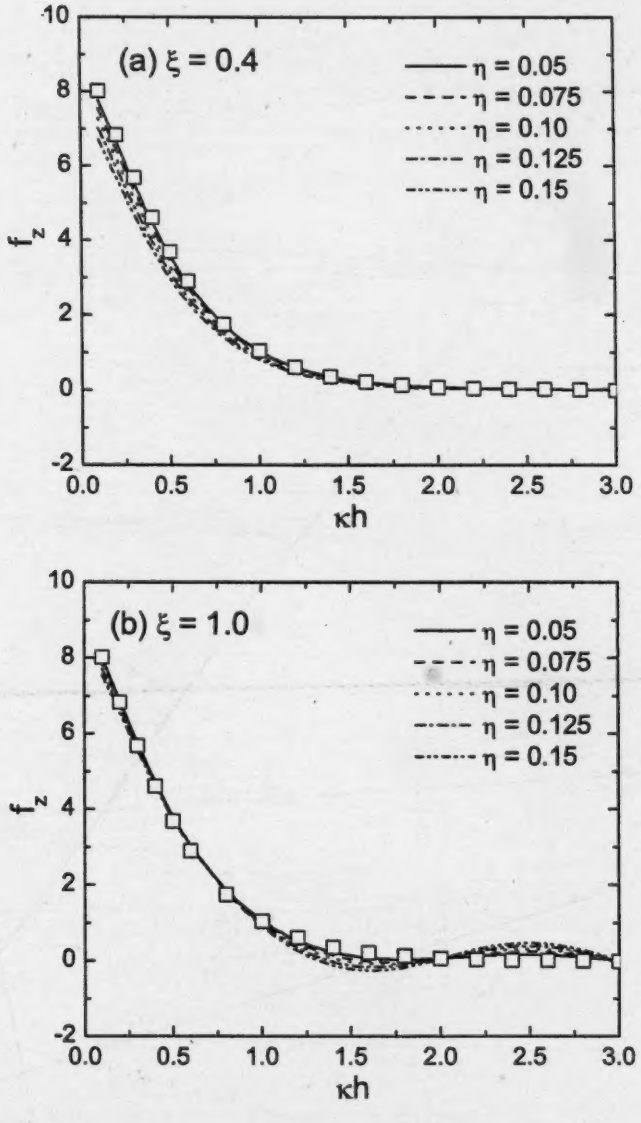

Figure 4.6: Variations of the scaled electrostatic interaction force between two spherical particles inside a "rough" capillary with scaled separation distance when the particles are moving uniformly from the crest of an undulation (Case−I). Both particles and capillary are similarly charged ($\Psi_p = \Psi_c = -3.0$) and different line types correspond to different values of scaled amplitude (η) of the roughness as indicated in the legend. Two figures represent the two values scaled wavelength of the undulation, (a) $\xi = 0.4$ and (b) $\xi = 1.0$. The open symbols depict the interaction force between two CP particles in a smooth ($\eta = 0.0$) cylindrical capillary.

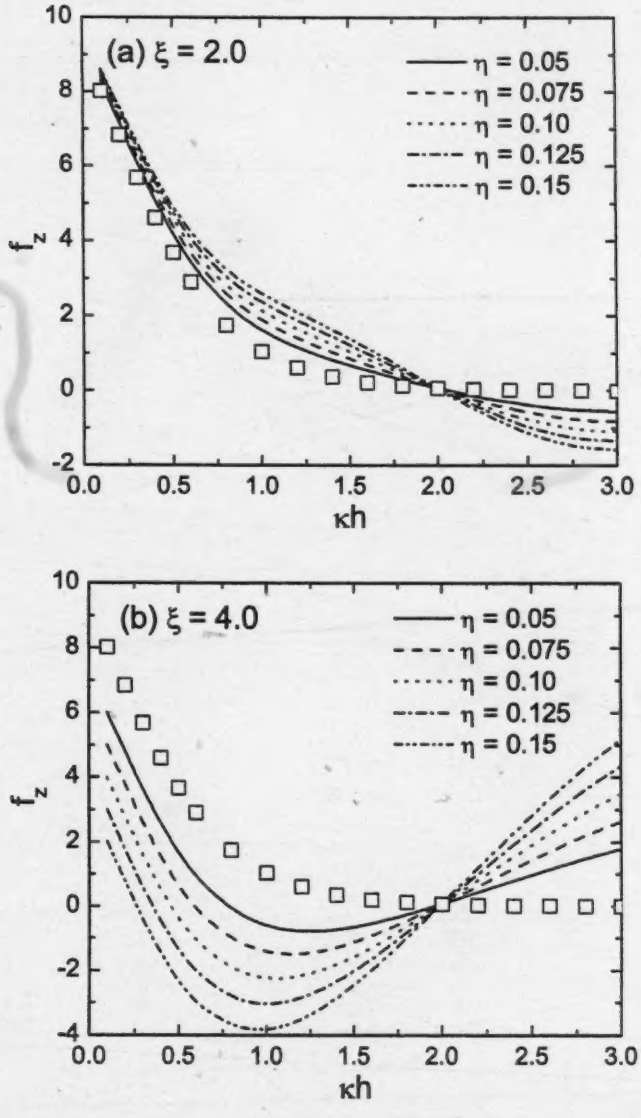

Figure 4.7: Variations of the scaled electrostatic interaction force between two spherical particles inside a "rough" capillary with scaled separation distance when the particles are moving uniformly from the crest of an undulation (Case−I) under same conditions as in Figure 4.6. Two figures represent the two values scaled wavelength of the undulation, (a) $\xi = 2.0$ and (b) $\xi = 4.0$.

namely, 0.4, 1.0, 2.0, and 4.0, as indicated in the legend. In all these figures, the force was calculated for a fixed value of the size ratio $\lambda = a/b = 0.83$, a fixed dimensionless surface potential $\Psi_p = -3.0$ on the particles and a dimensionless surface potential $\Psi_c = -3.0$ on the capillary wall. A negative value of the scaled force in these figures corresponds to attraction, while a positive value indicates repulsion. For comparison, the interaction force between two particles in an infinitely long smooth cylindrical capillary is depicted as open symbols in each figure.

Figure 4.6a indicates that varying the scaled amplitude (η) from 0.05 to 0.15 induces extremely small changes in the magnitude of the scaled electrostatic force compared to a smooth capillary wall when the scaled pitch of the undulation ($\xi = 0.4$) is less than the particle radius ($\kappa a = 1.0$). Regardless of the value of scaled amplitude, roughness always reduces the repulsive force between the two colloidal particles at small separation distances. Figure 4.6b shows the variation of interaction forces for different amplitudes of the roughness when the wavelength of the periodic roughness (ξ) on the capillary wall is equal to the particle radius (κa). Figure 4.7 shows the force for the cases when the scaled wavelength of the roughness is greater than the particle radius. In these cases, an oscillatory behaviour of the interaction force between the particles is observed. These oscillations correspond to the periodic nature of the capillary wall roughness, and the extent of the oscillations increases with the amplitude of the roughness. For $\xi = 2.0$ and 4.0, the interaction force even becomes attractive at certain locations, and the particles feel a periodic attractive and repulsive interaction as the separation distance between them is increased. In all cases, the interaction force is primarily contributed to by the roughness of the capillary wall. When the interparticle separation becomes larger than approximately one wavelength of the periodic roughness of the capillary, each spherical particle appears to solely interact with the capillary wall. The behaviour described above is strongly dictated by the amplitude of the roughness, with larger amplitudes leading to greater oscillations in the interaction force.

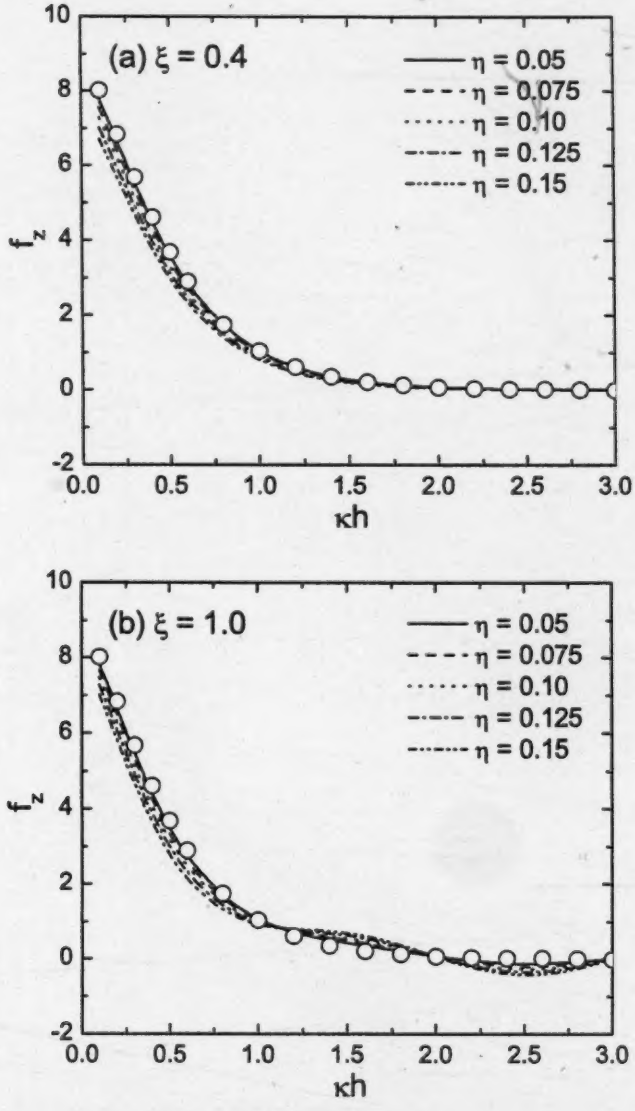

Figure 4.8: Scaled electrostatic interaction force between two spherical particles as a function of scaled separation distance when the particles are moving uniformly from the trough of an undulation (Case−II) under same conditions as in Figure 4.6 for two values scaled wavelength of the undulation, (a) $\xi = 0.4$ and (b) $\xi = 1.0$.

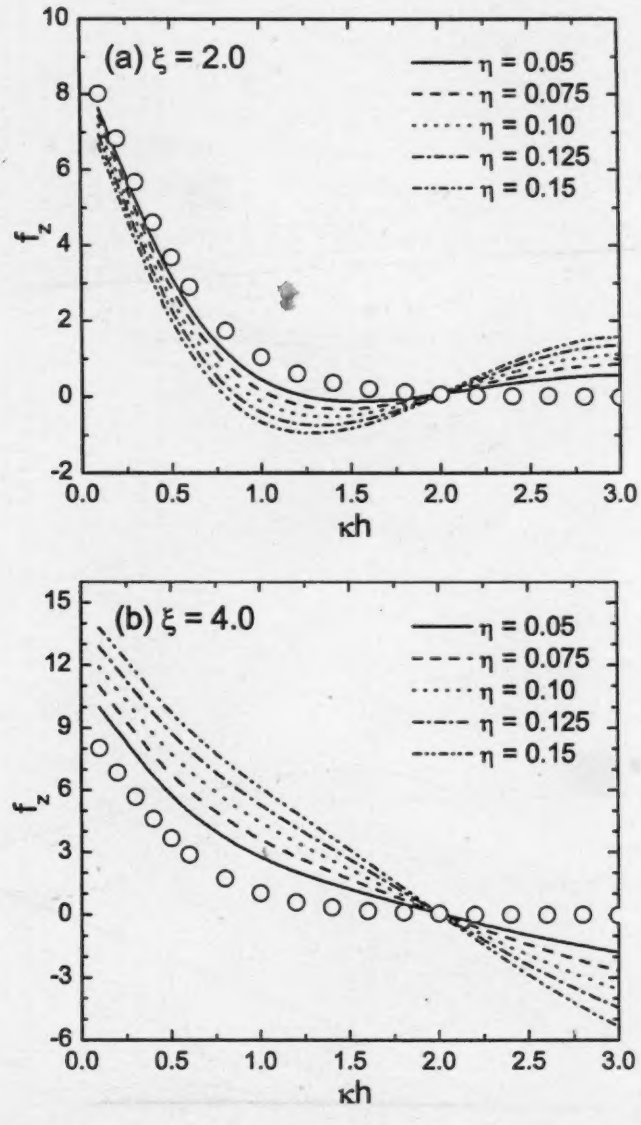

Figure 4.9: Scaled electrostatic interaction force between two spherical particles as a function of scaled separation distance when the particles are moving uniformly from the trough of an undulation (Case−II) under same conditions as in Figure 4.7 for two values scaled wavelength of the undulation, (a) $\xi = 2.0$ and (b) $\xi = 4.0$.

Furthermore, all the oscillations seem to occur symmetrically about the zero amplitude force.

The forces corresponding to Case−II when particles are moving uniformly form a reference point o/n the trough of an undulation are shown in Figures 4.8 and 4.9, which indicate a different behaviour compared to Case−I, particularly for larger wavelengths of the undulation. These results were obtained under identical parameter settings for the Case−I simulations. In Figure 4.8, similar trends in the interaction forces are observed for small $\xi(< 1.0)$ like Figure 4.6 at small separations. Surface roughness reduces the magnitudes of the electrostatic repulsion for small separations ($\kappa h \leq 0.5$). From these two figures, it is clear that for small ξ, relative position of a particle with respect to the crest or trough of an undulating wall does not play any significant role on the electrostatic interaction. However, the variation of electrostatic force between the particles for $\xi = 2.0$ and 4.0 are completely opposite both in nature and magnitude when we compare Figure 4.7 to Figure 4.9. In Case−I, the interaction force is more repulsive when the separation distance is less than the wavelength for $\xi = 2.0$, while in Case−II, the force is less repulsive, and even becomes slightly attractive near $\kappa h = 1.0$ (Figures 4.7a and 4.9a). The trends in Figures 4.7b and 4.9b are exactly opposite to the above observation.

4.3.3 Charged Particles Inside an Uncharged Capillary

The variation of the scaled interaction force with scaled separation distance κh) between the spherical particles inside an uncharged ($\Psi_c = 0.0$) "rough" capillary is shown in Figures 4.10, 4.11, 4.12, and 4.13. Results are presented for both Case−I (Figures 4.10 and 4.11) and Case−II (Figures 4.12 and 4.13) for four values of the scaled pitch of the undulation (ξ), namely, 0.4, 1.0, 2.0, and 4.0. The simulations of Figures 4.10 and 4.11 were performed under identical conditions as in Figures 4.6 and 4.7, respectively, except for zero surface potential conditions on the capillary wall ($\Psi_c = 0.0$). Similarly, Figures 4.12 and 4.13 have the identical boundary conditions of Figures 4.10 and 4.11, respectively.

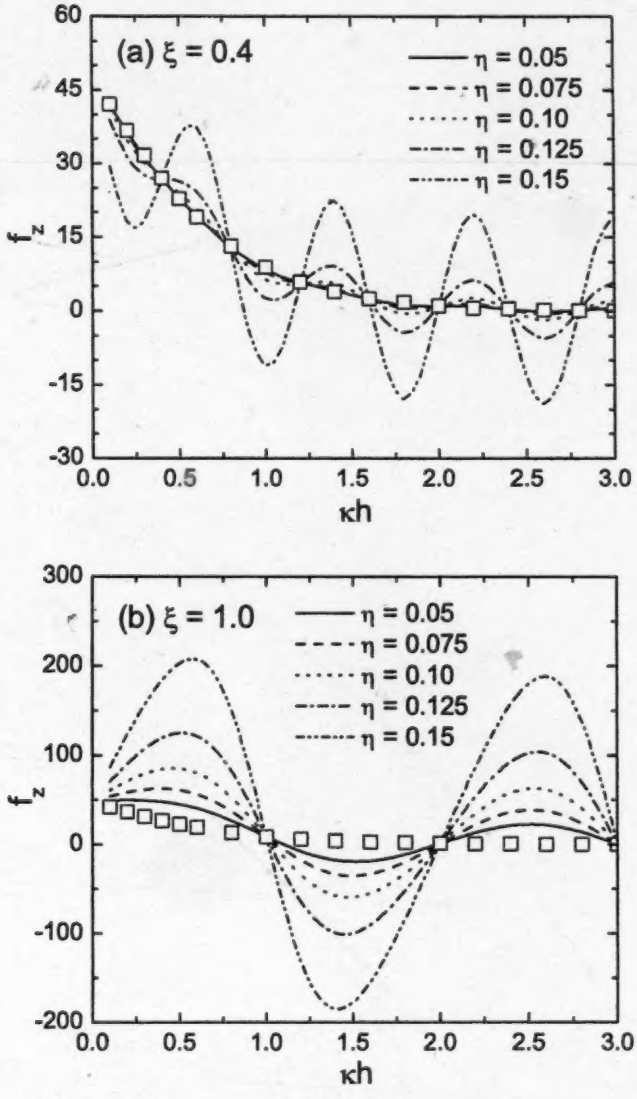

Figure 4.10: Variation of the scaled electrostatic interaction force between two similarly charged particles inside an uncharged "rough" capillary with scaled separation distance for Case−I corresponding to two values scaled wavelength of the undulation, (a) $\xi = 0.4$ and (b) $\xi = 1.0$. Simulations were performed under same boundary conditions as in Figure 4.6, except for zero surface potential on the capillary wall ($\Psi_c = 0.0$). The open symbols depict the interaction force between two CP particles in a smooth ($\eta = 0.0$) cylindrical capillary.

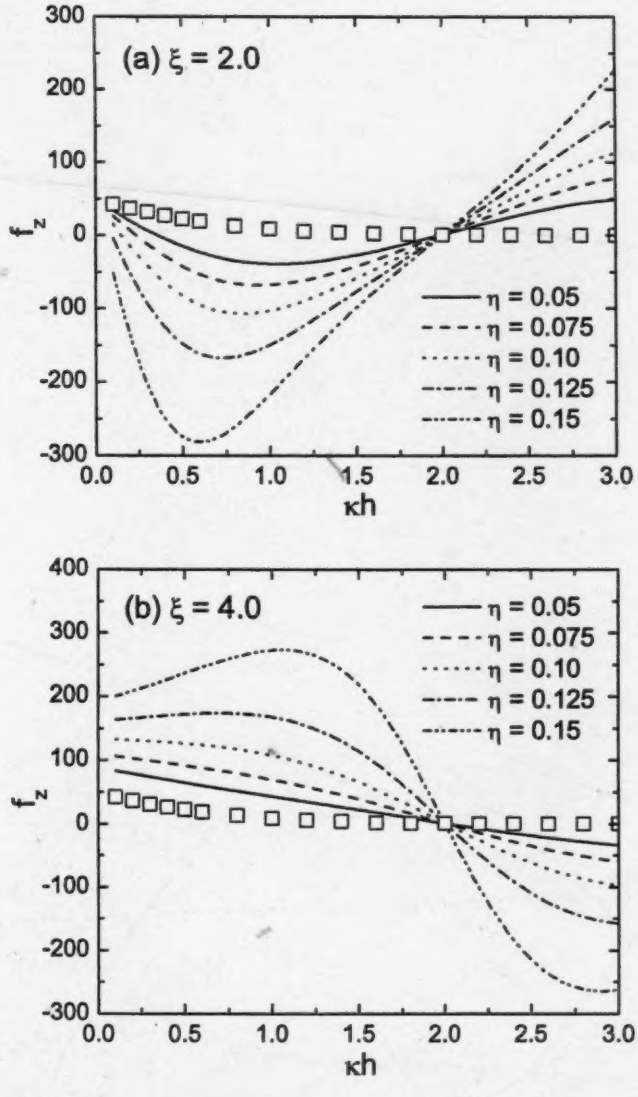

Figure 4.11: Variation of the scaled electrostatic interaction force between two similarly charged spherical particles inside an uncharged "rough" capillary with scaled separation distance for Case−I corresponding to two values scaled wavelength of the undulation, (a) $\xi = 2.0$ and (b) $\xi = 4.0$. Simulations were performed under same boundary conditions as in Figure 4.10.

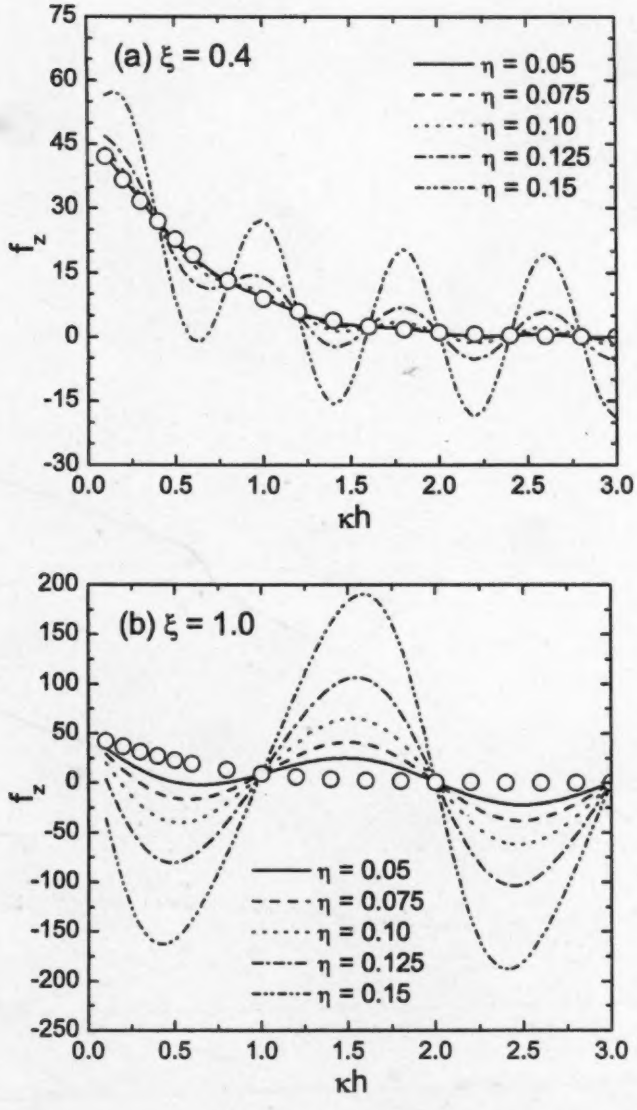

Figure 4.12: Variation of the scaled electrostatic interaction force between two similarly charged particles inside an uncharged ($\Psi_c = 0.0$) "rough" capillary with scaled separation distance for Case–II under same conditions as in Figure 4.10 for two values scaled wavelength of the undulation, (a) $\xi = 0.4$ and (b) $\xi = 1.0$.

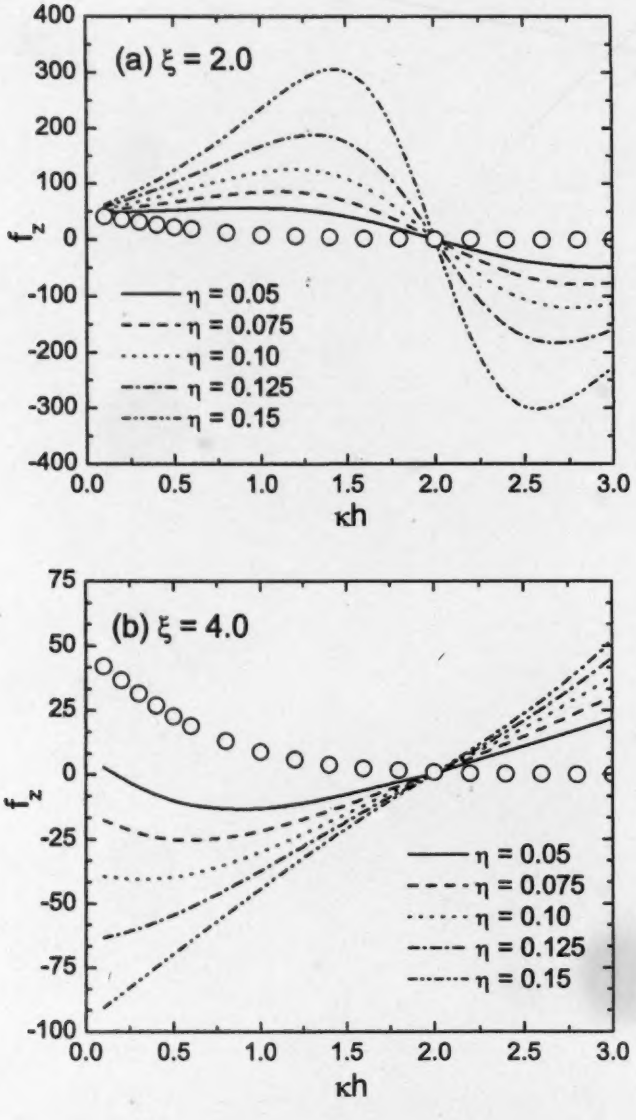

Figure 4.13: Variation of the scaled electrostatic interaction force between two similarly charged particles inside an uncharged ($\Psi_c = 0.0$) "rough" capillary with scaled separation distance for Case−II under same conditions as in Figure 4.11 for two values scaled wavelength of the undulation, (a) $\xi = 2.0$ and (b) $\xi = 4.0$.

For similarly charged particles and capillary wall, the effect of amplitude on the interaction force is less significant in terms of the magnitude (*cf.* Figures 4.6 and 4.8), particularly for smaller wavelengths. For different particle and capillary wall surface potentials, however, the effect of amplitude on the interaction force is considerable in terms of the magnitude as well as nature of the forces even for small wavelengths. For smaller amplitudes ($\eta < 0.1$), variations of the electrostatic force are negligible compared to the cases when amplitude is higher than 0.1. For large amplitudes, the force is oscillatory, closely emulating the periodic undulations of the capillary wall. Depending upon the relative position of the particles, the forces are either repulsive or attractive. For $\xi \geq 1.0$, a dramatic change in magnitude of the forces is observed even at small amplitudes. A slight increase in amplitude causes a significant enhancement of the interaction force on the particles. The presence of roughness appears to induce a significant oscillation in the forces, which alternately become attractive and repulsive, emulating the periodic nature of the roughness, whereas the particles always exhibit repulsive force inside a smooth capillary. When the particles are moving from the trough of an undulation, the nature of the force is opposite compared to when the particles are moving away from the crest as depicted in Figures 4.12 and 4.13. For separation distances larger than the wavelength of the roughness, the maxima and minima of the interaction force have nearly identical values (Figures 4.10b and 4.12b).

4.3.4 Charged Particles Inside an Oppositely Charged Capillary

The interaction forces between the particles were determined so far for situations where the particles and the capillary surfaces had potentials with same sign (like-charge cases) and the case when the particles had potentials with same sign but the capillary wall surface potential was zero. Figures 4.14, 4.15, 4.16, and 4.17 represent the variation of interaction force for cases where the capillary surface is oppositely charged with respect to the particles. The simulations of these figures

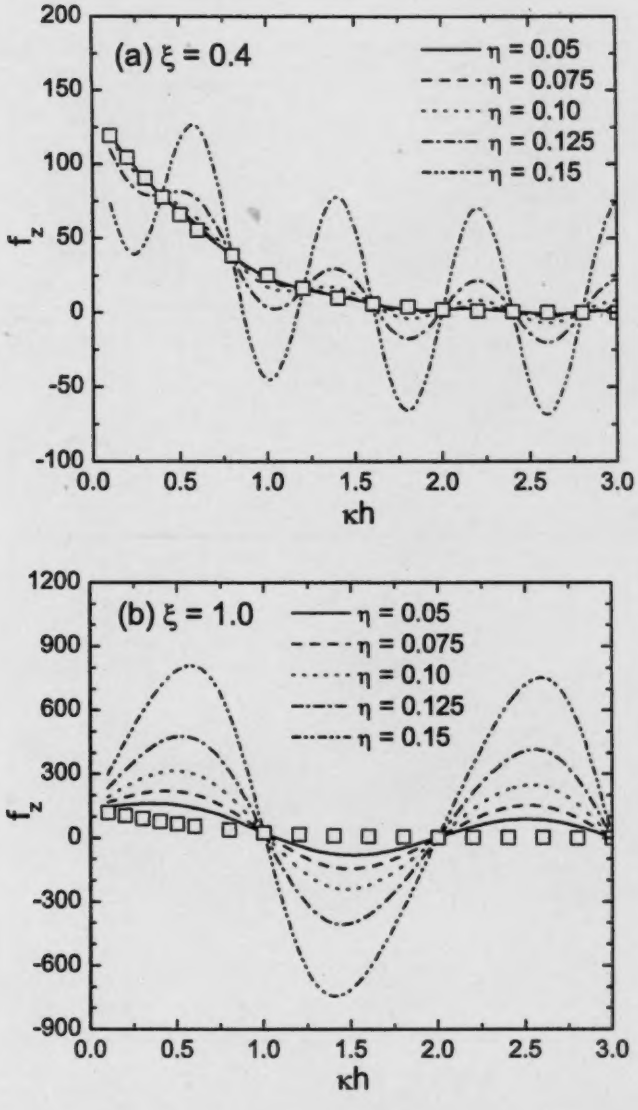

Figure 4.14: Variation of the scaled particle-particle interaction force between two similarly charged spherical particles inside an oppositely charged capillary with scaled separation distance for Case−I. The scaled surface potential on the capillary wall is $\Psi_c = +3.0$, while the particle surface potential is given by $\Psi_p = -3.0$. All other conditions are as in Figure 4.6. Two figures represent the two values scaled wavelength of the undulation, (a) $\xi = 0.4$ and (b) $\xi = 1.0$.

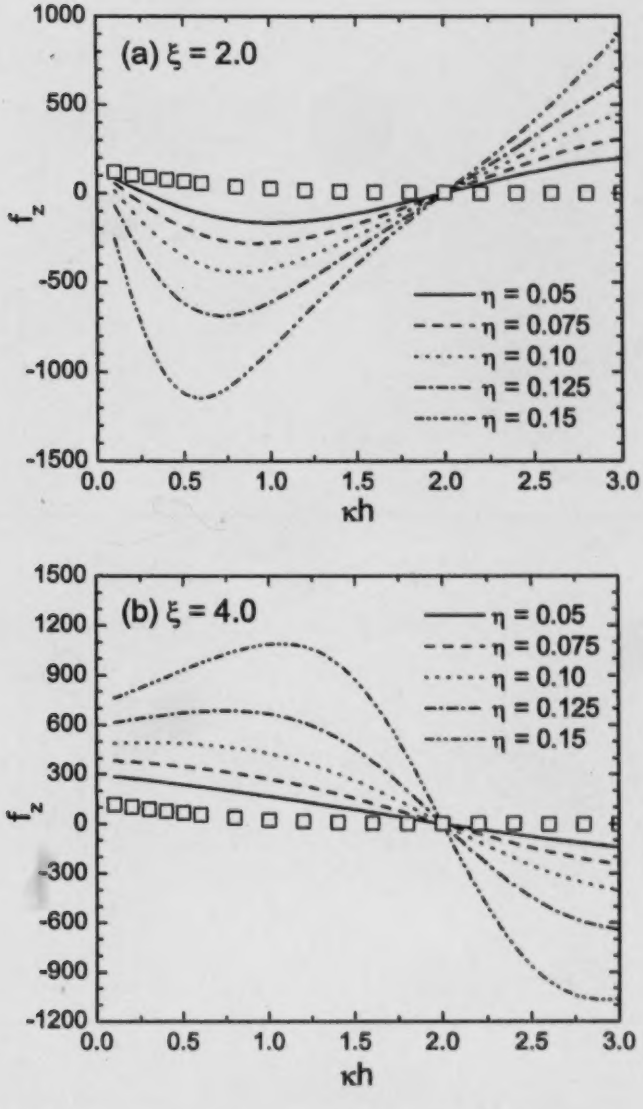

Figure 4.15: Variation of the scaled particle-particle interaction force between two similarly charged spherical particles inside an oppositely charged capillary with scaled separation distance for Case−I corresponding to two values scaled wavelength of the undulation, (a) $\xi = 2.0$ and (b) $\xi = 4.0$ under same conditions as in Figure 4.14.

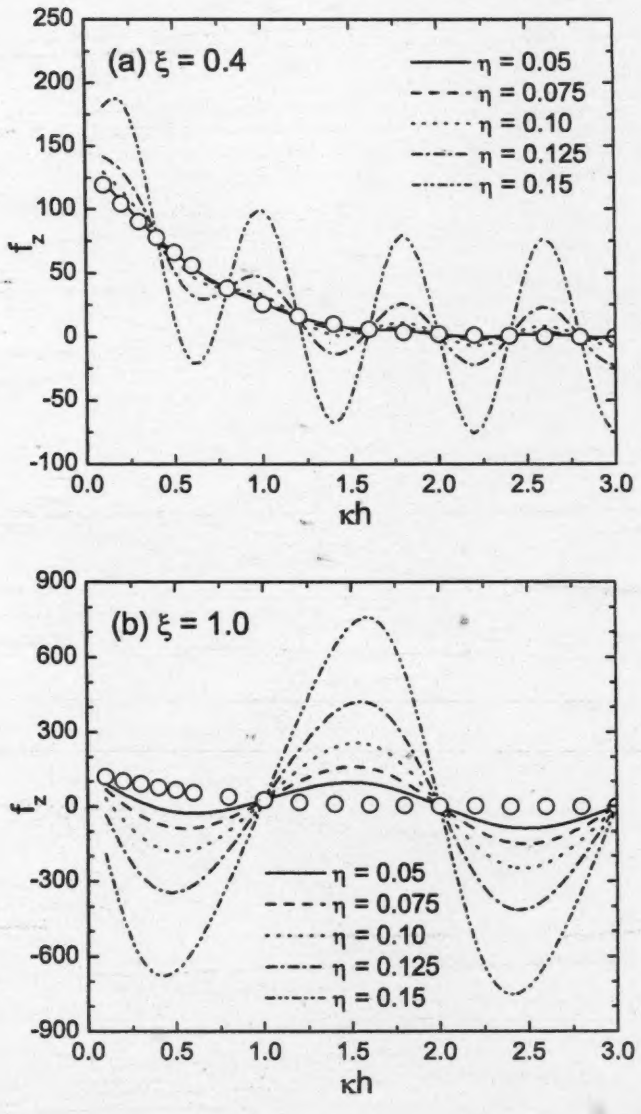

Figure 4.16: Variation of the scaled particle-particle interaction force between two similarly charged spherical particles inside an oppositely charged capillary with scaled separation distance for Case−II under same conditions as in Figure 4.14 for two values scaled wavelength of the undulation, (a) $\xi = 0.4$ and (b) $\xi = 1.0$.

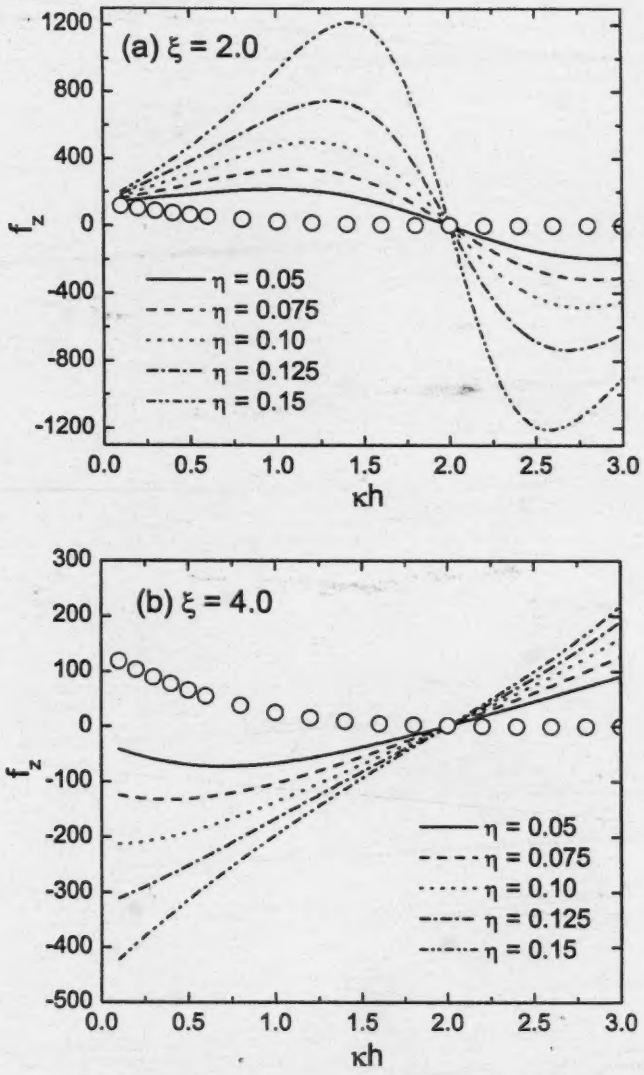

Figure 4.17: Variation of the scaled particle-particle interaction force between two similarly charged spherical particles inside an oppositely charged capillary with scaled separation distance for Case−II under same conditions as in Figure 4.15 for two values scaled wavelength of the undulation, (a) $\xi = 2.0$ and (b) $\xi = 4.0$.

were performed under identical conditions as all the previous cases, except for the opposite sign of the surface potential on the capillary wall ($\Psi_c = +3.0$). Figures 4.14 and 4.15 show the simulations for Case−I, *i.e.*, particles moving away from the crest. The two parts (a−b) in Figure 4.14 correspond to the scaled pitch of the undulation $\xi = 0.4$ and 1.0 and two parts (a−b) in Figure 4.15 correspond to $\xi = 2.0$ and 4.0. Figures 4.16 and 4.17 depict the corresponding results for Case−II with all other parameters identical to the simulations of Figures 4.14 and 4.15. All of these results follow similar qualitative behaviour as the corresponding simulations for the uncharged capillary wall, although the magnitude of the interaction force was found to be considerably larger compared to the uncharged capillary cases. From these results, it is evident that the roughness effects of the oppositely charged capillary wall are so pronounced that the particle-particle interaction force is strongly oscillatory even at very small interparticle separations.

4.4 Influence of Surface Roughness on the Interaction Force

The results from the previous section throw considerable light regarding the behaviour of the electrostatic double layer force experienced by a spherical colloidal particle inside a rough capillary, which is charged to different extents. The most striking feature of these results is the enormous influence of the capillary wall roughness on the magnitude of the interaction force. In this section, some of the implications of these roughness engendered oscillatory forces on the behaviour of nanoparticles confined in capillary cavities are discussed.

The simulations presented here all represent situations where the particle and capillary mean radii are comparable to the screening length of the electrostatic double layer interactions. Furthermore, all the calculations were for comparable particle and capillary radii corresponding to the scenario of particles confined in tightly fitting capillaries. The dramatic oscillatory behaviour

observed in such tightly fitting pores decay sharply as the size ratio (a/b) is decreased, and for size ratios of about 0.5, the oscillations are imperceptible. Similarly, the oscillations in the force are damped dramatically as the particle size to screening length ratio, κa, is increased. It should also be noted that the large variations noted here are only observed for constant potential particles. For constant charge density on the particle surfaces, the influence of roughness is not so dramatic.

The interaction force experienced by a spherical particle in rough capillaries evolves from two competing factors. First, presence of the similarly charged (implying same sign of the surface potential as the particle surface potential) smooth capillary wall causes a reduction in the interaction force compared to the force between two particles in an infinite domain. This can be observed by comparing the constant potential results of two particles in an infinite domain (Figure 3.4a) with the zero amplitude forces (symbols) in Figures 4.6 and 4.7. Secondly, oscillations in the capillary wall result in severe modifications of the electrostatic stress tensor by imposing unbalanced Maxwell stresses on the particle due to asymmetry in the rough capillary geometry. The periodic nature of the interaction force exactly matches the wavelength of the undulations in the capillary wall. When both the particle and capillary surfaces have the same surface potentials (both magnitude and sign), the magnitude of the force is small. However, the forces are drastically enhanced as the capillary surface potential changes from the particle surface potential. In absence of roughness, reducing the surface potential of the capillary wall substantially enhances the repulsion between the spherical particles. If, in addition, the amplitude of the roughness is increased, the repulsion is increased even further. However, the repulsion is caused solely by the asymmetric positioning of regions of the capillary wall in the vicinity of the spherical particle. The effect of such asymmetric stresses induced by the wall with different surface potentials on the particles is so intense that even at very small separations between the particles, we start observing a considerable oscillation of the interaction force (note the distinct

differences between the interaction forces in Figure 4.6a, 4.10a, and 4.14a for small κh). In other words, for dissimilar surface potentials on the particles and the capillary, the interaction force between the particles is predominantly dictated by the charge and periodicity of the capillary wall surface. The force oscillates around a mean value that represents the particle-particle interaction in a smooth cylindrical capillary, with a superimposed oscillation that follows the roughness pattern of the capillary wall.

It should be noted, however, that the magnitudes of the force oscillations obtained for oppositely charged capillaries may be unrealistically high. This high value is an artifact of our use of Boltzmann distribution and assumption of point charge ions in our analysis. Such an approximation allows concentration of extremely large number of ions near the asperities, which is physically unrealistic. Although the effects of finite ion sizes are not included in this thesis, it is believed that inclusion of such effects will result in a more modest variation of forces.

The oscillatory force experienced by the spherical particle is possible only in case of nano-scale particles, and may be instrumental in dictating the transport behaviour of nanoparticles in confined geometries of comparable dimensions. In these situations, the roughness of the confining wall (and, of course, the surface texture of the particles themselves) becomes comparable to the scaled amplitude values employed in these simulations. For instance, if we consider a 50 nm radius colloidal particle in a 60 nm radius capillary, a scaled amplitude of 0.1 will indicate that the roughness is of the order of 5 nm. This scale of roughness can be obtained quite readily in photolithographic micro-fabrication of micro-channels by etching a sputtered metal layer on a silicon wafer. The purpose of etching a metal film is to produce channels, the walls of which can be charged up to a constant surface potential. Although silicon or glass substrates can be etched to a considerably higher precision than metal films, we cannot form a constant potential surface on these materials. In the following section, a detailed measurement technique of surface roughness using atomic force micro-

scope (AFM) is provided along with a brief description of the micro-fabrication techniques.

4.5 AFM Measurement of Surface Roughness

4.5.1 Fabrication of Micro-channel

The fabrication of micro-channels begins from the proper selection of metal for the coating layer on Si-wafers. Here, aluminum is sputtered over the Si-wafer using standard sputtering techniques. In sputtering, argon gas is used as ionizing medium, which is attracted to a target of metal that is electrically grounded. As the argon bombards the target, metal atoms are knocked away from the target and deposited on the wafer. The next steps include photolithography, and wet etching. Photolithography is the process of transferring geometric shapes from the mask to the desired surface. In the lithography procedure, a light-sensitive material known as photo-resist, is deposited on the wafer, and this photo-resist is exposed and developed to uncover certain areas of the wafer which may then be subjected to process steps without affecting the covered, or masked, areas. The photosensitive resist is applied on the wafer in a liquid form and then coated evenly by spinning the wafer at 3000 RPM. Subsequent soft-baking steps are used to solidify the resist, improving its adhesion to the wafer surface and enhancing its resistance to etchant. In the exposing part, a mask with the desired pattern is brought close in contact with the resist-covered wafer and exposed using ultraviolet light shining through the mask so that only selected areas are exposed. A typical mask designed for this purpose is depicted in Figure 4.18a. The white region in Figure 4.18a shows the uncovered or exposed area through which UV light can shine on the photo-resist layer on the wafer and the black region represents the covered area on the photo-mask. The exposed wafer is then developed by immersion in a developer solvent for about one minute (amount of time varies with resist thickness, type, etc.). This exposes the appropriate areas of the wafer surface, allowing further processing in only those areas until

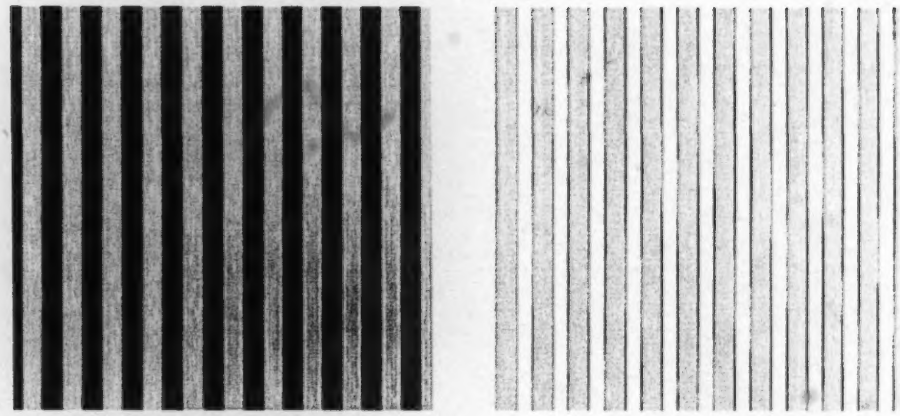

(a) Mask. (b) Wafer.

Figure 4.18: Microscope image of micro-fabricated mask in part (a) and corresponding microscope image of aluminium coated Si-wafer after etching in part (b) showing an array of rectangular micro-channels.

the masking resist layer is removed. Finally, etching is done by immersing the patterned wafer in Al-etchant for a certain time period, which will react with the exposed Al-layer and remove it. Typical results obtained from etching an aluminum film using a wet-etching process is depicted in Figure 4.18b where the gray region represents 5 μm wide rectangular micro-channels. A detailed description of the roughness analysis of the micro-fabricated micro-channel using atomic force microscope is presented in the following subsection.

4.5.2 AFM Width Analysis

To measure the roughness of the micro-fabricated rectangular micro-channel, the aluminium coated Si-wafer shown in Figure 4.18b is first scanned using an atomic force microscope (Digital Instruments' Dimension 3100 SPM). Figure 4.19a shows an array of approximately 5 μm wide rectangular channels scanned using an atomic force microscope (Digital Instruments' Dimension 3100 SPM) while Figure 4.19b shows an array of approximately 6 μm wide rectangular channels. The depth of these channels is approximately 450 nm and pitch is 10

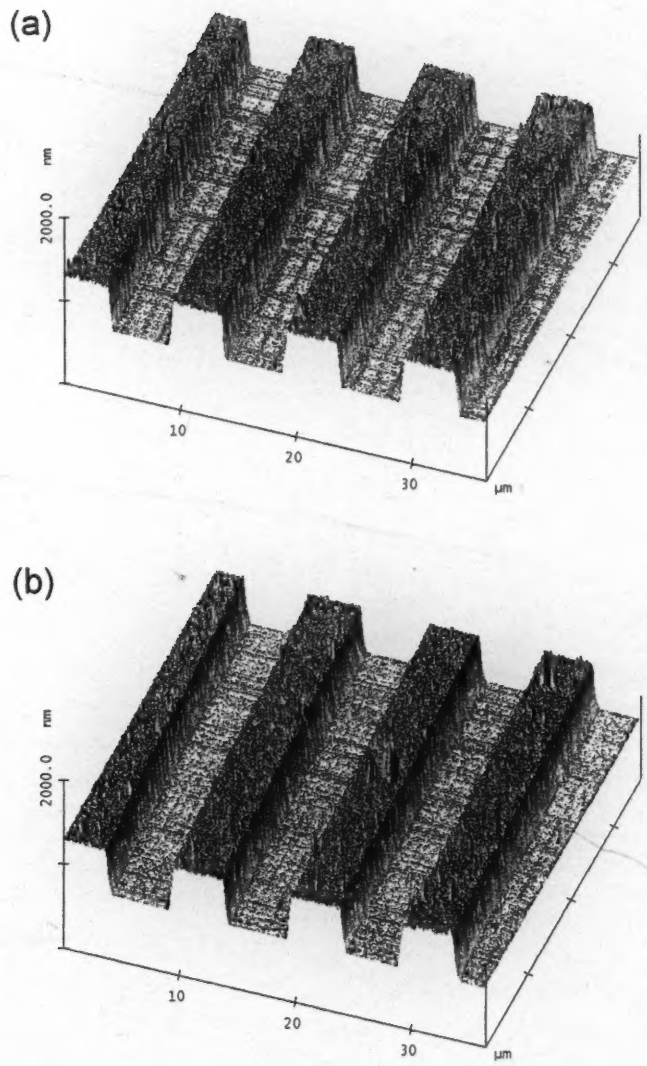

Figure 4.19: Atomic force microscope (AFM) image of micro-fabricated rectangular channels showing an array of, (a) 5 μm wide and (b) 6 μm wide rectangular micro-channels of *ca.* 0.45 μm deep etched on an aluminum film.

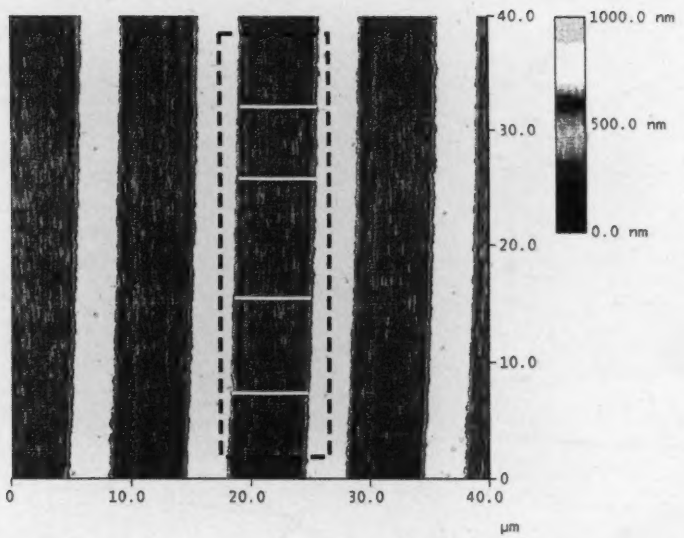

Figure 4.20: Atomic force microscope (AFM) image of micro-fabricated rectangular channels showing the procedure of measuring surface roughness by width analysis. Top view of patterned surface showing the section over which the width analysis is performed. The dashed rectangular box is placed on each channel and the width of the channel is measured by recording the lengths of all the horizontal scan lines (horizontal white lines) spanning the width of the channel. The measurements are performed at different channel heights.

μm in both cases. The unevenness of the metal film, particularly at the vertical walls, is readily visible in these images. A quantitative depiction of the extent of roughness on these vertical side-walls is possible through a width analysis, which is described in the following.

Figure 4.20 shows a typical section over which the analysis is performed. In width analysis, the average width of a feature is measured inside a specified box (shown by the rectangle in Figure 4.20). The average width is obtained by measuring the lengths of all the line segments aligned parallel to the horizontal sides of the box (the horizontal scan lines). The standard deviation of this width distribution provides an estimate of the vertical wall roughness. This analysis is performed on three consecutive channels in a wafer. For each channel, the mean width and standard deviation are measured at four different vertical locations

Wafer 1: Channel width = 5 μm, pitch = 10 μm, and height = 487 nm					
	Threshold (nm)	100	200	300	400
Channel 1	Mean width (nm)	4996	5110	5277	5422
	Std. deviation (nm)	86.44	79.25	77.81	74.63
Channel 2	Mean width (nm)	5111	5326	5495	5643
	Std. Deviation (nm)	93.27	90.53	81.54	76.75
Channel 3	Mean width (nm)	5030	5241	5408	5553
	Std. Deviation (nm)	96.24	88.69	83.72	83.19

Table 4.1: Width analysis statistics from atomic force microscope scans of rectangular micro-channels shown in Figure 4.19a. The threshold value represents the vertical height from the base of the channel.

Wafer 2: Channel width = 6 μm, pitch = 10 μm, and height = 459 nm					
	Threshold (nm)	100	200	300	400
Channel 1	Mean width (nm)	6125	6308	6448	6586
	Std. deviation (nm)	79.16	79.89	86.41	85.49
Channel 2	Mean width (nm)	6285	6486	6618	6756
	Std. Deviation (nm)	88.12	86.19	80.57	81.45
Channel 3	Mean width (nm)	6285	6461	6612	6745
	Std. Deviation (nm)	77.32	78.99	79.67	84.34

Table 4.2: Width analysis statistics from atomic force microscope scans of rectangular micro-channels shown in Figure 4.19b. The threshold value represents the vertical height from the base of the channel.

(100, 200, 300, and 400 nm) in the channel. The measurement results are summarized in Table 4.1. Similar measurements were also conducted using another wafer where the channel width was 6 μm as summarized in Table 4.2. From these tables, it is clear that the channel width decreases with depth in all cases. In other words, the channels are slightly tapered. Secondly, the standard deviation, which provides a measure of the roughness, does not depend on the channel width. The average standard deviation from all these measurements was determined as 83.32 nm. The standard deviation, to a good approximation, represents the sum of the roughness amplitudes from the two vertical walls of a channel. Assuming that the average roughness on both the side-walls are same, the roughness amplitude on a channel wall is estimated to be 41.66 nm (half of the standard deviation).

The above analysis reveals that the mean roughness of wet-etched metal film channels that are about 450 nm deep, is of the order of 40 nm. Scaling this information linearly to 100 nm deep channels yields a value of about 10 nm for the wall roughness. Therefore, it is clearly discernable that the roughness amplitudes considered in this study are comparable to those obtainable in micro-fabrication processes. In top-down micro-fabrication processes, we will generally obtain significant roughness on the walls of these channels, which in turn, can considerably affect the electrostatic interaction of a charged particle that is comparable in dimension to the channel width. Although the channels in the above discussion are rectangular, the analysis performed using the cylindrical geometry in our simulation studies provides considerable insight regarding the qualitative behaviour of the interactions experienced by particles near the axis of these rectangular channels.

4.6 Summary

The simulations performed in this study reveal that the electrostatic double layer interaction force experienced by a spherical colloidal particle inside a

"rough" capillary can be significantly modified by the roughness of the capillary wall. The influence of the wall roughness is significant when the periodicity of the roughness (wavelength) is comparable to or larger than the particle radius. When the periodicity of the roughness is considerably smaller than the particle dimension, the interaction force experienced by the particle is not seriously altered if both the particles and the capillary surfaces are similarly charged (bearing same sign of the surface potential). However, as the capillary surface potential starts to deviate from the particle surface potential, a considerable influence of the capillary wall is observed on the electrostatic force experienced by a particle irrespective of the scale of the wall roughness. Influence of the capillary wall roughness on the electrostatic force is more prominent when charged spherical nanoparticles are trapped inside an oppositely charged rough capillary. The roughness amplitudes considered in these simulations appear to be consistent with roughness dimensions generated in photolithographic fabrication of micro-channels by etching metal films. Accordingly, it seems that a roughness analysis of the channel walls is a fairly important criterion for correctly assessing the electrokinetic transport behaviour of nanoparticles inside such capillaries, particularly when the particle dimensions are comparable to the channel hydraulic diameter.

Chapter 5

Many-Body Electrostatic Interactions

5.1 Introduction

The electrostatic double layer interaction between colloidal particles was studied so far for situations where two nanoparticles were interacting inside a cylindrical confinement. Although interaction of the particles with the confining wall was also considered in the previous cases, the exact scenario of many-body colloidal interactions and how presence of a surface or another particle affects the particle-particle interaction was not addressed explicitly. The purpose of this chapter is to study the effect of the presence of neighboring particles on the electrostatic double layer interaction between colloidal particles. Toward an experimentally approachable scenario to describe the behaviour of concentrated colloidal dispersions in confined domains, a 3-dimensional (3-D) finite element model of electrostatic interactions near a planar wall or interface containing a layer of deposited particles is proposed. This model can be potentially verified using experiments that provide direct force measurement.

Many-body electrostatic interactions near interfaces and within confined domains have a large significance on numerous dynamic phenomena occurring in the dispersed phase of a colloidal system, for instance aggregation, coagulation, and particle deposition onto collectors. A quantitative description of many-body

electrostatic interactions is also important for many practical processes, such as water and waste water filtration, chromatographic separation, protein and cell separation, and membrane filtration [Adamczyk and Warszynski, 1996; Adamczyk *et al.*, 1997; Ko *et al.*, 2000; Adamczyk, 2003]. Often with these processes, especially filtration and separation, colloidal particles are first adsorbed at the interface, forming a layer, and the presence of such a layer may exert a significant influence on subsequent adsorption of other particles. For similar particles, the deposition rate on a partially covered surface can be substantially reduced due to the electrostatic interaction between the particles. Oberholzer *et al.* (1997) studied the effect of double layer interaction between the charged particles near the jamming limit. In their investigation, interaction energies between the particles was calculated for a 3-body system where two particles are sitting on an interface. However, a more realistic scenario will be attained by considering randomly deposited particles on a surface or a regular array of particles deposited on a patterned surface. The major advantage of considering a patterned surface is that such a surface can be easily produced by using soft-lithography techniques. Since our main objective is to develop an experimental scheme to investigate the exact nature of the electrostatic interaction for many-body cases, we will consider a surface where particles are deposited in a uniform fashion. A detailed description of the geometry and the mathematical modelling is provided in the following section.

5.2 Mathematical Modelling

5.2.1 Geometry and Boundary Conditions

In this subsection, the geometry and the boundary conditions of the problem under consideration are described. The mathematical formulation of this problem in terms of NLPB equation is given in the previous two chapters. Here, a charged planar surface with uniformly deposited colloidal particles as shown in Figure 5.1 is considered. The computational domain used in the finite element

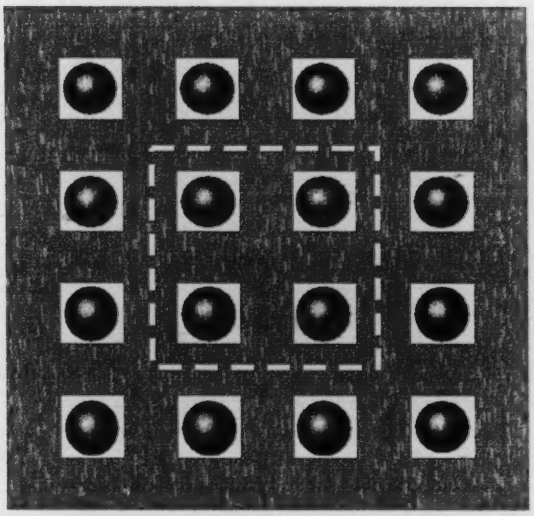

Figure 5.1: Schematic depiction of a patterned planar surface showing an array of square grid with deposited particles.

modelling is depicted by the rectangular region (in white dashed lines) in Figure 5.1. A schematic depiction of the computational geometry corresponding to the many-body colloidal system is shown in Figure 5.2. Here, four spherical colloidal particles of radius a_1 are sitting on a charged planar surface separated (surface to surface) by a distance of twice the particle radius ($L = 2a_1$). The center to center distance between the particles is defined as d. The fifth particle (smaller particle) represents the probe particle of radius a_2 located at the origin of the $x - y$ plane, and is used to measure the force as it approaches the other particles. The vertical separation distance between the center of probe particle and the planar surface along the z direction is denoted as z as shown in Figure 5.2a, while surface to surface separation is h ($= z - a_2$). The coordinates of the center of each particle are depicted in Figure 5.2b. The surfaces of the particles can be assigned constant surface potentials ψ_p or constant charge densities q_p. For simplification, only constant potential boundary condition on the charged bodies is considered in the rest of this study. The surface of the flat plate is assigned a constant surface potential ψ_s, which, for simplicity, is

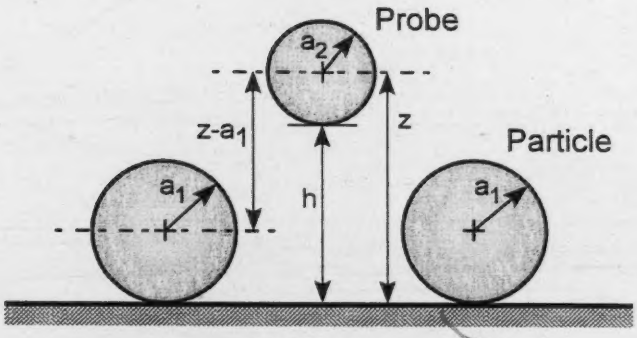

(a) Side view.

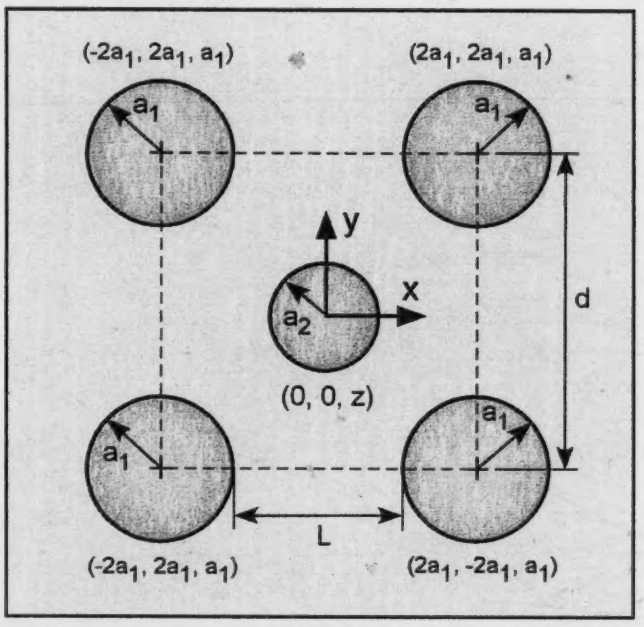

(b) Top view.

Figure 5.2: Geometry showing the details of the finite element computational domain shown in the Figure 5.1. Part (a) depicts side view of the computational domain with geometrical parameters while part (b) shows top view along with the coordinates of the center of each particle.

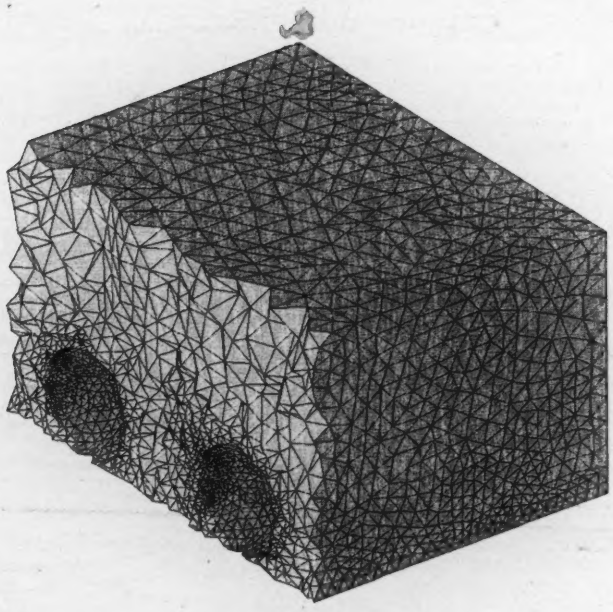

Figure 5.3: Finite element mesh showing tetrahedron meshes for the geometry under consideration.

assumed equal to the surface potential of the particles, ψ_p. On the remaining parts of the boundary, we apply the appropriate symmetry boundary conditions. In a 3-dimensional (3-D) finite element scheme, the computational domain is partitioned into tetrahedron mesh elements whose faces are partitioned into triangular boundary elements as shown in Figure 5.3. All of these length scales are scaled with inverse of Debye screening length (κ) while electric potential is scaled with respect to thermal energy. Detailed description of the normalization procedure of the governing PB equation and boundary conditions is described in Chapter 3.

5.2.2 Force Formulation

The 3-D non-linear Poisson-Boltzmann equation was solved in a Cartesian coordinate system using the finite element technique to obtain the potential distribution in the electrolyte domain. From the numerically obtained potential

distribution, the electrostatic force experienced by the spherical particles can be calculated by integrating the total stress tensor over the particle surface as described in Chapter 3.

The net force acting on a particle along the vertical direction, *i.e.*, in z direction can be written explicitly as

$$\begin{aligned} F_z &= \mathbf{F} \cdot \mathbf{k} \\ &= \kappa^2 \varepsilon \varepsilon_0 \left(\frac{kT}{\nu e}\right)^2 \iint_P \left[n_x E_x E_z + n_y E_y E_z + n_z \left\{ \Pi + \frac{-E_x^2 - E_y^2 + E_z^2}{2} \right\} \right] \mathrm{d}S \end{aligned} \tag{5.1}$$

where E_x, E_y and E_z are the components of the electric field vector $\mathbf{E}$ and n_x, n_y and n_z are the components of the unit normal vector ($\mathbf{n}$) along the x, y, and z directions, respectively. The term Π ($= \cosh \Psi - 1$) in Eq. (5.1) represents the osmotic pressure component, while the other terms represent the electrostatic (Maxwell) stress component.

5.3 Results and Discussions

5.3.1 Particle-Plate Interaction

In this section, a comparison of a 3-dimensional (3-D) finite element result of the electrostatic force experienced by a charged particle near a charged planar surface is presented with corresponding results available in the literature. This represents a limiting case of the 3-D model of the many-body system and provides a validation of the numerical results. In this simple model, a charged colloidal particle (the probe) approaches a bare charged surface (with no deposited particle). This type of geometry can be easily rendered as a 2-D problem, which can be solved using finite element analysis with a fairly high level of accuracy. The simulation results presented here are obtained for constant potential (CP) conditions on the surfaces of both the particle and the plate. Figure 5.4 depicts a comparison of the interaction forces obtained in the present study with the

corresponding analytical expression given by Hogg *et al.* [Hogg *et al.*, 1966]. This expression is commonly known as the HHF (Hogg-Healy-Fuerstenau) expression, which is based on the linearized model of Poisson-Boltzmaan equation. The expression of force between a particle and a plate based on the HHF expression, when both the particle and the plate are held at the same surface potential, can be written as

$$f = \frac{4\pi\Psi^2 \exp(-\kappa h)}{[1 + \exp(-\kappa h)]} \tag{5.2}$$

where f $(= \frac{F}{\varepsilon\varepsilon_0}(\frac{\nu e}{kT})^2)$ represents the scaled force, Ψ is the scaled surface potential, and κh is the scaled surface-to-surface separation distance between the particle and the planar surface. The above expression is based on the linearized PB model, so the calculation based on this expression will always overestimate the force at small separation distances. However, this expression can predict the interaction force more accurately at larger separations and low surface potential situations.

The particle-plate interaction problem can be solved as a 2-D problem using similar techniques as described in the Chapter 3. The accuracy of the 2-D finite element scheme is already well-established based on our comparisons with previously calculated results [Carnie *et al.*, 1994*b*; Stankovich and Carnie, 1996]. Here, the 2-D finite element results based on the NLPB equation is first compared with the results from Eq. (5.2) as shown in Figure 5.4. The interaction forces obtained from the present 2-D finite element model agree with the results obtained from the analytical expression over a relatively wide range of scaled separation distances (surface to surface) $0.0 < \kappa h < 4.0$. The disagreement between the two solutions at small separation distances is mainly attributable to the overestimation of the force by the HHF expression, which is based on the solution of the linearized PB equation. However, for a separation larger than 1.0, both results agree well with each other, which is expected. The full 3-D finite element simulation results (symbols) is also compared with the 2-D finite element results (dashed line), as shown in the Figure 5.4. It is evident that the

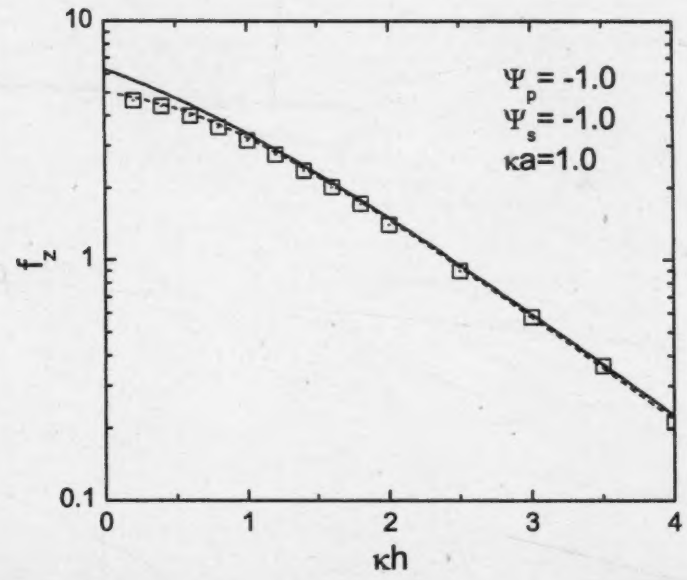

Figure 5.4: Comparison of the electrostatic interaction force between a charged particles and a charged planar surface obtained from finite element simulation with the corresponding estimates from Hogg *et al.* (1966). Solid line represents the result of the analytical HHF expression Eq. (5.2), while dashed line represents the result of 2-dimensional finite element method. Symbols represent the 3-dimensional finite element results obtained under identical geometry and boundary conditions as 2-D finite element model.

3-D simulations provide identical results as the 2-D ones.

Although the above comparison indicates the ability of 3-D finite element approximations to provide a reasonable estimate of the interaction force, it comes at the expense of fairly involved computation. It should be noted that the results in Figure 5.4 for the 3-dimensional case could only be attained by using a large number of elements (usually of the order of 150,000) and carefully choosing the convergence and mesh refinement criteria.

The results of the 3-dimensional finite element simulation are listed in Table 5.1 for two scaled separation distances (κh = 0.4 and 1.0). As shown in the table, for κh = 0.4, the convergence of the force experienced by a charged particle near a charged plate is monotonic and the result is within 2 $\sim$ 3% of

$\kappa h = 0.4$		$\kappa h = 1.0$	
No. of elements	Force	No. of elements	Force
2151	4.1341	2211	3.0835
4301	4.2414	4571	3.0037
12614	4.3169	13913	3.0868
21964	4.3624	23709	3.1721
52841	4.3732	56380	3.1601
175137	4.3825	192425	3.1618

Table 5.1: Steps of the 3-dimensional finite element scheme showing the convergence of the force between the particle and the plate with mesh refinements.

the 2-dimensional finite element results. For the 2-D simulation this level of accuracy was attained with only 30,000 (approx.) elements, but for the 3-D simulation it was attained for the meshes with more than 150,000 elements. A similar trend can be observed for the larger separation distance ($\kappa h = 1.0$). Although the convergence of force for this case shows an oscillatory behaviour even for a large number of mesh elements, the results gradually converge.

5.3.2 Particle over an Array of Deposited Particles

The potential distribution for the case of a probe particle over an array of deposited particles is depicted in Figure 5.5. In this figure, the surface potentials on all the particles are $\Psi_p = -1.0$ and the plate surface potential is $\Psi_s = -1.0$. The scaled dimension (κa_1) of the particles deposited on the surface is 1.0 whereas dimension of the probe particle is 0.5. For a specific value of scaled separation distance between the probe particle and plate surface, the simulation was conducted for different number of mesh elements. The results shown in Figure 5.5 presents the simulation results at scaled separation $\kappa h = 1.5$ between the probe particle and the planar surface for 157,375 tetrahedron mesh elements. The plot represents a pictorial view of the potential decay inside the domain at

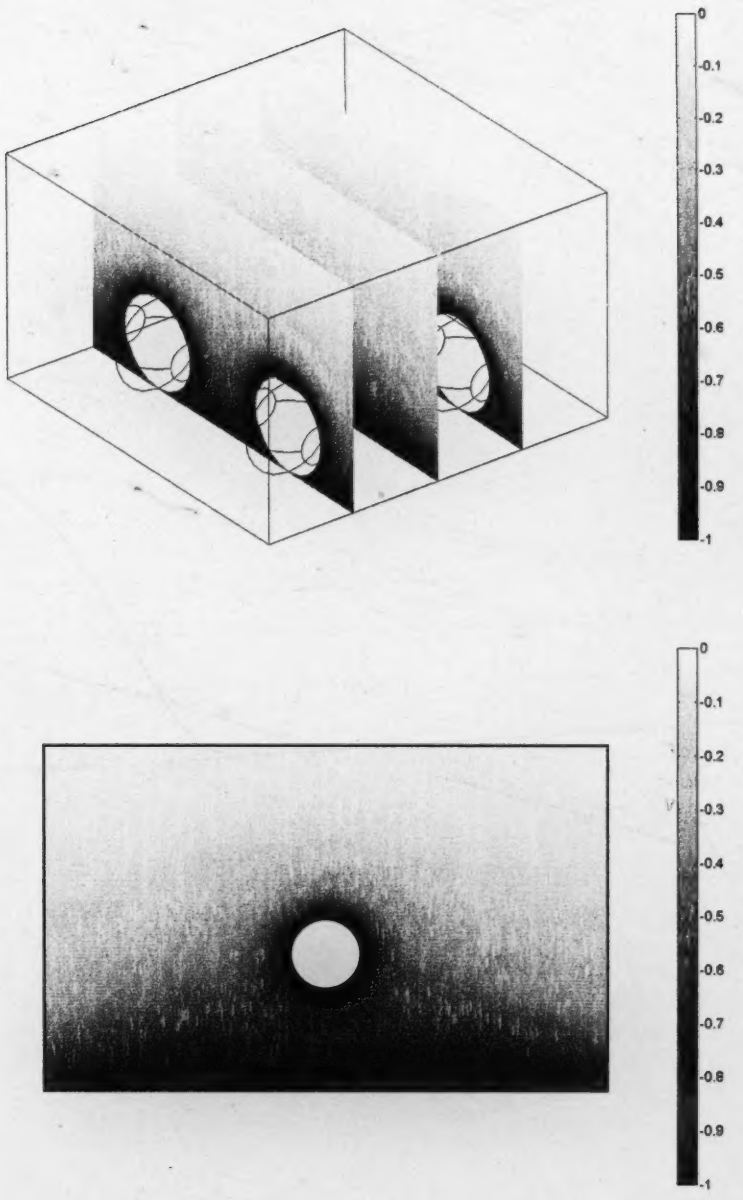

Figure 5.5: Potential distribution of many-body colloidal interaction when a particle approaching toward the previously deposited particles (top). A detail of the middle slice is depicted in bottom part.

three different locations and the profile of the middle slice is shown in the bottom part of the Figure 5.5. The results of force calculations at different levels of mesh refinements are listed in Table 5.2 for two different scaled separations between the probe particle and the plate. The results listed in Table 5.2 show that the force calculations for the two simulations with higher numbers of elements are within approximately 1% of each other, which indicate that this level of mesh refinement could be sufficient for obtaining mesh independent results.

$\kappa h = 0.5$		$\kappa h = 1.0$	
No. of elements	Force	No. of elements	Force
18209	1.3973	19501	1.2463
32669	1.4093	35947	1.2887
78257	1.4487	82947	1.3178
158015	1.4514	149357	1.3294

Table 5.2: Steps of the 3-dimensional finite element scheme of many-body colloidal system showing the convergence of the force experienced by a particle with mesh refinements.

5.3.3 Difficulties of Numerical Solution

The results shown in the previous two sections reveal that a higher level of accuracy can be achieved using a refined mesh. The many-body system shown in the Figures 5.3 and 5.5 requires a large number of elements (approximately 200,000 or higher) to provide a reasonably accurate measure of the force. This level of mesh refinement will need an enormous computational effort. This could not be possible using a traditional Windows based computer system, although current progress of computational systems suggest that this type of problem can be easily solved in the near future using distributed memory or parallel computing.

The critical point in the 3-dimensional finite element modelling was to choose a proper solver, which could be either linear or non-linear. Since the PB equation is a non-linear equation, we started with the built-in non-linear solver available in the FEMLAB software. For the stationary non-linear problem, one can choose between direct and iterative solvers. The solvers in FEMLAB always break down each problem to one or several solutions of linear systems. The choice between direct and iterative solvers for the linear systems affects the solution time and memory requirements. The direct solvers solve the linear system by Gaussian elimination. In 3-D problems, the iterative solvers generally use substantially less memory than direct solvers and they are often faster. On the other hand, the iterative solvers need a careful selection of pre-conditioners for optimal performance. Three different kinds of iterative solvers are available in FEMLAB, namely Good Broyden, generalized minimum residual (GMRES), and quasi-minimal residual (QMR). Among them, the Good Broyden iterative solver works well for most elliptic problems such as the Poisson, Helmholtz, and Navier equations and the GMRES iterative solver is good for the Navier-Stokes equations and other non-elliptic PDE's. However, a different pre-conditioner is also needed to tune the problem properly. The incomplete LU factorization pre-conditioner works well for difficult problems, but it requires a careful choice of drop tolerance. The algebraic multigrid (AMG) pre-conditioner is easier to use, since the default parameters often work well. The AMG works best for scalar elliptic PDE's such as the Laplace and Poisson equations. AMG is the preferred pre-conditioner for electrostatics, conductive media DC, heat transfer, and diffusion 3-D application modes. The symmetric successive over-relaxation (SSOR) and diagonal scaling pre-conditioners also work well for the Laplace and Poisson equations. They normally result in longer computing times than the AMG pre-conditioner, but the solution process will require less memory.

The mesh quality is also important for 3-D finite element simulations, specially for the iterative solvers. For higher mesh quality, the iterative solver will use fewer iterations. Specially with 3-D problems, mesh quality should be

greater than 0.3. For large 3-D problems, it is also difficult to solve the full coupled systems of equations, in particular because of memory constraints. So the system was solved using a coarse mesh by solving for the governing variable, then the mesh was taken to the next level of mesh refinement and solved again for the governing variable using the previous solution as initial guess. For the current model of many-body colloidal system, almost all of the features available in FEMLAB are used. However, a high level of accuracy comparable to the 2-D simulations is still elusive due to the memory limitation of the Windows based computer systems.

5.3.4 Comparison of 3-D FEM Simulations with Pairwise Summation Approaches

The preliminary results obtained in subsections 5.3.1 and 5.3.2 indicate that the interaction force experienced by a probe particle is quite different when it approaches a "clean" planar surface and when it approaches a surface with deposited particles. For instance, comparing the forces experienced by a probe particle at $\kappa h = 1.0$ from Table 5.1 and 5.2, we observe that the scaled interaction force is reduced from *ca.* 3.16 to *ca.* 1.33 from the former to the later. Such a reduction, although quite surprising at a first glance, is not unphysical. However, the extent of this reduction in force is quite remarkable. A simple approach commonly used to estimate the interaction force in such many-body geometries is to algebraically sum the pairwise interactions. In the following, present 3-D FEM results are compared with two types of pairwise summation approaches to assess the extent of force suppression estimated by various approximation techniques vis-à-vis detailed numerical simulations.

In the first pairwise summation approach, an analytical expression is used for the particle-particle and particle-plate interactions based on the solution of the linearized Poisson-Boltzmann (LPB) equation according to Hogg *et al.* (1966). The net interaction force on a probe particle is then obtained by adding the appropriate vertical components of the individual pair-forces. The particle-

plate interaction force expression used was given in Eq. (5.2), while the particle-particle force is given by [Hogg *et al.*, 1966]

$$f = \frac{4\pi\kappa a_1 a_2 \Psi^2 \exp(-\kappa h)}{(a_1 + a_2)[1 + \exp(-\kappa h)]} \tag{5.3}$$

In the second pairwise summation approach, numerical solutions of the non-linear Poisson-Boltzmann (NLPB) equation based on Carnie *et al.* (1994*b*) is used to calculate the individual particle-particle and particle-plate interactions. The net force on the probe particle is then obtained by adding these individual forces. This second approach provides a better estimate of the net force than the first approach, since, for small values of $\kappa a = 1.0$, the non-linear PB equation provides a more accurate solution.

A quantitative comparison between the results obtained from the two above mentioned pairwise summation approaches and the corresponding finite element predictions is depicted in Table 5.3. The finite element simulation results listed in this table are obtained under the identical conditions shown in the Figure 5.5 for four different scaled separation distances. The FEM results were obtained using a fairly high level of mesh refinement (approximately an order of 150,000 elements). As shown in Table 5.2, the force obtained from the final level of mesh refinement is almost independent of the element number, and should be accurate. However, the results of the 3-D FEM simulations in Table 5.3 do not agree with the pairwise summation calculations. The pairwise summation based on LPB gives the highest force, the NLPB based pairwise summation provides a modest (about 15%) reduction in the net force, while the 3-D FEM results are almost 40% lower than the LPB results and about 30% lower than the forces from the NLPB calculations. Based on the results shown earlier in this chapter (section 5.3.1), it seems impossible to attribute this deviation solely to numerical error in the 3-D FEM calculations.

When the probe particle is approaching toward the planar surface, the electrostatic field around the particle is seriously modified due to the previously deposited particles, which causes the subsequent force reduction. These results

	Scaled force (f_z)		
	pairwise summation		
κh	linearized PB	non-linear PB	FE
0.5	2.3709	2.0195	1.4514
1.0	2.2786	2.0534	1.3294
1.5	2.1640	1.8595	1.1642
2.0	1.9590	1.5401	0.9873

Table 5.3: Comparison of force experienced by a particle approaching towards the previously deposited particles on a charged surface calculated using the HHF expression based pairwise summation method (linearized PB), pairwise summation of Hermite Collocation based numerical calculations (non-linear PB), and current 3-D finite element (FE) calculation for different scaled separation distances.

also suggest that the pairwise summation method will seriously overestimate the force for the case of many-body colloidal systems. It should, however, be noted that theses results are applicable for low κa values. For larger κa, the pairwise summation becomes more accurate.

5.4 Concluding Remarks

In this chapter, a 3-D FEM based simulation technique for predicting EDL interactions is presented for a model system that can be easily developed for direct measurement of force in many-body situations. The simulations performed for the 3-D colloidal system reveal that the finite element method would be a good tool for such systems. However, simulations of this type of many-body systems require careful attention to choose element type, solver type, pre-conditioner, and mesh refinement techniques. Computer memory is an important issue to solve a large 3-D system. Although, the comparison between the finite element predictions of particle-planar surface interaction shows a good agreement with the available references, the many-body results deviate from the theoretical pre-

diction as well as from the other numerical results based on pairwise additivity principle. This result suggests that a pairwise summation approach will not be a good approximation to predict the electrostatic interactions in many-body scenarios.

Chapter 6

Conclusions and Future Work

6.1 Concluding Remarks

The main aim of this research was to investigate the electrostatic double layer (EDL) interactions between nanoparticles in confined domains. Based on our literature survey, it was clear that while considerable attention has been devoted toward evaluation of electrostatic double layer interactions, researchers have often neglected the effect of the confining wall, which is important for correctly assessing the electrokinetic transport behaviour of nanoparticles inside narrow capillaries. Hence there is a need to study the electrostatic double layer interaction in micro-capillaries. The calculation of the EDL interaction is quite complicated, especially when particles are trapped inside narrow capillaries. In this case both particle-particle interaction and particle-wall interaction can modify the overall nature of the electrokinetic behaviour of the particles. Thus, in this study, we concentrated on the EDL part of the DLVO interaction to investigate the interaction force inside confined domains.

The major conclusions drawn from the parametric studies carried out with the finite element scheme of the non-linear Poisson-Boltzmann equation developed during the first part of this research are summarized below:

1. The finite element method with adaptive mesh refinement can provide a good numerical tool for the non-linear Poisson-Boltzmann equation to

assess the interaction force between nanoparticles in micro-capillaries.

2. The proximity of the charged capillary wall has a significant influence on the electrostatic interaction force between two spherical particles trapped inside a micro-capillary. The influence of the capillary wall on the particle-particle interaction force was most pronounced when the particle radius was comparable to the capillary radius.

3. The electrostatic repulsion between the particles is considerably suppressed when the capillary and the particle surfaces are like-charged (bearing same sign of the charge or surface potential). Conversely, the interparticle repulsion is more pronounced when the capillary wall is oppositely charged with respect to the particles.

4. Although the effects of the charged wall are not as pronounced for constant charge particles, there are still observable modifications of the short-range interaction force between the particles in presence of the charged wall.

5. Long-rage electrostatic attraction is impossible in the framework of the PB equation. However, it seems pertinent to explore the possibility of modulating the short-range electrostatic interaction force between constant potential particles by altering the surface potential of the confining capillary wall.

6. An order of magnitude modulation in the repulsive force between the particles may be obtained by changing the surface potential of the charged wall by a fraction of a volt. This modulation of force can be exploited to move nanoparticles in microfluidic channels in a controlled manner.

The second part of the research involved the study of roughness effect on the electrostatic interaction between two nanoparticles trapped inside a "rough" capillary. The conclusions from this part of the research are:

1. The electrostatic double layer interaction force experienced by two spherical nanoparticles inside a "rough" capillary can be significantly modified by the roughness of the capillary wall. The influence of the wall roughness is significant when the periodicity of the roughness (wavelength) is comparable to or larger than the particle radius.

2. Influence of roughness is negligible when the periodicity of the roughness is considerably smaller than the particle dimension.

3. The interaction force experienced by the particle is not seriously altered if both the particles and the capillary surfaces are similarly charged (bearing same sign of the surface potential).

4. Influence of the rough capillary wall on the electrostatic force experienced by a particle is more pronounced when the capillary surface potential starts to deviate from the particle surface potential. An oppositely charged rough capillary causes a large fluctuation in the interaction force on the confined nanoparticles.

5. It seems that a roughness analysis is a fairly important criterion for correctly assessing the electrokinetic transport behaviour of nanoparticles inside narrow capillaries, particularly when the particle dimensions are comparable to the hydraulic diameter of the channel.

The last part of the research involved the modelling of many-body colloidal systems in the framework of an experimentally measurable direct force measurement technique. Although this part needs further study, the conclusions based on the current study are:

1. The 3-D finite element model could be a good tool for assessing the many-body colloidal interactions, especially for complicated geometries. However, this type of modelling needs fairly high level of computational power to obtain a desired level of accuracy.

2. The pairwise summation approach commonly used in the literature for assessing many-body interactions would not be a good approximation for EDL forces. This method will seriously overestimate the net force experienced by a particle.

6.2 Future Work

The research described in this thesis can be considered as the first step toward addressing the calculation of many-body colloidal interactions in a rigorous manner. Recommendations for expanding the scope of the research and improvements are numerous, but the initial ideas and tools are in place for future exploration. Based on the results obtained in this study, the finite element scheme of the electrostatic double layer interactions between nanoparticles in confined and many-body geometries can be further improved by considering the following factors:

1. The finite element method described in the first two parts of this study is valid only for the case where the particles are located at the axis of the capillary so that the problem can be rendered as a 2D problem. This study can be extended for the case of complicated geometries in a fully 3-D framework.

2. When solving the Poisson-Boltzmann equation, the ions are treated as point charges. As the system size is reduced, such an assumption will evidently break down. Although this point was not explored, it bears serious consequences on the results for rough capillaries with opposite surface potentials. Generalizing the Poisson equation with more accurate ion distribution formulations is an important subject that warrants further attention.

3. In this study we have simply considered the two static situations corresponding to two different charged states of the colloids and the capillary

wall, without considering the dynamic behaviour of the system as the surface potential on the capillary wall is changed. Secondly, in these simulations, we have not considered the influence of the fluid flow, or the electrolyte polarization due to the charged surfaces of the particles and the capillary. Clearly, these two phenomena will influence the overall behaviour of the colloidal interaction. So this study can be further extended by considering these dynamic effects.

4. Although most of the numerical results were validated against available results for various limiting-case scenarios, a rigorous validation of these results for their intended geometries could not be obtained due to lack of appropriate experimental protocols. Development of experimental methodologies for direct measurement of the forces or for studying the behaviour of nanoparticles in confined channels will be an important contribution toward validating the numerical results. This can be done by using standard micro-fabrication techniques, the preliminary steps for which have been described in this dissertation.

5. Lastly, based on these numerical predictions, it seems possible to develop colloidal actuation based micro-devices for various MEMS applications.

Bibliography

Adamczyk, Z. (2003). Particle adsorption and deposition: role of electrostatic interactions. *Advances in Colloid and Interface Science* **100**, 267–347.

Adamczyk, Z., P. Belouschek and D. Lorenz (1990*a*). Electrostatic interactions of bodies bearing thin double layers. 1. general formulation. *Berichte Der Bunsen-Gesellschaft-Physical Chemistry Chemical Physics* **94**(12), 1483–1492.

Adamczyk, Z., P. Belouschek and D. Lorenz (1990*b*). Electrostatic interactions of bodies bearing thin double layers. 2. exact numerical solutions. *Berichte Der Bunsen-Gesellschaft-Physical Chemistry Chemical Physics* **94**(12), 1492–1499.

Adamczyk, Z., P. Belouschek and D. Lorenz (1991*a*). Electrostatic interactions of bodies bearing thin double layers. *Bulletin of the Polish Academy of Sciences-Chemistry* **39**(4), 423–448.

Adamczyk, Z., P. Belouschek and D. Lorenz (1991*b*). Electrostatic interactions of bodies bearing thin double layers. 3. dissimilar double layers. *Berichte Der Bunsen-Gesellschaft-Physical Chemistry Chemical Physics* **95**(5), 566–573.

Adamczyk, Z. and P. Warszynski (1996). Role of electrostatic interactions in particle adsorption. *Advances in Colloid and Interface Science* **63**, 41–149.

Adamczyk, Z., B. Siwek and P. Weronski (1997). Adsorption of colloid particles at partially covered surfaces. *Journal of Colloid and Interface Science* **195**(1), 261–263.

Bell, G. M., S. Levine and L. N. McCartney (1970). Approximate methods of determining the double layer free energy of interaction between two charged colloidal spheres. *Journal of Colloid and Interface Science* **33**(3), 335–359.

Bhattacharjee, S. and A. Sharma (1995). Lifshitz-van der Waals energy of spherical particles in cylindrical pores. *Journal of Colloid and Interface Science* **171**(2), 288–296.

Bhattacharjee, S. and A. Sharma (1997). Apolar, polar, and electrostatic interactions of spherical particles in cylindrical pores. *Journal of Colloid and Interface Science* **187**(1), 83–95.

Bhattacharjee, S. and M. Elimelech (1997). Surface element integration: A novel technique for evaluation of DLVO interaction between a particle and a flat plate. *Journal of Colloid and Interface Science* **193**(2), 273–285.

Bhattacharjee, S., C. H. Ko and M. Elimelech (1998). DLVO interaction between rough surfaces. *Langmuir* **14**(12), 3365–3375.

Bowen, R. W. and A. O. Sharif (1997*a*). Adaptive finite element solution of the nonlinear Poisson-Boltzmann equation: A charged spherical particle at various distances from a charged cylindrical pore in a charged planar surface. *Journal of Colloid and Interface Science* **187**(2), 363–374.

Bowen, W. R. and A. O. Sharif (1997*b*). Adaptive finite element solution of the nonlinear Poisson-Boltzmann equation: A charged spherical particle at various distances from a charged cylindrical pore in a charged planar surface (vol 187, pg 363, 1997). *Journal of Colloid and Interface Science* **188**(2), 517.

Bowen, W. R. and A. O. Sharif (1998). Long-range electrostatic attraction between like-charge spheres in a charged pore. *Nature* **393**(6686), 663–665.

Bowen, W. R., A. N. Filippov, A. O. Sharif and V. M. Starov (1999). A model of the interaction between a charged particle and a pore in a charged membrane surface. *Advances in Colloid and Interface Science* **81**(1), 35–72.

Bowen, W. R. and A. O. Sharif (1999). Long-range electrostatic attraction between like-charge spheres in a charged pore. *Nature* **402**(6763), 841–841.

Bowen, W. R. and P. M. Williams (2002). Finite difference solution of the 2-dimensional Poisson-Boltzmann equation for spheres in confined geometries. *Colloids and Surfaces A: Physicochemical and Engineering Aspects* **204**(1-3), 103–115.

Carnie, S. L. and D. Y. C. Chan (1993*a*). Interaction free-energy between identical spherical colloidal particles - the linearized Poisson-Boltzmann theory. *Journal of Colloid and Interface Science* **155**(2), 297–312.

Carnie, S. L. and D. Y. C. Chan (1993*b*). Interaction free-energy between plates with charge regulation - a linearized model. *Journal of Colloid and Interface Science* **161**(1), 260–264.

Carnie, S. L., D. Y. C. Chan and J. S. Gunning (1994*a*). Electrical double layer interaction between dissimilar spherical colloidal particles and between a sphere and a plate - the linearized Poisson-Boltzmann theory. *Langmuir* **10**(9), 2993–3009.

Carnie, S. L., D. Y. C. Chan and J. Stankovich (1994*b*). Computation of forces between spherical colloidal particles - nonlinear Poisson-Boltzmann theory. *Journal of Colloid and Interface Science* **165**(1), 116–128.

Chan, B. K. C. and D. Y. C. Chan (1983). Electrical double layer interaction between spherical colloidal particles - an exact solution. *Journal of Colloid and Interface Science* **92**(1), 281–283.

Chan, D. Y. C., R. R. Dagastine and L. R. White (2001). Forces between a rigid probe particle and a liquid interface - I. the repulsive case. *Journal of Colloid and Interface Science* **236**(1), 141–154.

Czarnecki, J. (1986). The effects of surface inhomogeneities on the interactions in colloidal systems and colloid stability. *Advances in Colloid and Interface Science* **24**(4), 283–319.

Czarnecki, J. and T. Dabros (1980). Attenuation of the van der Waals attraction energy in the particle semi-infinite medium system due to the roughness of the particle surface. *Journal of Colloid and Interface Science* **78**(1), 25–30.

Czarnecki, J. and V. Itschenskij (1984). van der Waals attraction energy between unequal rough spherical particles. *Journal of Colloid and Interface Science* **98**(2), 590–591.

Czarnecki, J. and P. Warszynski (1987). The evaluation of tangential forces due to surface inhomogeneties in the particle deposition process. *Colloids and Surfaces* **22**(2-4), 207–214.

Derjaguin, B. V. and L. Landau (1941). Theory of the stability of strongly charged lyophobic sols and the adhesion of strongly charged particles in solutions of electrolytes. *Acta Physicochimica (USSR)* **14**, 633–662.

Elimelech, M. and C. R. Omelia (1990). Effect of particle size on collision efficiency in the deposition of Brownian particles with electrostatic energy barriers. *Langmuir* **6**(6), 1153–1163.

Elimelech, M., J. Gregory, X. Jia and R. Williams (1995). *Particle Deposition and Aggregation: Measurement, Modeling and Simulation*. Colloid and Surface Engineering. Butterworth-Heinemann Ltd, Oxford, England.

Glendinning, A. B. and W. B. Russel (1983). The electrostatic repulsion between charged spheres from exact solutions to the linearized Poisson-Boltzmann equation. *Journal of Colloid and Interface Science* **93**(1), 95–104.

Gray, J. J., B. Chiang and R. T. Bonnecaze (1999). Origin of anomalous multibody interactions. *Nature* **402**(6763), 750–750.

Gregory, J. (1973). Approximate expression for the interaction of diffuse electric double layers at constant charge. *Journal of Chemical Society Faraday Transaction II* **69**, 1723–1728.

Gregory, J. (1975). Interaction of unequal double layers at constant charge. *Journal of Colloid and Interface Science* **51**(1), 44–51.

Harries, D. (1998). Solving the Poisson-Boltzmann equation for two parallel cylinders. *Langmuir* **14**(12), 3149–3152.

Heimenz, P. C. and R. Rajagopalan (1997). *Principles of Colloid and Surface Chemistry*. 3rd ed.. Marcel Dekker Inc., New York.

Herman, M. C. and K. D. Papadopoulos (1990). Effects of asperities on the van der Waals and electric double layer interactions of 2 parallel flat plates. *Journal of Colloid and Interface Science* **136**(2), 385–392.

Herman, M. C. and K. D. Papadopoulos (1991). A method for modeling the interactions of parallel flat plate systems with surface-features. *Journal of Colloid and Interface Science* **142**(2), 331–342.

Hofman, J. A. M. H. and H. N. Stein (1992). Hydrodynamic and surface interaction forces on a particle in a pore. *Journal of Colloid and Interface Science* **154**(2), 359–368.

Hogg, R, T. W. Healy and D. W. Fuerstenau (1966). Mutual coagulaion of colloidal dispersion. *Transaction of Faraday Society* **62**, 1638–1651.

Hoskin, N. E. (1956). The interaction of two identical spherical colloidal particles. I. potential distribution. *Philosophical Transactions of the Royal Society of London. Series A* **248**(951), 433–448.

Hoskin, N. E. and S. Levine (1956). The interaction of two identical spherical colloidal particles. II. the free energy. *Philosophical Transactions of the Royal Society of London. Series A* **248**(951), 449–466.

Hsu, J. P. and B. T. Liu (1997). Electrostatic interaction between two ion-penetrable charged spheroids. *Journal of Colloid and Interface Science* **190**(2), 371379.

Hunter, R. J. (2001). *Foundations of Colloidal Science*. 2nd ed.. Oxford University Press, New York.

Israelachvili, J. N. (1991). *Intermolecular & Surface Forces*. 2nd ed.. Academic Press, San Diego, California.

Ko, C. H., S. Bhattacharjee and M. Elimelech (2000). Coupled influence of colloidal and hydrodynamic interactions on the rsa dynamic blocking function for particle deposition onto packed spherical collectors. *Journal of Colloid and Interface Science* **229**(2), 554–567.

Larsen, A. E. and D. G. Grier (1997). Like-charge attractions in metastable colloidal crystallites. *Nature* **385**(6613), 230–233.

Ledbetter, J. E., T. L. Croxton and D. A. Mcquarrie (1981). The interaction of two charged spheres in the Poisson-Boltzmann equation. *Canadian Journal of Chemistry* **59**(13), 1860–1864.

Lenhoff, A. M. (1994). Contributions of surface features to the electrostatic properties of rough colloidal particles. *Colloids and Surfaces a-Physicochemical and Engineering Aspects* **87**(1), 49–59.

Mark, L. A., J. L. Kaplan and J. C. Williams (2000). An exact solution to the electrostatic interaction between an ion-penetrable sphere and an ion-penetrable rod. *Journal of Colloid and Interface Science* **229**(1), 102106.

Masliyah, J. H. (1994). *Electrokinetic Transport Phenomena.* number 12 In: *AOSTRA Technical Publications Series.* AOSTRA.

McCartney, L. N. and S. Levine (1969). An improvement on Derjaguins expression at small potentials for the double layer interaction energy of two spherical colloidal particles. *Journal of Colloid and Interface Science* **30**, 345.

McCormack, D., S. L. Carnie and D. Y. C. Chan (1995). Calculations of electric double layer force and interaction free-energy between dissimilar surfaces. *Journal of Colloid and Interface Science* **169**(1), 177–196.

Oberholzer, M. R., J. M. Stankovich, S. L. Carnie, D. Y. C. Chan and A. M. Lenhoff (1997). 2-d and 3-d interactions in random sequential adsorption of charged particles. *Journal of Colloid and Interface Science* **194**(1), 138–153.

Ohshima, H. (1996). Electrostatic interaction between two parallel cylinders. *Colloid and Polymer Science* **274**(12), 1176–1182.

Ohshima, H. (1998). Electrostatic interaction between a sphere and a planar surface: Generalization of point-charge/surface image interaction to particle/surface image interaction. *Journal of Colloid and Interface Science* **198**(1), 42–52.

Ohshima, H. (1999). Electrostatic interaction between a cylinder and a planar surface. *Colloid and Polymer Science* **277**(6), 563–569.

Ohshima, H., D. Y. C. Chan, T. W. Healy and L. R. White (1983). Improvement on the Hogg-Healy-Fuerstenau formulas for the interaction of dissimilar double layers. 2. curvature correction to the formula for the interaction of spheres. *Journal of Colloid and Interface Science* **92**(1), 232–242.

Ohshima, H., K. Makino and T. Kondo (1987). Electrostatic interaction of two parallel plates with surface charge layers. *Journal of Colloid and Interface Science* **116**(1), 196–199.

Ohshima, H. and T. Kondo (1993). Electrostatic interaction of an ion-penetrable sphere with a hard plate: Contribution of image interaction. *Journal of Colloid and Interface Science* **157**(2), 504–508.

Ospeck, M. and S. Fraden (1998). Solving the Poisson-Boltzmann equation to obtain interaction energies between confined, like-charged cylinders. *Journal of Chemical Physics* **109**(20), 9166–9171.

Papadopoulos, K. D. and C. C. Kuo (1990). The van der Waals interaction between a colloid and its host pore. *Colloids and Surfaces* **46**(2-4), 115–125.

Pujar, N. S. and A. L. Zydney (1997). Charge regulation and electrostatic interactions for a spherical particle in a cylindrical pore. *Journal of Colloid and Interface Science* **192**(2), 338–349.

Russel, W.B., D.A. Saville and W.R. Schowalter (1991). *Colloidal Dispersions.* Cambridge University Press, Cambridge, New York.

Sader, J. E. and D. Y. C. Chan (1999*a*). Electrical double layer interaction between charged particles near surfaces and in confined geometries. *Journal of Colloid and Interface Science* **218**(2), 423–432.

Sader, J. E. and D. Y. C. Chan (1999*b*). Long-range electrostatic attractions between identically charged particles in confined geometries: An unresolved problem. *Journal of Colloid and Interface Science* **213**(1), 268–269.

Sader, J. E. and D. Y. C. Chan (2000). Long-range electrostatic attractions between identically charged particles in confined geometries and the Poisson-Boltzmann theory. *Langmuir* **16**(2), 324–331.

Shikin, E.V. and A.I. Plis (1995). *Handbook on Splines for the User*. CRC Press, Boca Raton, Florida.

Shulepov, S. Y. and G. Frens (1995). Surface roughness and the particle size effect on the rate of slow, perikinetic coagulation. *Journal of Colloid and Interface Science* **170**(1), 44–49.

Shulepov, S. Y. and G. Frens (1996). Surface roughness and particle size effect on the rate of perikinetic coagulation: experimental. *Journal of Colloid and Interface Science* **182**(2), 388–394.

Smith, F. G. and W. M. Deen (1980). Electrostatic double layer interactions for spherical colloids in cylindrical pores. *Journal of Colloid and Interface Science* **78**(2), 444–465.

Smith, F. G. and W. M. Deen (1983). Electrostatic effects of partitioning of spherical colloids between dilute bulk solution and cylindrical pores. *Journal of Colloid and Interface Science* **91**(2), 573–589.

Sparnaay, M. J. (1983). 4 notes on van der Waals forces - induction effect, non-additivity, attraction between a cone and a flat plate (asperities), history. *Journal of Colloid and Interface Science* **91**(2), 307–319.

Stankovich, J. and S. L. Carnie (1996). Electrical double layer interaction between dissimilar spherical colloidal particles and between a sphere and a plate: nonlinear Poisson-Boltzmann theory. *Langmuir* **12**(6), 1453–1461.

Suresh, L. and J. Y. Walz (1996). Effect of surface roughness on the interaction energy between a colloidal sphere and a flat plate. *Journal of Colloid and Interface Science* **183**(1), 199–213.

Suresh, L. and J. Y. Walz (1997). Direct measurement of the effect of surface roughness on the colloidal forces between a particle and flat plate. *Journal of Colloid and Interface Science* **196**(2), 177–190.

Tamai, H., Y. Nagai and T. Suzawa (1983). Interfacial electrical studies on the deposition of polymer latexes onto fabrics and the removal of these deposited latexes, latex deposition on fibers, deposition state and interaction energy. *Journal of Colloid and Interface Science* **91**(2), 464–471.

Tobiason, J. E. (1989). Chemical effects on the deposition of non-Brownian particles. *Colloids and Surfaces* **39**(1-3), 53–77.

Van Bree, J. L. M. J., J. A. Poulis, B. J. Verhaar and K. Schram (1974). Influence of surface irregularities upon van der Waals forces between macroscopic bodies. *Physica* **78**(1), 187–190.

Verwey, E. J. and J. Th. G. Overbeek (1948). *Theory of Stability of Lyophobic Colloids*. Elsevier. Amsterdam.

Walz, J. Y. (1998). The effect of surface heterogeneities on colloidal forces. *Advances in Colloid and Interface Science* **74**(1-3), 119–168.

Warszynski, P. and Z. Adamczyk (1997). Calculations of double layer electrostatic interactions for the sphere/plane geometry. *Journal of Colloid and Interface Science* **187**(2), 283–295.

White, L. R. (1977). Approximate analytical solution of the Poisson-Boltzmann equation for a spherical colloidal particle. *Journal of Chemical Society Faraday Transaction II* **73**, 577–596.

White, L. R. (1983). On the Deryaguin approximation for the interaction of macrobodies. *Journal of Colloid and Interface Science* **95**(1), 286–288.

Zienkiewicz, O. C. and R.L. Taylor (1989). *The Finite Element Method*. 5th ed.. McGraw-Hill.

Appendix A

Calculation of Force

The force between two charged particles is obtained by integrating the Maxwell stress tensor over a suitable surface.

$$\mathbf{F} = \iint_{p} \mathbf{T}_{ij} \cdot \mathbf{n} \, \mathrm{d}S \tag{A.1}$$

Here $\mathbf{F}$ is the force between the particles, $\mathbf{n}$ is the unit surface normal to the surface over which integration is performed and $\mathbf{T}_{ij}$ is the stress tensor in Cartesian coordinates, which is given by

$$\mathbf{T}_{ij} = \left(\Pi - \frac{1}{2} \varepsilon \varepsilon_0 \, \mathbf{E} \cdot \mathbf{E} \right) \mathbf{I} + \varepsilon \varepsilon_0 \, \mathbf{E}\mathbf{E} \tag{A.2}$$

where $\mathbf{E}$ $(=-\nabla\psi)$ is the electrostatic field vector, Π is the osmotic stress, and $\mathbf{I}$ is the identity tensor. It should be noted that the above expression of force is independent of the choice of the surface over which the integration is performed.

For 2-D case, the stress tensor can be written as

$$\begin{aligned} \mathbf{T}_{ij} &= \Pi \mathbf{I} - \frac{1}{2} \varepsilon \varepsilon_0 \left(E_x^2 + E_y^2 \right) \mathbf{I} + \varepsilon \varepsilon_0 \begin{bmatrix} E_x^2 & E_x E_y \\ E_x E_y & E_y^2 \end{bmatrix} \\ &= \begin{bmatrix} \Pi + \frac{1}{2} \varepsilon \varepsilon_0 \left(E_x^2 - E_y^2 \right) & \varepsilon \varepsilon_0 E_x E_y \\ \varepsilon \varepsilon_0 E_x E_y & \Pi + \frac{1}{2} \varepsilon \varepsilon_0 \left(-E_x^2 + E_y^2 \right) \end{bmatrix} \end{aligned} \tag{A.3}$$

where E_x and E_y represent the potential gradient along the x and y direction, respectively.

For a particle located at the origin, the unit normal can be defined as

$$\mathbf{n} = n_x\hat{i} + n_y\hat{j} \tag{A.4}$$

or

$$\mathbf{n} = \frac{x}{\sqrt{x^2+y^2}}\hat{i} + \frac{y}{\sqrt{x^2+y^2}}\hat{j} \tag{A.5}$$

Using Eqs. A.4 and A.3 in Eq. A.1, the net force on the particle is defined as

$$\mathbf{F} = \iint_p \begin{bmatrix} \Pi + \frac{1}{2}\varepsilon\varepsilon_0\left(E_x^2 - E_y^2\right) & \varepsilon\varepsilon_0 E_x E_y \\ \varepsilon\varepsilon_0 E_x E_y & \Pi + \frac{1}{2}\varepsilon\varepsilon_0\left(-E_x^2 + E_y^2\right) \end{bmatrix} \cdot \begin{bmatrix} n_x \\ n_y \end{bmatrix} \mathrm{d}S$$

$$= \iint_p \begin{bmatrix} \left\{\Pi + \frac{1}{2}\varepsilon\varepsilon_0\left(E_x^2 - E_y^2\right)\right\} n_x + \left\{\varepsilon\varepsilon_0 E_x E_y\right\} n_y \\ \left\{\varepsilon\varepsilon_0 E_x E_y\right\} n_x + \left\{\Pi + \frac{1}{2}\varepsilon\varepsilon_0\left(-E_x^2 + E_y^2\right)\right\} n_y \end{bmatrix} \mathrm{d}S \tag{A.6}$$

Finally, the force acting along the axial direction on the particles is

$$F_x = \mathbf{F}\cdot\mathbf{i}$$

$$= \kappa^2\varepsilon\varepsilon_0\left(\frac{kT}{\nu e}\right)^2 \iint_p \left[n_x\left\{\Pi + \frac{1}{2}\left(E_x^2 - E_y^2\right)\right\} + n_y E_x E_y\right] \mathrm{d}S$$

$$= 2\pi\kappa^2\varepsilon\varepsilon_0\left(\frac{kT}{\nu e}\right)^2 \int_{\mathrm{BCD}} \left[n_x\left\{(\cosh\Psi - 1) + \frac{1}{2}\left(\Psi_x^2 - \Psi_y^2\right)\right\} + n_y\Psi_x\Psi_y\right] r\,\mathrm{d}r \tag{A.7}$$

Eq. A.7 represents the expression for force along the axial direction between two spherical particles inside a cylindrical capillary in a 2-dimensional Cartesian coordinate. Ψ_x and Ψ_y are the components of the electric field vector $\mathbf{E}$ along the x and y directions, respectively. The term (cosh Ψ - 1) in Eq. (A.7) represents the osmotic pressure contribution to the net force and BCD represents the particle surface.

Appendix B

Computer Codes (FEMLAB)

```
% PROGRAM TO CALCULATE THE ELECTROSTATIC FORCE BETWEEN TWO
% SPHERICAL COLLOIDAL PARTICLES INSIDE AN INFINITELY LONG CYLINDRICAL
% USING THE POISSON-BOLTZMANN THEORY.

flclear fem

% Recorded command sequence
% New geometry 1
fem.sdim={'x','y'};

% THIS BLOCK IS FOR GEOMETRY, GENERATED USING FEMLAB GUI
clear s c p p=[-4 -4 -1 -1 0 1 1 1.4 1.4 2.4 3.4 3.4 6.4  ...
6.4;0 1.2 0 1 1 0 1 0 1 1 0 1 0 1.2];
rb={[1 2 3 5 6 8 10 11 1314],[1 1 2 6 11 13;2 3 14 8 13 14], ...
[3 5 8 10;4 7 9 12;5 6 10 11],zeros(4,0)};
wt={zeros(1,0),ones(2,6),[1 1 1 1;0.70710678118654746 ...
0.70710678118654746 0.70710678118654746 0.70710678118654746; ...
1 1 1 1],zeros(4,0)};
lr={[NaN NaN NaN NaN NaN NaN NaN NaN NaN NaN],[0 1 0 1 1 1;1 0 ...
1 0 0 0],[1 1 1 1;0 0 0 0],zeros(2,0)};
CO1=solid2(p,rb,wt,lr);
objs={CO1};
names={'CO1'};
s.objs=objs;
s.name=names;
objs={};
names={};
c.objs=objs;
c.name=names;
objs={};
names={};
```

```
p.objs=objs;
p.name=names;
drawstruct=struct('s',s,'c',c,'p',p);
fem.draw=drawstruct;
fem.geom=geomcsg(fem);

clear appl

% APPLICATION MODE 1
appl{1}.mode=flpdeg2d(1,'dim',{'u','u_t'},'sdim',{'x','y'}, ...
'submode','std','tdiff','on'); appl{1}.dim={'u','u_t'};
appl{1}.form='general'; appl{1}.border='off'; appl{1}.name='NLPB';
appl{1}.var={};
appl{1}.assign={'abscu1x';'abscu1x';'absga1x';...
'absga1x';'absux';'absux'};
appl{1}.elemdefault='Lag2'; appl{1}.shape={'shlag(2,''u'')'};
appl{1}.sshape=2; appl{1}.equ.da={{{'0'}}};
appl{1}.equ.ga={{{'-ux';'-uy'}}};
appl{1}.equ.f={{{'-sinh(u)+uy/y'}}}; appl{1}.equ.weak={{{'0'}}};
appl{1}.equ.dweak={{{'0'}}}; appl{1}.equ.constr={{{'0'}}};
appl{1}.equ.gporder={{4}}; appl{1}.equ.cporder={{2}};
appl{1}.equ.shape={1}; appl{1}.equ.init={{{'0'}}};
appl{1}.equ.usage={1}; appl{1}.equ.ind=1;
appl{1}.bnd.g={{{'0'}},{{'0'}},{{'0'}}};
appl{1}.bnd.r={{{'-u'}},{{'-u+psic'}},{{'-u+psip'}}};
appl{1}.bnd.type={'neu','dir','dir'};
appl{1}.bnd.weak={{{'0'}},{{'0'}},{{'0'}}};
appl{1}.bnd.dweak={{{'0'}},{{'0'}},{{'0'}}};
appl{1}.bnd.constr={{{'0'}},{{'0'}},{{'0'}}};
appl{1}.bnd.gporder={{0},{0},{0}};
appl{1}.bnd.cporder={{0},{0},{0}};
appl{1}.bnd.shape={0,0,0};
appl{1}.bnd.ind=[1 1 2 1 1 1 3 3 3 3];
appl{1}.pnt.weak={{{'0'}}};
appl{1}.pnt.dweak={{{'0'}}};
appl{1}.pnt.constr={{{'0'}}};
appl{1}.pnt.shape={0};
appl{1}.pnt.ind=ones(1,10);

fem.appl=appl;

% INITIALIZE MESH
fem.mesh=meshinit(fem,...
    'Out',    {'mesh'},...
    'jiggle', 'mean',...
```

```
    'Hcurve', 0.3,...        % MESH CURVATURE FACTOR
    'Hgrad',  1.3,...        % MESH GROWTH RATE
    'Hpnt',   {10,[]});

% DIFFERENTIATION RULES
fem.rules={};

% PROBLEM FORM
fem.outform='general';

% DIFFERENTIATION
fem.diff={'ga','g','f','r','expr'};

% DIFFERENTIATION SIMPLIFICATION
fem.simplify='on';

% POINT SETTINGS
clear pnt pnt.weak={{{'0'}}};
pnt.dweak={{{'0'}}};
pnt.constr={{{'0'}}};
pnt.shape={0};
pnt.ind=ones(1,10);
fem.appl{1}.pnt=pnt;

% BOUNDARY CONDITIONS FOR CONSTANT POTENTIAL PARTICLES (CP)
% 'neu' DENOTES NEUMANN BOUNDARY CONDITION AND
% 'dir' DENOTES DIRICHLET BOUNDARY CONITION IN THE 'bnd.type'
% 'psic' DENOTES POTENTIAL ON CYLINDER SURFACE AND
% 'psip' PARTICLE POTENTIAL
clear bnd
bnd.g={{{'0'}},{{'0'}},{{'0'}}};
bnd.r={{{'-u'}},{{'-u+psic'}},{{'-u+psip'}}};
bnd.type={'neu','dir','dir'};
bnd.weak={{{'0'}},{{'0'}},{{'0'}}};
bnd.dweak={{{'0'}},{{'0'}},{{'0'}}};
bnd.constr={{{'0'}},{{'0'}},{{'0'}}};
bnd.gporder={{0},{0},{0}};
bnd.cporder={{0},{0},{0}};
bnd.shape={0,0,0};
bnd.ind=[1 1 2 1 1 1 3 3 3 3];
fem.appl{1}.bnd=bnd;

% BOUNDARY CONDITIONS FOR CONSTANT CHARGE PARTICLES (CC)
% 'sig' DENOTES CHARGE DENSITY
clear bnd
```

```
bnd.g={{{'0'}},{{'0'}},{{'sig'}}};
bnd.r={{{'-u'}},{{'-u+psic'}},{{'-u'}}};
bnd.type={'neu','dir','neu'};
bnd.weak={{{'0'}},{{'0'}},{{'0'}}};
bnd.dweak={{{'0'}},{{'0'}},{{'0'}}};
bnd.constr={{{'0'}},{{'0'}},{{'0'}}};
bnd.gporder={{0},{0},{0}};
bnd.cporder={{0},{0},{0}};
bnd.shape={0,0,0};
bnd.ind=[1 1 2 1 1 1 3 3 3 3];
fem.appl{1}.bnd=bnd;

% PDE COEFFICIENTS ARE DEFINED HARE WHERE ux AND uy REPRESENT
% THE FIRST DERIVATIVES OF GOVERNING VARIABLE WITH x AND y
clear equ equ.da={{{'0'}}};
equ.ga={{{'-ux';'-uy'}}};
equ.f={{{'-sinh(u)+uy/y'}}};
equ.weak={{{'0'}}};
equ.dweak={{{'0'}}};
equ.constr={{{'0'}}};
equ.gporder={{4}};
equ.cporder={{2}};
equ.shape={1};
equ.init={{{'0'}}};
equ.usage={1};
equ.ind=1; fem.appl{1}.equ=equ;

% INTERNAL BORDERS
fem.appl{1}.border='off';

% SHAPE FUNCTIONS
fem.appl{1}.shape={'shlag(2,''u'')'};

% GEOMETRY ELEMENT ORDER
fem.appl{1}.sshape=2;

% BOUNDARY CONDITION ARE DEFINED HERE
fem.const={...
    'psic',   0,...      % CYLINDER POTENTIAL
    'psip',   -3};       % PARTICLE POTENTIAL

% MULTIPHYSICS
fem=multiphysics(fem);

% EXTEND THE MESH
```

```
fem.xmesh=meshextend(fem,'context','local',...
'cplbndeq','on','cplbndsh','on');

% EVALUATE INITIAL CONDITION
init=asseminit(fem,...
    'context','local',...
    'init',   fem.xmesh.eleminit);

% SOLVE PROBLEM WITH ADAPTIVE REFINEMENT
fem=adaption(fem,...
    'iterative','off',...
    'nonlin', 'on',...
    'init',   init,...
    'solver', 'stationary',...
    'context','local',...
    'sd',     'off',...
    'nullfun','flnullorth',...
    'blocksize',5000,...
    'solcomp',{'u'},...
    'linsolver','matlab',...
    'bsteps', 0,...
    'ntol',   1.0e-006,...  % NONLINEAR TOLERANCE
    'hnlin',  'off',...
    'jacobian','equ',...
    'maxiter',25,...        % NO. OF ITERATIONS
    'method', 'eliminate',...
    'uscale', 'auto',...
    'geomnum',1,...
    'maxt',   30000,...     % NUMBER OF MAXIMUM ELEMENTS
    'ngen',   10,...        % NO. OF REFINEMENTS
    'tpfun',  'fltpft',...
    'tppar',  1.7,...
    'eefun',  'fleel2',...  % ERROR CRITERIA
    'eepar',  struct('equ',{struct('f',{1})}),...
    'resorder',0,...
    'rmethod','regular',... % MESH REFINEMENT METHOD
    'report', 'on',...
    'stop',   'on',...
    'out',    'fem',...
    'cplbndeq','on',...
    'cplbndsh','on');

% Save current fem structure for restart purposes
fem0=fem;
```

```
% PLOT SOLUTION
postplot(fem,...
    'geomnum',1,...
    'context','local',...
    'tridata',{'u','cont','internal'},...
    'trifacestyle','interp',...
    'triedgestyle','none',...
    'trimap', 'jet',...
    'trimaxmin','off',...
    'tribar', 'on',...
    'contdata',{'u','cont','internal'},...
    'contlevels',20,...
    'contstyle','color',...
    'contlabel','off',...
    'contmaxmin','off',...
    'contbar','on',...
    'contmap','cool',...
    'geom',   'on',...
    'geomcol','bginv',...
    'refine', 3,...
    'contorder',2,...
    'phase',  0,...
    'title',  'Surface: u (u)  Contour: u (u)  ',...
    'renderer','zbuffer',...
    'solnum', 1,...
    'axisvisible','on')
```